3-30-2017 12:00 AM

Assessment of the Non-linear Stress-strain Characteristics of Poly (vinyl alcohol) Cryogel

Mojdeh Zakeri
The University of Western Ontario

Supervisor
Dr. Timothy A. Newson
The University of Western Ontario

Graduate Program in Biomedical Engineering
A thesis submitted in partial fulfillment of the requirements for the degree in Master of Engineering Science

Abstract

Creation of tissue-mimicking constructs is of great importance in the field of biomedical engineering. Poly (vinyl Alcohol) (PVA) is a biomaterial capable of simulating a wide range of geometries and mechanical properties of biological tissues. It is nontoxic, biocompatible, and easy to produce. PVA can be physically crosslinked by repeated cycles of freezing and thawing. The final product of this process is called PVA cryogel (PVA-C). The mechanical properties of PVA-C can be accurately controlled by changing PVA molecular weight, PVA concentration, and number and duration of freeze/thaw cycles (FTC). In this study, the stress-strain behavior of PVA cryogel was studied for different strain ranges. Unconfined compression and rigid indentation tests were conducted to study the behavior of the material at large strains. Additionally, viscoelastic and poroelastic behavior of the PVA-C were investigated by conducting indentation force relaxation tests on different samples. Furthermore, mechanical behavior of the PVA-C at different strain rates was investigated by conducting unconfined compression tests. A piezoelectric ring actuator was used to estimate the velocity of shear wave propagation in the samples and therefore, to obtain reference shear moduli of the samples at strains of approximately 10^{--5}. Finally, the mechanical behavior of the PVA-C for small strains was investigated by using the resonant column apparatus. Young's modulus, shear wave velocity, and shear modulus at different strains were obtained. Unconfined compression and indentation testing showed shear moduli that ranged between about 0.008 and 0.3 MPa at strains of 3%. It was found that there was some sample size dependency of the shear moduli for certain formulations. The cooperative diffusion coefficient of the PVA-C obtained from force relaxation test was found to decrease from 1.9×10^{-8} m^2/s for 5% PVA, 6FTC to 6.1×10^{-10} m^2/s for 20% PVA, 6FTC. Results of the tests conducted with piezoelectric ring actuator on samples with different PVA concentrations showed that shear wave velocity varies from 45 to 65 m/s in different samples, and has a positive correlation with PVA concentration and number of freeze/thaw cycles. Reference shear moduli of different samples were also found to range between 2.5 and 4 MPa. The results of a damping test on 20% PVA with 6 FTC showed that the damping ratio varies between 6 to 14% over strain magnitudes of 10^{-4} to 10^{-2}. Finally, comparison between the results of the different mechanical tests show that the

shear moduli of PVA-C samples are generally constant for very low strains (less than 0.001). Shear moduli are found to decrease when the strain ranges between 0.001 and 0.05 (medium strain), and finally increase again for strains beyond 0.05 (large strain). Comparison of the mechanical behavior of PVA-C with tests reported in the literature for a range of biological tissues suggest that a number of formulations of PVA-C investigated in this study would be possible tissue mimics for these materials.

Keywords: Poly (vinyl alcohol) cryogel, tissue-mimicking construct, freeze-thaw, laboratory test, stress-strain, shear modulus, shear wave velocity, reference shear modulus, small strain

Dedication

I dedicate this thesis to my parents for supporting me in every path I chose in my life, for trusting me, and for their passion in science.

Acknowledgments

I would like to thank my supervisor, Dr. Newson. He gave me the opportunity to work on this topic and guided me through the research. I was inspired by his passion in science I discovered in our Starbucks meetings.

I extend my special gratitude to my advisor, Dr. Campbell, for all the motivation and support I received from him. Working in National Research Council with him was a wonderful experience impossible to explain in words.

I would also like to thank my lab-mate Jesus Gonzalez for patiently teaching me how to work with resonant column apparatus and helping me solve problems in the lab.

I express a special gratitude to my mother, my father and my sister. Although they were not here, I felt their love and support deep in my heart. They kept me warm and motivated all the way. I cannot thank you enough.

I am especially thankful to my dearest Mojtaba, for his unconditional love and support. He was always there, whenever I needed him, no matter we were thousand miles away or sitting beside each other. The completion of this thesis would have not been possible without his help and encouragement.

Finally, I thank my 8-months old friend Mahoor, for being the cutest and loveliest baby in the world. Watching her videos was sometimes the best stress-relief option.

Table of Contents

List of Figures

List of Tables

List of Abbreviations and Symbols

Abbreviations

ANOVA	Analysis of variance
FTC	Freeze/thaw cycle
LVDT	Linear variable differential transformer
MRI	Magnetic resonance imaging
PHEMA	Poly hydroxyl ethyl methacrylate
PRA	Piezoelectric Ring Actuator
PVA	Poly (vinyl alcohol)
PVAc	Poly (vinyl acetate)
PVA-C	Poly (vinyl alcohol) cryogel
PVA-H	Heated poly (vinyl alcohol) solution
PVA-S	Poly (vinyl alcohol) solution
RCA	Resonant column apparatus
RF	Rectus femoris
PT	Patellar tendon

Symbols

a	Indenter tip radius (mm)
a_a	Angular acceleration (m/s^2)
a_c	Acceleration (m/s^2)

A	Area of the sample (m^2)
A_0	Initial area of the sample (m^2)
A_c	Corrected area (mm^2)
c	Curve fitting parameter
d	Diameter of the sample (m)
D	Indentation depth (mm)
D_c	Cooperative diffusion coefficient (m^2/s)
E	Young's modulus (MPa)
f	Frequency (Hz)
f_n	Natural frequency of the sample at the resonant column test (Hz)
f_r	Resonant frequency (Hz)
F	Load (N)
G	Shear modulus (MPa)
G_0	Reference shear modulus (MPa)
G_d	Shear modulus of the drained network (MPa)
G'	Shear storage modulus (MPa)
G''	Shear loss modulus (MPa)
G^*	Complex shear modulus (MPa)
H	Height of the sample (mm)
H_0	Initial height (mm)

I	Mass polar moment of inertia of the sample ($kg.m^2$)
I_0	Mass polar moment of inertia of the drive system ($kg.m^2$)
K	Offset of accelerometer from the axis of rotation
m	Density (kg)
M_n	Number average molecular weight
M_w	Weight average molecular weight
q	Scattering vector
R	Sample radius (m)
S	Type A durometer hardness
t	Time (s)
t^*	Normalized time (s)
t_r	Poroelastic characteristic relaxation time (s)
t_s	Travel time of shear wave (ms)
V	Volume (m^3)
V_{volt}	Voltage (volts)
V_p	Compression wave velocity (m/s)
V_s	Shear wave velocity (m/s)
V_t	Output voltage as reading from the GDS RCA software (volts)
Y_{meas}	Maximum displacement of the accelerometer
α	Curve fitting parameter

β	Curve fitting parameter
γ	Shear strain
γ_p	Peak strain
γ_r	Reference shear strain,
δ	Phase lag between stress and strain (degree)
ϵ	Strain
ε_a	Axial strain
ϵ_0	Initial strain
ζ	Constant value corresponding with I/I_0
ν	Poisson's ratio
γ	Shear strain
θ	Angle of twist (degrees)
ν	Poisson's ratio (0.5)
ν_d	Poisson's ratio of the drained network
Π	Dimensionless function
ρ	Mass density (kg/m^3)
σ	Stress (MPa)
ω	Angular velocity
ω_f	Frequency of the strain oscillation (Hz)

Chapter 1 : Introduction

1.1 Background

In the latter part of the 20th century, the development of technological innovations potentially affected medicine more than any other scientific discipline. This continuing trend has permitted professionals from other fields to enter the realm of medicine. Biomedical engineering is the integration of medicine and engineering, which advances diagnosis and treatment of diseases by providing medical devices and novel techniques. Biosensors, biomaterials, image processing techniques, and artificial intelligence are some of the tools and methods introduced by biomedical engineers (1). Each of these tools can be used separately or in combination with other medical devices and techniques to improve health care services.

Teaching of surgical skills to medical students and surgery residents is an area where biomedical engineering can make substantial contributions. Traditional teaching methods such as those involving cadaveric and animal models often do not address the needs of current educational settings because of the difficulty and high cost of obtaining specimens, their limited life, and ethical issues (2), (3). Furthermore, the mechanical properties of biological tissues are subject to change ex-vivo and post-mortem. Animal cadaveric specimens can also have different anatomical and tissue characteristics, and they might be or can become contaminated (4). Biomedical engineering gives trainees the opportunity to work in a safer and more appropriate environment by using physical models and virtual reality (2), (5), (6). Virtual reality can provide a realistic simulation of the environment. However, it is often not capable of simulating exact tissue properties and temporal/spatial variations of these properties (5), (6), (7). Physical models used for training surgeons involve tissue mimicking constructs that have been made to precisely resemble the size, geometry, and texture of the real tissue. Research has shown that the degree to which these models imitate real tissue is an important factor in the improvement of surgical skills in trainees (8). Therefore, the materials and the processing methods for production of these models should be chosen such that the final model simulates natural tissues in the best

possible way. Materials used to produce these physical models, as well as other medical devices, are called *biomaterials*. Biomaterials cover a wide range of properties and, therefore, can be used in various biomedical applications (9). In addition to surgical models, tissue mimicking phantoms are widely used in medical imaging research to test the viability of different modalities of medical imaging, such as magnetic resonance imaging (MRI), medical ultrasonography, and elastography (10), (11). When a new imaging technique is developed or an old technique is improved, it is necessary to test the practicality of the method before clinical testing (11). Phantoms should mimic the geometry and anatomical features of the tissue and possess its mechanical, optical, and acoustic properties. They also should be reproducible and able to maintain their structure and shape for long periods of time (7), (10), (12), (13). Mixtures of agar and gelatin (14), water-based gels (Hydrogels) (15), (16), and urethane polymers (16) are some of the biomaterials that have been used to produce phantoms in the medical imaging field. As well as their use in medical imaging, tissue-mimicking constructs can also be used to help fundamental understanding of the mechanical behavior of soft tissues, such as nonlinearity and viscoelasticity (17), (18), since in-vivo testing of these characteristics are potentially difficult, high-risk, expensive, and need to meet ethical obligations.

Biomaterials are also widely used in reparative and regenerative medicine either as tissue engineered-matrices for cell growth (19), (20) or in the form of artificial tissues which substitute damaged tissue (9), (19), (20), (21). Selection of appropriate biomaterials depends on the functions of the tissue that it is going to replace. Metal alloys and ceramics are usually used to mimic hard tissues, such as bones and teeth (9), (22). Soft biological tissues are commonly simulated using polymers and polymeric hydrogels. Poly(methyl methacrylate), polyethylene, poly(vinyl chloride), and poly(dimethyl siloxane) are examples of polymers used in medical applications due to their suitable mechanical and optical properties (9). Hydrogels are cross-linked polymeric networks with a high capability to absorb water (9), (23). They are widely used in biomedical applications based on their specific properties. PHEMA is one of the most common hydrogels widely used due to the similarity of its water content to biological tissues, biocompatibility, and its ability to take a wide variety of forms and properties by changing its preparation methods

(24). Poly(acrylamide) (25), poly(methacrylic acid) (PMAA), poly(methyl methacrylate) (PMMA), poly(maleic anhydride), and poly(vinyl alcohol) (PVA) are some of the other polymers whose hydrogels are useful in biomedical applications (9).

Poly (vinyl alcohol) (PVA) is an industrial non-toxic polymer, which can be cross-linked to form a hydrogel possessing tissue-like features (26), (27). Adding chemical cross-linking agents, irradiation techniques, and physical cross-linking are three mechanisms for gelation of PVA (23), (26), (28). Physical crosslinking is the most appropriate method because it does not leave behind toxic residual agents. Also, hydrogels crosslinked physically have improved mechanical strength and stiffness in comparison to those crosslinked either chemically or by using irradiation techniques (23), (26), (28). In order to physically crosslink PVA, PVA solution has to go through cycles of freezing and thawing. This process is called cryotropic gelation and the final product is PVA cryogel (PVA-C) (26), (27), (28). In addition to high mechanical strength and non-toxicity, PVA-C is biocompatible and non-carcinogenic, has a high swelling degree in water and biological fluids, exhibits elastic behavior, can be produced easily, and is capable of forming complex geometries (27). Moreover, mechanical properties of PVA-C can be easily controlled by changing the molecular properties of the PVA, the PVA concentration in the hydrogel, number and duration of freeze/ thaw cycles, and the rate of the thawing (26), (27), (28). This wide control of a range of properties makes PVA-C a material of great interest for use as a tissue-mimicking model for surgical training (7), medical imaging (10), (11), (13), and research on soft tissue material properties (17), (18). It is also a desirable material for production of artificial tissues such as cartilage (27), (29), meniscus (30), (31), heart valves (32), and pancreas (33), (34).

Soft biological tissues can have a broad range of stiffness and their Young's moduli span at least five orders of magnitude (0.0017 MPa for brain tissue to 40 MPa for kidney). PVA-C has the potential as a material for mimicking geometry and mechanical properties of these soft tissues, by altering PVA concentrations and freeze/thaw cycle features. However, the degree of sensitivity of the material properties to processing methods has not been thoroughly investigated. Biological tissues are viscoelastic materials and exhibit time-dependent properties. Studying the response of PVA-C to different rates of strain allows us

to explore the viscoelastic and rate sensitivity properties of this material. In addition, there is a need to study the behavior of these materials over large ranges of strain; from extremely small strains appropriate to dynamic events and elastic waves, to large strains appropriate to compression and indentation experiments. It is known that soft tissues can experience large range of strain during biological processes and medical interventions. Over physiological ranges, the maximum elongation before tissue ruptures varies between 2%-5% for the tendons to 100%-200% for the mesenteries (35) (tissues forming some of the abdominal organs such as small intestine (36)). Artificial material and tissue experimental testing predominantly investigate the stress-strain responses over very narrow strain ranges. Investigating PVA-C nonlinear elasticity over these broad strain ranges should therefore provide valuable data and improve the quality of tissue-mimicking constructs. This information determined from accurate laboratory measurements is generally absent from the literature.

1.2 Objective

The study contained in this thesis has the following objectives:

- To understand the effect of PVA concentration and number/duration of freeze/thaw cycles on the stiffness properties of PVA-C.
- To investigate PVA-C stress-strain behavior under uniaxial, indentation and torsional loading states to determine the elastic properties.
- To investigate the viscoelastic properties of PVA-C and the response of the material to different rates of strain.
- To study the elastic responses of PVA-C for small, moderate, and large strains (0.00001 to 1).
- To investigate the effect of shear wave frequency and applied pressure on the reference shear modulus (shear modulus at near zero strain), G_0, of PVA-C.
- To investigate the range of tissues that can be mimicked by PVA-C.

1.3 Methods

To achieve the aforementioned objectives, the following approaches were used:

- A review of the literature on the stress-strain behavior and Young's modulus of different soft tissues was performed.
- Cylindrical PVA-C samples of three sizes with different percentages of PVA and various numbers of freeze/thaw cycles were formed. The *isotherm* method with a longer freeze/thaw cycle than conventional cycles was applied for the production of large samples.
- Unconfined compression tests with different rates of deformation were conducted on samples of different sizes and aspect ratio.
- Indentation tests were performed on samples using flat cylindrical indenters.
- Elastic shear waves were transmitted through samples using a novel piezoelectric ring actuator, to find the reference shear modulus using the density of the sample and velocity of the shear wave propagation in the sample.
- Torsional dynamic loading was applied to samples with a resonant column apparatus to investigate the small-strain behavior for different confining pressures of the sample.

1.4 Statement of Originality

I hereby certify that, to the best of my knowledge, studies and tests used in this thesis were not performed by any other researcher and the results has not been published or submitted for publication. I declare that this thesis has not been previously submitted for a degree or diploma at any other higher education institution.

1.5 Thesis Outline

This thesis consists of the following chapters and content.

Chapter one provides a brief overview of the background of the problem and explains the necessity of creating tissue-mimicking constructs and commonly used biomaterials for this

purpose. PVA and its characteristics are briefly explained. It also describes the objectives of this research and methods for achieving the research goals. An outline of the thesis is provided in this chapter.

Chapter two reviews biological tissues and their mechanical properties briefly. Theories of nonlinear elasticity, viscoelasticity, and porosity are briefly described and numerical models for fitting the biological material experimental data are provided. Common biomaterials used for simulating tissue properties are detailed. Polymers and their properties as well as polymer gels and cryogels are explained. PVA-C formation mechanisms, their influential factors, and applications are then discussed. Microstructure of the PVA along with methods of investigating these microstructures are described. This chapter also provides a review of previous mechanical experiments conducted on PVA-C samples.

In chapter three, the material and sample production methods are explained in detail. Preparation of the samples for each test and experimental procedures, as well as test protocols are also explained for unconfined compression, rigid indentation, piezoelectric ring actuator, and resonant column tests. The data analysis methods and equations used for analyzing the data obtained from the mechanical tests are provided. Also, statistical analysis used for verification of the data are described at the end of this chapter.

Chapter four presents the results of the experimental tests. Initially, stress-strain behavior of the materials obtained from unconfined compression are provided. The results of the tests at different strain rates, as well as the tests conducted on samples with different thicknesses are compared together. Afterwards, the Young's moduli of different samples obtained by using indentation tests are provided. Load relaxation test results are shown and the values of cooperative diffusion coefficient obtained from a poroelastic model are compared based on the PVA concentration of the samples. Thereafter, the results of the tests conducted with piezoelectric ring actuator are provided. Furthermore, the data obtained from resonant column test are shown and the relationship between these results is explained. A discussion of the results is then provided and the reasons for the mechanical

behavior of the materials are discussed. At the end of the chapter a summary of the tissues which can be simulated by PVA-C is provided.

Chapter five draws conclusions from the presented research and provides suggestions to add to and improve this work for future studies.

Chapter 2 : Literature Review

2.1 Overview

This chapter provides background information on this project and a review of the related literature. The necessity of production of tissue-mimicking constructs, as well as their required properties are discussed. The mechanical properties of soft tissues are also briefly explained. In addition, the formation and structure of polymers and polymer gels are explained and cryotropic gelation is covered in more detail compared to different methods of gelation. Poly (vinyl alcohol) (PVA) production reaction and material properties are described in the context of the polymer structure. Finally, the range of mechanical tests that have been conducted on this material by other researchers to determine these properties are briefly discussed.

2.2 Biological Tissues and Tissue-mimicking Constructs

The creation of materials that simulate the shape and mechanical behavior of soft biological tissues has been a subject of great interest for researchers and engineers over a number of decades (1), (9), (22). Surgical training, research in medical imaging, and regenerative medicine are some of the areas with a significant need for tissue mimicking materials. The reason for this growing demand is that conventional methods cannot address a range of today's scientific requirements. Current methods have limitations such as difficulties in obtaining human cadaveric tissues, differences between animal and human cadaveric tissues in terms of anatomy and mechanical characteristics, and tissue changes post-mortem which lead to variations in the observed behavior. Tissue-mimicking constructs must simulate the size and biomechanical properties of human tissue to be suitable substitutes for real tissues and organs. In addition, their shape and material properties should be consistent over time.

Biological tissues have various mechanical properties and there are strong links between the structure and function of all tissues. Some of the main properties are described below. Soft biological tissues are typically nonlinear elastic materials and they stiffen as they strain

and therefore, prevent large deformations that may damage the integrity of the tissue (37). Figure 2.1 shows a typical nonlinear stress-strain curve for soft biological tissues, obtained from experimental data on cornea (38). Stiffening of the tissue at higher strains is seen in this figure, where the Young's modulus varies from approximately 0.04 to 2.29 MPa.

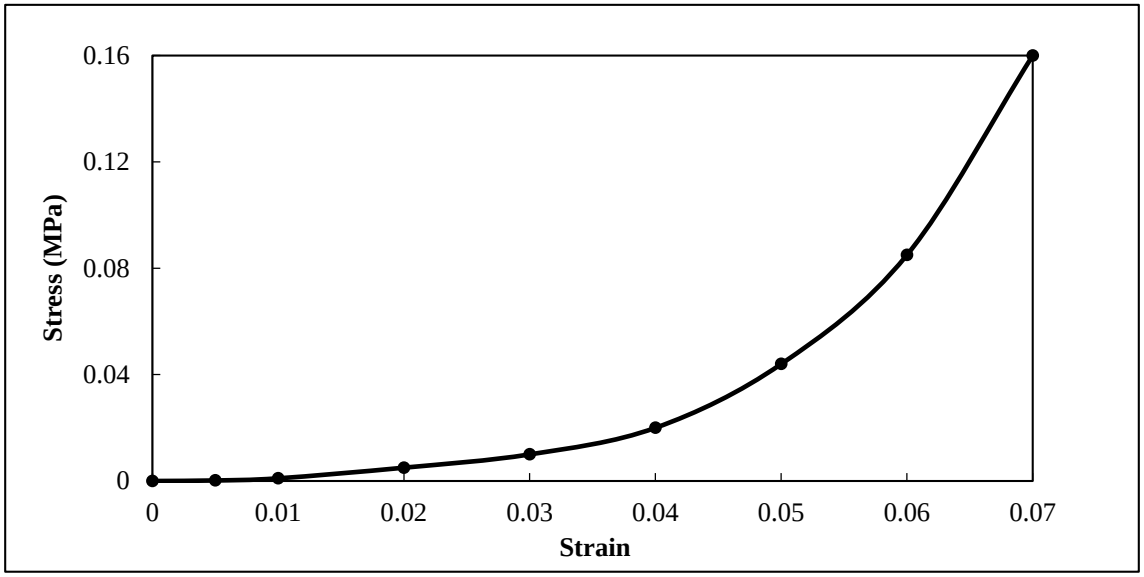

Figure 2.1. Typical nonlinear stress-strain curve for soft biological tissues.

Often biological tissues are also viscoelastic and poroelastic materials. Viscoelastic materials show both viscous and elastic properties when subjected to a deformation (39). Viscoelasticity of biological tissues results from the conformational change of the macromolecules (40). Poroelastic materials consist of an elastic matrix containing interconnected pores that are saturated with fluids (39). Poroelasticity of biological tissues is the result of the migration of the pore fluids under loading (40). Therefore, biological tissues deform gradually when a load is applied to them, as opposed to the instantaneous deformation of primarily elastic materials. Therefore, the mechanical properties of these materials, such as stiffness, depend on the rate at which the load is applied to the tissue and the geometry of the specimens (35), (41). Additionally, biological tissues are non-homogeneous materials and their properties can vary at different points within the same tissue or organ. They can also be anisotropic materials, and the response of the tissue to an applied load depends on the direction of that load (35), (36), (42). For instance, human cornea shows significant mechanical anisotropy. The value of Young's modulus varies in

different sections of the cornea and in-plane sections are stiffer than out of plane sections (43).

Table 2.1. Young's moduli of soft tissues

Body Organ/tissue	Young's modulus (MPa)
Abdominal Organs (44), (36), (45), (46);	
Bladder	0.128
Gallbladder	0.15-4.07
Kidney (Human)	6.7-41.5
Liver	0.46-0.56
Large intestine	0.20- 0.33
Small intestine	0.22- 0.60
Stomach	0.30-0.52
Spleen	0.18- 0.20
Brain (Human) (47), (48), (49);	
white matter	0.0017- 0.0054
Grey Matter	0.0016- 0.0031
Thalamus	0.0025- 0.0032
Midbrain	0.0025- 0.0033
Spinal cord	0.0002- 0.007
Breast (Human) (42), (50)	0.00325- 0.008
Cartilage (Human) (51), (52), (53);	
Articular Cartilage (Fibrous)	0.31- 0.80
Auricular Cartilage (Hyaline)	0.80- 2.78
Eye (38), (54), (55), (56);	
Cornea	0.159- 0.961
Sclera	0.269- 0.412
Intervertebral Disk (57);	
Anulus fibrosus	2.9- 6.6
Nucleus pulposus	0.00169- 0.00481
Muscle (RF) (58)	0.00922- 0.08531
Tendon (PT)	0.0556- 0.3318
Prostate (46), (59)	0.002- 0.0056
Skin (60)	0.001- 0.008
Thyroid (61)	0.009- 0.0114

Table 2.1 shows the values of Young's moduli reported for various soft biological tissues. As shown in the table, Young's moduli of the biological tissues can vary from 0.0017 MPa for the white matter to 40 MPa for kidney.

Biological tissues possess these characteristics due to their components and concentration and structural arrangement of the components. Elastin and collagen are the two main proteins responsible for the mechanical properties of tissues (41), (42). Collagen is a macromolecule which is 280 nm long. These molecules can covalently cross-link and form collagen fibrils, and the intramolecular cross-linking is responsible for the mechanical strength of soft biological tissues. The orientation and diameter of collagen fibrils varies based on the function and strength of the tissue. Collagen fibrils display larger relaxation effects in comparison to other components and is the main reason for the viscoelastic behavior of tissues (62). Elastin is made of long, flexible molecules which can create a three-dimensional rubbery network. Elasticity of elastin changes with deformation and as the elastin chains are straighten, the elasticity of the network increases. Elastin shows very low relaxation behavior and is mainly responsible for the linear elasticity of soft biological tissues (60). The function and integrity of biological tissues are maintained by tension in collagen fibrils and networks (38), (39), (60). As stated in (35), over physiological ranges, the maximum elongation before tissue ruptures varies between 2%-5% for the tendons to 100%-200% for the mesentery. This diversity in properties of different tissues is due to the size, orientation, concentration, and type of this collagen and elastin fibers. This large range of potential mechanical properties presents significant challenges for developing artificial material.

2.3 Theoretical Background

As mentioned in the previous section, soft biological tissues can be viscoelastic and/or poroelastic materials and show nonlinear elasticity behavior. This section provides more detail on these concepts.

2.3.1 Nonlinear Elasticity

Rubber-like materials such as soft biological tissues are able to undergo large strains with small applied stress, depending on their Young's moduli. Theories of linear elasticity such as Hooke's law were initially used to model the mechanical behavior of the rubber-like (elastomer) materials. However, the experimental observations of Mooney (1940) and Rivlin (1948) showed that linear elasticity theories cannot explain the nonlinear mechanical properties of rubber-like materials (63), (64). Hyperelastic constitutive laws are usually used for modelling both nonlinear elastic materials and large strain behavior. Nonlinear elasticity theories, constitute the theoretical basis for hyperelastic material models that can be used to predict tissue behavior (65).

A nonlinear or hyperelastic material is a type of constitutive model for ideally elastic materials and uses a strain-energy function, Ψ, to derive the stress-strain relationship of the material (63). A strain-energy function relates the strain energy density of a material to the deformation gradient (66). For an isotropic material, strain-energy function can uniquely depend on the strain invariants or principal stretches:

$$\Psi_{\text{isotropic}} = \Psi (I_1, I_2, I_3)$$

Where

$$I_1 = \sum_{i=1}^{3} \lambda_i^2$$

$$I_2 = \sum_{ij=1}^{3} \lambda_i^2 \lambda_j^2, \quad i \neq j$$

$$I_3 = \prod_{i=1}^{3} \lambda_i^2$$

and λ_1, λ_2, and λ_3 are the principal stretches.

The Mooney-Rivlin material model was one of the first hyperelastic models developed and has high accuracy when predicting the nonlinear behavior of isotropic rubber-like material (60), (61). The strain-energy function for this model is:

$$\Psi = 1/2 \, [\mu_1 (I_1 - 3) - \mu_2 (I_2 - 3)]$$

where μ_1 and μ_2 are material constants.

Holzapfel (2000) used a statistical theory to establish a model based on the study of vulcanized rubber. This model which is known as the Neo-Hookean model, assumes that the vulcanized rubber is a three-dimensional network of long-chain molecules that are connected at a few discrete points. The strain-energy function for this model is assumed to be:

$$\Psi = c_1 (I_1 - 3)$$

and the shear modulus of the material can be obtained from the relation $G = 2 * c_1$ (67).

Ogden (1984) developed a model based on Ogden's phenomenological theory of elasticity. The model has the general form of:

$$\Psi = \sum_{i=1}^{N} \frac{c_{(2i-1)}}{c_{2i}} (\lambda_1^{c_{2i}} + \lambda_2^{c_{2i}} + \lambda_3^{c_{2i}} - 3).$$

Ogden's model was found to better fit the experimental data for rubber when N=3 (68).

Humphery and Yin (1987) proposed a model to study the passive myocardium. The strain-energy function of this model is:

$$\Psi = c_1(e^{c_2(I_1-3)} - 1)$$

where c_1 and c_2 are the material parameters (69).

Martine's et al. (2006) used these models along with other models to fit their experimental data on silicone-rubber and soft tissues. They found that Ogden's model had the best fit among the other models presented here, and this is a very commonly used model in numerical analysis of biological tissues (65).

2.3.2 Viscoelasticity and Poroelasticity

A viscoelastic material has the characteristics of both fluids and solids. Linear elastic materials deform instantaneously when an external load is applied to them. On the other hand, viscoelastic materials show time-dependent responses and gradually deform and recover when they are subjected to loading and unloading. Stress in viscoelastic material is a function of both strain and strain rate. Spring and dashpot idealizations are used to

mechanically model viscoelastic materials. The spring models the elastic solid and the dashpot models the Newtonian fluid (70), (71).

Viscoelastic behavior of a material is commonly characterized by sinusoidally deforming it. The stress and strain caused by the deformation of an ideal elastic materials are in phase, meaning that there is no phase lag (δ=0) between the invariants. The stress and strain of the ideal viscous materials have a phase lag of 90°, hence there is a lag between its strain and stress response. Stress and strain for viscoelastic material can be obtained from the following equations:

$$\epsilon = \epsilon_0 \sin \omega t,$$
$$\sigma = \sigma_0 \sin(\omega t + \delta).$$

Where

ϵ	strain,
ϵ_0	initial strain,
σ	stress, MPa,
σ_0	initial stress, MPa
t	time, seconds,
ω	angular velocity, radians/sec,
δ	phase lag between stress and strain, radians.

The compressive/tensile storage modulus, E', is a measure of stored energy and describes the elastic behavior of a viscoelastic material. The storage modulus can be defined as:

$$E' = \left(\frac{\sigma_0}{\epsilon_0}\right) \cos \delta$$

The compressive/tensile loss modulus, E", measures the loss of energy in the form of heat and represents the viscous behavior of the viscoelastic material. The loss modulus can be obtained from:

$$E'' = \left(\frac{\sigma_0}{\epsilon_0}\right) \sin \delta$$

The relationship between complex Young's modulus, and compressive/tensile loss and storage moduli can be described using the following equation:

$$E^* = E' + iE''$$

Alternatively the material stiffness can be expressed using shear moduli. The relationship between the complex shear modulus (G^*), shear loss modulus, and shear storage modulus is therefore:

$$G^* = G' + iG'' \tag{2.1}$$

where

G' shear storage modulus, MPa,

G'' shear loss modulus, MPa,

and the *loss tangent* is defined as follows:

$$\tan\delta = \frac{E''}{E'} = \frac{G''}{G'}$$

The loss tangent is a measure of the relative importance of the viscous and elastic components for a given oscillatory frequency (72).

Poroelasticity is a theory for the interaction of the fluid and solid phases of a fluid saturated porous medium (73). This theory was initially proposed by Biot (1941) to calculate the settlement of soils under load during consolidation. The mechanism of soil consolidation is very similar to the process of squeezing water out of an elastic porous medium (74). When an elastic saturated porous medium is subjected to compression, the fluid will flow from the porous medium. As the compressive load is removed, the porous medium reabsorbs the fluid and swells. Therefore, pore fluid pressure can be the reason for the strain in the porous medium. The theory of poroelasticity also implies that a there is fluid movement in a porous medium that is caused by the differences in pore fluid pressure created by different pore volume strains. This fluid movement corresponds to the mechanical loading of the porous medium (75).

Viscoelasticity and poroelasticity usually coexist in some materials such as polymer gels. Separating these properties is still a challenging task in physics and mechanics (76). Anirudh et al. (2014) suggested an indentation stress relaxation method in which these properties can be separated using different time scales in mechanical gels (77). In this method, viscoelastic characteristic time and poroelastic diffusivity of a gel define an intrinsic material length scale of it (i.e. material length scale equals to square roots of

viscoelastic characteristic time multiplied by effective diffusivity of the solvent in the gel). Additionally, a sample length scale over which the solvent migrates in the gel is derived from the size of the indenter tip. They suggest that when the sample length is much larger or smaller than the material length scale, the viscoelastic and poroelastic behavior of the gel are dominative at different time scales (77). The results of their tests on polyacrylamide-alginate hydrogel showed that for large samples in which the sample length scale over the material length scale (i.e. the normalized radii of the gel disks) were set to be 100, 200, and 300, the stress relaxation curves are expected to be sample-size dependent and dominated by the viscoelastic properties of the gel. Therefore, viscoelastic behavior can be obtained from the initial part of the curve (39) and poroelasticity can be obtained from the extreme parts (long times) of the curves (78). For the small sample (sample length scale over material length scale set to be 0.00707, 0.0141, and 0.0212), the time scale for poroelastic relaxation is much smaller than the smallest time scale for viscoelastic relaxation. Therefore, for short time periods, the sample behaves as a poroelastic material and the poroelastic behavior of the material can be obtained from these parts of the stress relaxation curves. The viscoelasticity behavior can then be obtained from the longer time periods of the same curve (77).

2.4 Tissue Mimicking Biomaterials

This section briefly overviews biomaterials that are used to mimic soft biological tissues.

Gel-like material have been widely used to produce tissue mimicking elastographic phantoms. Korte et al. (1997), used agar-gelatin to make vessel mimicking phantoms to use in ultrasound elastography. Samples with 1%, 2%, and 3% dry-weight agar, with the dry-weight concentration of 8% for gelatin. The compression modulus of the samples were tested using a dynamic mechanical analyzer. The results of the tests showed that these phantoms can be used as a model for plaque containing vessels (79). Gao et al. (1995) produced heterogeneous phantom using agar and gelatin mixtures to model a tumor inside the tissue. The dry-weight gelatin concentration was different in the background material and caused osmosis. As the results, the diameter of the tumor increased over time (80).

In addition to elastographic phantoms, biomaterials are also widely used to produce implants and prosthesis. Polymeric materials are usually used to simulate mechanical properties and texture of soft biological tissues (9). Poly (dimethyl siloxane) (PDMS) is a versatile polymer and its properties are less temperature sensitive than other polymers due to the lower glass transient temperature (the temperature region where the polymer transitions from a hard, glassy material to a soft, rubbery material (25)). This stability in different temperatures, along with non-toxicity and flexibility make PDMS a good material to be used as different prosthesis such as finger joints, blood vessels, heart valves, breast implants, outer ears, chin, and nose implants (81).

Biomaterials should also mimic the function of the biological tissues. For instance, biomaterials that are used for contact lenses should have the high permeability to the oxygen. The oxygen is necessary for maintaining clarity, structure, and function of the cornea. Poly (methyl methacrylate) (PMMA) has been used as a material to produce contact lenses since 1936 (82). PMMA is a hydrophobic polymer that has a very good light transmittance, toughness, and stability. It is also a good biomaterial for making intraocular lenses (83). Poly-hydroxyethylmethacrylate (PHEMA) is another hydrogel used for soft contact lens. PHEMA is a hydrophilic polymer and therefore, is slightly cross-liked with ethylene glycol dimethyacrylate (EDGM) to avoid dissolving the hydrogel (77), (78).

2.5 Polymers and Polymeric Gels

Polymers are long-chain molecules that are made of small repeating units called *mer*. Monomers are the small, single, and unbound molecules from which a polymer is synthesized. Mer and monomer of a polymer are not necessarily similar in the number of atoms and atomic bonds (82). Two main factors influencing polymer properties are molecular weight of the polymer and method of polymerization (84), (85).

In polymer synthesis, not all of the polymer chains have similar molecular weights and there is always a distribution of molecular weights. Therefore, an average molecular weight is defined for the purpose of comparison. Two common definitions for calculation of this average are number average and weight average. The number average molecular weight

(M_n) is the total weight of a sample, divided by the number of polymer molecules in the sample. The weight average molecular weight (M_w) is based on the fact that a bigger molecule contains more of the total mass of the polymer. The weight average molecular weight is the second moment of molecular weight distribution over the weight of each polymer chain (84), (85). Linear polymers commonly used for biomedical applications have M_n in the range of 25000 to 100000 and M_w from 50000 to 300000 (9).

There are two main categories of polymerization, addition polymerization, and condensation polymerization. In addition polymerization (chain reaction), unsaturated monomers react and no by-product is produced as the result of the reaction. In condensation polymerization, a low-molecular-weight molecule is formed during each step of the process. Water, hydrochloric acid, methanol, and carbon dioxide are some of the possible by-products of condensation polymerization (84), (85), (86).

2.5.1 Polymeric Gels

Polymeric gels are three-dimensional structures of polymer and immobilized solvent in which macromolecules are connected with stable bonds. The chemical nature of these bonds along with the method of gel formation define the morphology of the gel (87), (62). Immobilized solvent maintains the stability of the gel, allows solutes to diffuse into and out of the network and prevents collapse of polymer gel into a compact polymer mass (88). If the immobilized solvent is water, the gel is called a hydrogel (61). Hydrogels are hydrophilic polymer networks that are able to swell in the presence of water. Hydrogels are capable of absorbing up to 3000 times their weight of water to their network (89), (90), (91).

There are two main methods of gel production. In the first method, hydrogel is produced as the result of swelling of a non-crosslinked polymer, such as a film or a powder, or by swelling of a polymer network, called xerogel, produced by chemical synthesis without solvent. The second method, which is commonly used, is formation of gel in a liquid system. The initial system in this method can consist of either a solution of monomers or polymer. In the first case, gelation occurs as a result of addition polymerization. If the initial system consists of a solution of polymer, gel forms as the result of chemical cross-linking,

self-gelation due to changes in temperature of the solvent, or phase transition of solvent into a gel (87).

Based on the method of cross-linking, gels can be divided into three groups: ionotropic gels, covalently cross-linked gels, and physical gels. In ionotropic gels, macromolecules are bound by electrostatic interactions. In covalently cross-linked gels, also known as *permanent* or *chemical* gels, a cross-linking agent is used to induce gelation (61), (62), (92). Covalent cross-linked gels provide easy control of the crosslinking density. However, formation of non-degradable cross-linking by-products and toxicity of cross-linking agents are two drawbacks when these are used in biomedical applications (23), (26), (91). Physical gels, also called reversible gels, are the result of secondary forces, such as hydrogen bonding, hydrophobic forces, and van der Waals forces between macromolecules in a network (65), (66). Changes in physical conditions, such as temperature, pH, and physical stress may affect physical gels (66). Physical and chemical gels are non-homogeneous materials and there are regions within them with low water swelling and high cross-link density. Figure 2.2 shows a schematic of typical networks formed by chemical and physical cross-linking methods (23).

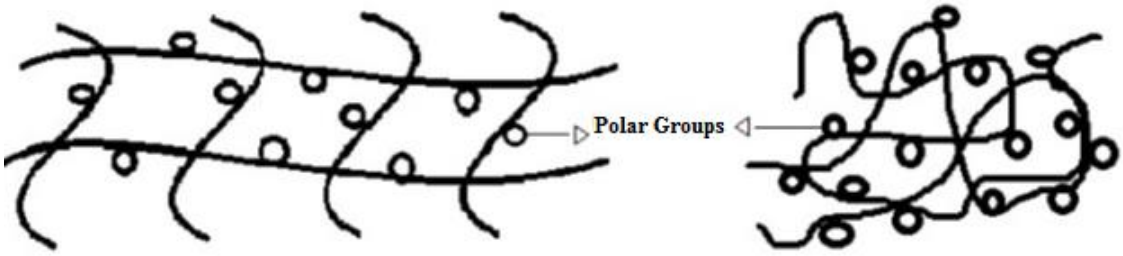

Figure 2.2. Chemically (left) and physically (right) cross-linked gels.

Cryogenic gels are one category of physical gels and are obtained by cryogenic treatment of the system. This kind of gelation is explained in more detail in the following section.

2.5.2 Polymeric Cryogels

Cryogelation is a method of gel formation that is the result of cryogenic treatment of systems to enable the formation of a gel (28), (87). The basis of this method is crystallization of the solvent of the initial gel forming system during the cryogenic

treatment. This feature distinguishes cryogelation from gelation caused by only purely cooling down the system (61). The product of the cryogelation process is called a *cryogel*. Cryogels are often anisotropic, macro-porous, and hetero-phase gels which means that they are consisted of solid, liquid and pores. The temperature cycle in which the solvent crystallizes is known as a freeze/thaw cycle (FTC). Polymer gelation can occur during one of the following steps of the cryogenic treatment:

1. during freezing, which results in a thermo-reversible physical cryogel, such as the aqueous solution of locust bean gum (25);
2. during storage in the frozen phase, which results in chemically cross-linked cryogels (28);
3. during thawing of the frozen sample, which can occur for aqueous poly (vinyl alcohol) (PVA) solution (93).

The benefit of cryogelation compared to other methods is that cryogels are formed at considerably lower concentrations of polymer as opposed to gels that form at room temperature (28). Another benefit is that the solvent can be squeezed out of the gel without destroying the gel structure (99). In addition, cryogels have a higher degree of swelling in comparison with gels made by conventional methods. They are also hetero-phase (containing solid and liquid phases and pores), spongy, non-transparent material, and possess better mechanical properties (99).

PVA cryogel is one of the more popular cryogels because of its mechanical properties, relatively easy production in comparison to other cryogels, and availability (89). Its nontoxicity and biocompatibility also makes it a desirable material for use in biomedical devices (89), (95), (96).

2.6 Poly (vinyl alcohol)

Poly (vinyl alcohol) (PVA) is a synthetic polymer that can be obtained by radical polymerization of vinyl acetate to poly (vinyl acetate) (PVAc), followed by hydrolysis of PVAc to PVA (97). Figure 2.4 shows this material. The properties of the PVA, such as hydrophilicity, solubility, crystallization, mechanical strength, and diffusivity can be

regulated by the molecular weight and the extent of hydrolysis (98). Molecular weight distribution becomes wider as the result of radical polymerization and of PVAc and hydrolysis of PVAc to PVA. Therefore, the degree of hydrolysis is a crucial factor (95), (97), (98). The degree of hydrolysis shows the presence of acetate groups in PVA. PVA with a high degree of hydrolysis of 99% is commercially available and used in this work. It is reported that increasing the degree of hydrolysis of this polymer will decrease the water solubility (99). Therefore, for PVA with degree of hydrolysis higher than 95% the temperature at which the PVA solution is made should be at least 70°C to assure the polymer is solved in water. In addition, as the degree of hydrolysis of PVA increases, it is harder to crystallize (97).

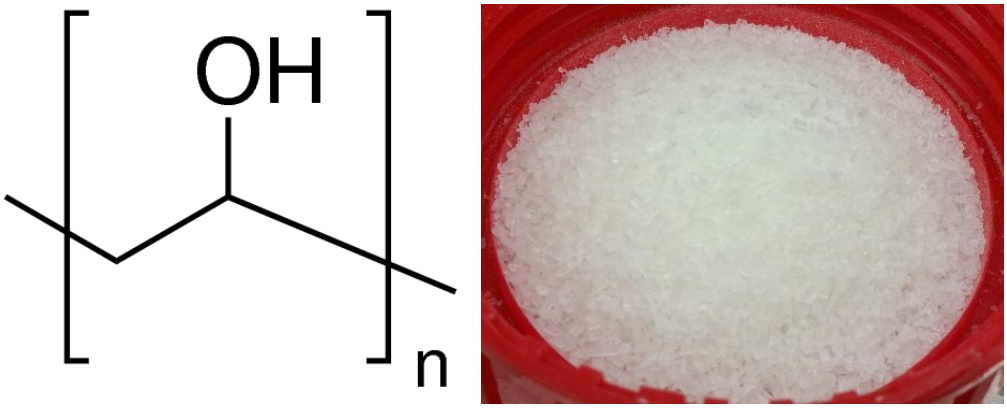

Figure 2.3. Structural formula of PVA (left) and PVA powder (right)

PVA can be cross-linked either chemically or physically. Examples of chemical agents for chemically cross-linking of PVA are glutaraldehyde, epichlorohydrin, acetaldehyde, and other mono-aldehydes (23), (26), (95), (97), (99). However, this method of crosslinking is not widely used due to toxicity and leaching of chemical agents (95). Physical cross-linking of PVA addresses toxicity (23), (100). Cryogenic treatment is the most common method for physical cross-linking of PVA which is obtained by repeated cycles of freezing and thawing (95). By decreasing the temperature during the freezing phase of a freeze/thaw cycle the molecular motion decreases. The intermolecular interaction of PVA, mainly hydrogen bonding, is therefore increased and forms crystallite nuclei. These crystallites act as cross-links and form a three-dimensional network of PVA (polymer-rich area).

Additionally, water freezes during the freezing cycle and forms ice crystals. During the thawing phase, these ice crystals melt and leave behind cavities which will later become filled with liquid water and unsolved PVA (polymer-poor region). Repeating the temperature cycle increases crystallites formation and therefore, physical cross-links, and results in a stronger polymeric network (93), (101), (102). There is no need for cross-linking agents with this method due to the high mechanical strength of PVA-C made with physical cross-linking. PVA-C is stable at room temperature, highly nonlinear elastic, can be formed to mimic different sizes and geometries, has high water content, and can maintain its properties for a long time (26), (95), (97), (101).

The properties of PVA-C are affected by various factors. Molecular weight of the polymer, degree of hydrolysis, PVA concentration in the solution, thawing rate, duration of storage in frozen state, and the number of freeze/thaw cycles (12), (26), (27), (101).

PVA-C formed from polymers with molecular weights less than 70000 are weak gels that cannot maintain their form (102). As the molecular mass of the PVA increases, chain length of the polymer increases and more intermolecular interactions happen. This results in formation of a denser physical network with a higher number of crystallites (28).

Lozinsky et al. (102), showed that PVA solutions with a degree of hydrolysis lower than 90% were not able to form a gel in any condition during freezing. They kept the sample in frozen states for up to ten days, and tried to induce gelation by increasing PVA concentration, but no gel was formed in their study.

As reported in (28), the rate of the thawing in freeze/thaw cycles is the most influential factor for PVA-C properties (28), (102). As observed in a detailed study on the thawing phase of the cryogenic treatment, in a high thawing rate (10 K/min) regardless of the initial concentration of the polymer and the freezing temperature, the solvent does not turn into a gel, but forms a viscous and turbid colloid solution. It was also shown that with slow rates of thawing (0.01-0.05 K/min) very elastic cryogels are formed (28). However, dielectric spectroscopy measurements on PVA-C showed that the dielectric constant, which is a proxy for chain mobility, decreases dramatically when the system is cooled down, and only

partly recovers when it is thawed. This observation suggests that the freezing phase plays the main role in PVA gelation (94).

2.7 Structure of PVA

Study of micro/nanostructure of PVA-C helps to better understand the effect of freeze/thaw cycling on PVA-C properties (103). Transmission electron microscopy (TEM), small angle X-ray scattering (SAX), and small angle and ultra-small angle neutron scattering are some of the methods used to investigate structure of the PVA-C. The following sections will describe some of these methods and the properties of PVA-C obtained from these methods.

2.7.1 Transmission Electron Microscopy (TEM)

Transmission electron microscopy (TEM) is one of the most useful techniques used to study micro-structured fluid systems by providing high resolution direct images. The microscope is capable of directly examining hydrogels which has been thermally treated (cryogel); this technique is called cryo-TEM (104). Willcox et al. (1999) investigated the effect of thermal cycling on the morphology of PVA-C by using cryo-TEM (103). The results of their tests showed that the PVA hydrogel consists of a homogenous polymer-rich phase formed of nano-pores, crosslinked by smaller PVA crystallites, and surrounding micro-pores which are polymer-poor regions. Additionally, it was shown that samples with different freeze/thaw cycles have various morphologies. PVA hydrogel which had gone through no freeze/thaw cycle showed a rounded pore morphology. Rounded pores were also observed in the PVA-C sample with one freeze/thaw cycle (see Figure 2.4). However, the rounded pores were more similar in the sample with no thermal cycles.

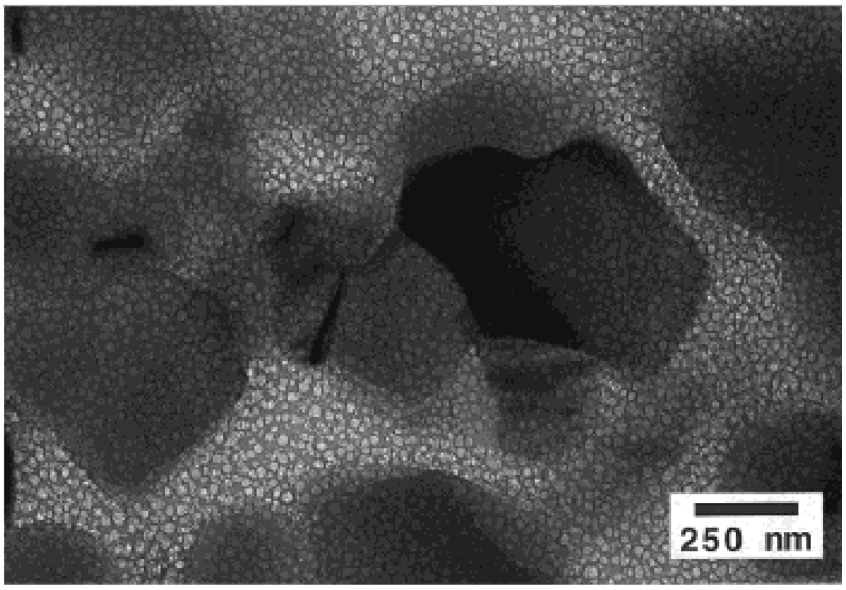

Figure 2.4. Cryo-TEM image of PVA-C after 1 freeze/thaw cycle (103).

Cryo-TEM on PVA-C with twelve freeze/thaw cycles showed that the sample consists of rounded pores, coalesced rounded pores, and fibrillary structures. Finally, PVA-C samples at twenty four freeze/thaw cycles had a three-dimensional fibrillar network (103).

2.7.2 Neutron Scattering

Neutron scattering is the process of investigating material properties by scattering of free neutrons by matter. A thermal neutron is a neutron at room temperature, which has an average kinetic energy of 40 meV and velocity of 2700 m/s at that energy. In addition, neutrons interact with nuclear force of the atoms rather than electrical forces. Therefore, neutrons can travel large distances inside most of the material without being scattered or absorbed. The scattering of the neutrons depends on nuclear species and cross-section of the nuclei (105). Neutron scattering is a good method for studying structure of opaque hydrogels, and hydrogels consisting of organic molecules. To study the structure using neutron scattering, the differential scattering cross-section, which is the total number of neutrons scattered per second into the small solid angle, is measured with a detector and compared to structural models to find a model with has the most similarity to the observed scattering (106).

Small-angle neutron scattering (SANS) and ultra small-angle neutron scattering (USANS) are two different techniques of neutron scattering. The description of these techniques as well as the result of using these techniques to study the structure of PVA-C are provided in the following sections.

2.7.2.1 Small-Angle Neutron Scattering

Small-angle neutron scattering (SANS) provides information on structure at length scales of nanometers to hundreds of nanometers (77). Millon et al. (2007) studied the structural elements responsible for PVA-C anisotropy using SANS (107). Isotropic behavior was also investigated by testing 10% PVA-C samples after various freeze/thaw cycles. To induce anisotropy, PVA-C samples after one freeze/thaw cycle were stretched to 75% of their initial length and then cycled through five more cycles. The results of the SANS showed that before freeze/thaw cycling, the PVA solution consists of a collection of random polymer chains. After one freeze/thaw cycle, the isotropic PVA hydrogel is made of a weak mesh of polymer chains (amorphous phase) crosslinked by PVA crystallites (polymer-rich phase, ofsize 15 to 30 nanometer) with a pore structure (polymer-poor phase, length scale of >100 nm) created by melted ice crystals. Increasing freeze/thaw cycles results in freezing and thawing of the crystals mainly in the polymer-poor pores and therefore, reinforcing the polymer mesh by growing primary and secondary crystallites. Results of the SANS on the anisotropic sample which was subjected to strain after the first thermal cycle, showed that the polymer mesh and polymer-poor phase elongate along the direction of the stretch. However, crystallites maintain their random distribution. Increasing thermal cycles results in freezing and thawing of the ice crystals in the same elongated pores, and reinforcing of the polymer mesh (107).

2.7.2.2 Ultra Small-Angle Neutron Scattering

The ultra small-angle neutron scattering (USANS) device is capable of measuring the differential cross-sections with higher angular resolution and at smaller angles than that of SANS. Therefore, USANS is usually used to extend the length scale to micro-meters and hundreds of micro-meters (in comparison with nanometers in the SANS) (106). Hudson et

al. (2009) characterized anisotropic PVA-C samples with USANS. The results of their tests showed that the length scale of the structures extends to 10 μm (106). They proposed a conceptual model of the polymer structure around the pores as a network of dense polymer knots or blobs. Figure 2.5 shows the model of the structure containing aggregates of size ξ_1, blobs of size R and the fixed polymer length scale (108).

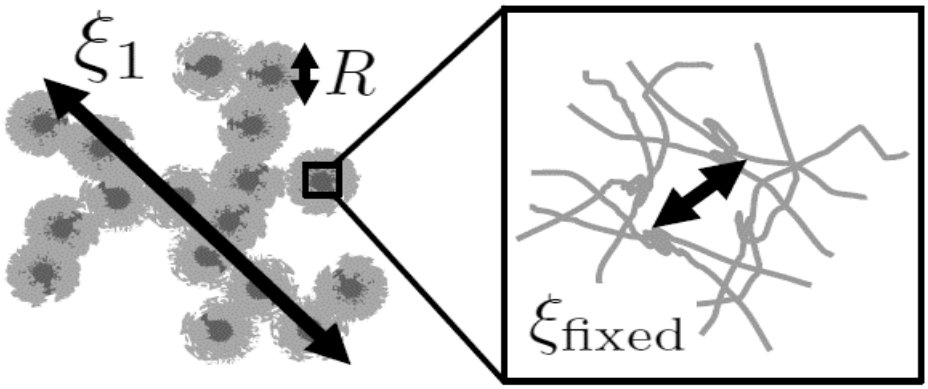

Figure 2.5. Schematic of the structure showing aggregates of size ξ_1, blobs of size R, and the fixed polymer length-scale (ξ_{fixed}) (108).

Their model suggests that for samples subjected to one to three thermal cycles, the blob size increases from about 18 nm to 50 nm. There was no significant increase in the blob size for more thermal cycles. It was also suggested that stronger gel structure at higher thermal cycles is due to the significant amount of loosely bound polymer available on the surface of the blobs. In addition, the maximum size of the aggregates was reported to be above the largest length scale from the USANS data, and the maximum length scale increases from one to three freeze/thaw cycles, but remains unchanged between three to six freeze/thaw cycles (108). Despite the lack of observed changes in structure for higher freeze/thaw cycles, the stiffness of the PVA-C continues to increase.

2.8 Mechanical Tests on PVA-C

Several forms of tests have been conducted by researchers on PVA-C to study different mechanical properties of this material for various states. Compression, indentation, and tensile tests are commonly used for characterizing the stiffness and stress-strain properties

of PVA-C (57), (89), (85). PVA-C is typically described as a biphasic material with both poroelastic and viscoelastic characteristics. It has nonlinear stiffness dependent on strain, strain rate and temperature. It is isotropic and very hydrophilic (109).

One of the traditional experiments for characterizing mechanical properties of biological tissues and biomaterials has been the unconfined compression test (50). Stammen et al. (2001) investigated compressive shear mechanical properties of two samples of a novel PVA-C called *Salubria* that consists of PVA and 0.9% saline (89). The two samples had PVA concentrations of 20% and 25% PVA and were subjected to different numbers of freeze/thaw cycles. Unconfined compression test were conducted on the samples at different magnitudes and rates of strain. The first set of samples were compressed up to 65% strain at a strain rate of 0.017 s^{-1}. The second set of samples were tested at a higher strain rate of 0.17 s^{-1}. The shear modulus of the samples were also tested at 0.013 s^{-1} of shear strain rate, while the magnitude of shear strain was 65%. The results showed that at lower strains (30% magnitude), there was an increase in the compressive modulus of the20% PVA sample as the strain rate increased. However, the rate of strain did not affect the 25% PVA sample at the low strain magnitudes. The increase in the strain rate affected the moduli of both of the samples at higher strain magnitudes. Shear modulus was also found to be strain dependent. Finally, both compressive moduli (1-18 MPa) and shear moduli (0.1 to 0.4 MPa) of the samples were found to be in the range of normal human articular cartilage (89). Wang and Campbell (2009) also used unconfined compression tests to investigate Young's moduli, compressive relaxation of stress, and creep behavior of different PVA-C samples to mimic intervertebral disks (57). The compressive moduli of the PVA-C samples, anulus fibrosus, and nucleus pulposus were measured at 5% and 10% strains and compared together. 3% PVA, 3FTC and 5% PVA, 1FTC formulations were reported to be the optimal material for mimicking the compression behavior of the nucleus pulposus at 5% strain and 10% strains. The results of the stress-relaxation tests showed that the relaxation rate increased with increase in PVA concentration and number of freeze/thaw cycles. Similar results was reported for the creep rates (57).

Tensile test is one other method for investigating mechanical behavior of the PVA-C. Wan et al. (2002), tested the tensile properties of PVA-C to mimic porcine aortic root and to fabricate a stent prototype for a bioprosthetic heart valve with the use of the proper formulation of the PVA-C (90). 15% PVA samples were with different free/thaw cycles profile and different thawing rate to investigate the effect of these factors on tensile and stress- relaxation properties of the PVA-C. The holding time of the samples at -20 °C (freezing point) were 1 or 6 hours and two different thawing rates of 0.1 °C/min and 0.2 °C/min were used. Samples were subjected to 1 to 6 freeze/thaw cycles. During the tensile test, samples were stretched to a maximum strain of 80% and the speed of the test was 40 mm/s. The results showed that the holding time at -20 °C did not affect the properties of the PVA-C. However, slower thawing rates improved the tensile elasticity of the samples. Tensile stress-strain curves showed that the tensile moduli increased with the increase in number of freeze/thaw cycles. Comparison of the nonlinear stress-strain and stress relaxation curves of different PVA-C formulations with the porcine aortic root showed that the 15% PVA, 4FTC formulation closely matches the stress-strain curves of porcine aortic roots. However, the stress-relaxation curve fitting parameters of the PVA-C samples were much lower than that of porcine aortic root (90).

Millon et al. (2006) used tensile testing to investigate nonlinear and anisotropic behavior of PVA-C. 10% PVA samples were made and were subjected to 1 freeze/thaw cycle. After that, the samples were transferred to some designed molds which allowed the samples to be strained to 25, 50, 75, and 100% of their original length in one direction. The stretched samples were then subjected to 5 more freeze/thaw cycles. Uniaxial tensile test was conducted at 40 mm/s strain rate and up to 65% of strain magnitude. The results showed that initial strains that led to anisotropy of the samples, increased the longitudinal stiffness of the samples. It also showed that the difference between perpendicular and longitudinal stiffness was higher in anisotropic samples (110).

Lin and Hu (2006), offered a model for load relaxation of hydrogels indented by a rigid flat indenter. They argued that load relaxation behavior had a relationship with Young's modulus, Poisson's ratio, and cooperative diffusion coefficient (111). Shibayama et al. (1996) studied the dynamics of chemically cross-linked PVA gels with borate ions by

means of light scattering, and evaluated two types of diffusion coefficients. They found that these values are constant for PVA with similar concentrations (112).

Minton et al. (2012) conducted dynamic mechanical tests on two PVA-C samples that have been subjected to two different freeze/thaw cycle profile, to investigate the effect of production method on mechanical properties of the PVA-C samples. 10% PVA-C samples were made and one of the samples was subjected to the conventional freeze/thaw cycle. The second sample was subjected to a freeze/thaw with two additional isotherms near the freezing and thawing points. Dynamic unconfined compression tests at the room temperature was conducted on these PVA-C samples in displacement control with a sinusoidal waveform between 1 and 80 Hz. The compressive complex modulus (E^*), compressive storage modulus (E'), and compressive loss modulus (E") were estimated as a function of frequency. The results of the mechanical tests showed that the PVA-C subjected to the isotherm method of freeze/thaw cycles had a higher elastic moduli (13.4 kPa at 1 Hz, 15.4 kPa at 80 Hz) than that of the sample prepared by the conventional freeze/thaw cycle (6.62 kPa at 1 Hz, 12.4 kPa at 80 Hz). The results also showed that the new method of freeze/thaw cycling has increased the stiffness of the PVA-C (113).

Mechanical properties of PVA-C at small strains is usually measured by using ultrasound imaging. Surry et al. (2004) tested mechanical properties of the 10% PVA-C cylindrical phantoms in different lengths, with different numbers of freeze/thaw cycles. The transmitted sound wave had frequencies in the range of 3 to 8 MHz (depending on the sample), period of 20 μs, and pulse duration of 1 μs. The speed of the sound was found to be between 1520 to 1540 m/s and it was increasing with the increase in number of freeze/thaw cycles (10). Reference Young's moduli of the samples can be calculated using these velocities and mass density of the sample (114). Fromageau et al. (2007) studied the mechanical properties of cylindrical 10% PVA samples subjected to 1 to 10 freeze/thaw cycles by using four different ultrasound elastography method (18). The aim of their study was to characterize mechanical behavior of the PVA-C as elastography phantoms. Shear wave velocity, speed of the sound, and density of different PVA-C samples were studied as a function of number of freeze/thaw cycles. Speed of the sound found to vary from about 1520 m/s for 10% PVA, 1FTC to approximately 1560 m/s for 10% PVA, 6FTC. These

results are similar to what was previously found (18). Shear wave velocity of the samples changed from about 1 m/s to 11 m/s. It was also shown that the speed of the sound, shear wave velocity, and density of the samples increase as a results of the increase in freeze/thaw cycles. The Poisson's ratio in these studies was found to be close to 0.5, implying PVA-C is an incompressible material (18).

2.9 Summary

This chapter provides a review on the mechanical properties of soft biological tissues and explains the need for tissue-mimicking constructs. Values of the Young's moduli for different tissues are provided and typical nonlinear stress-strain curve is shown for a soft tissue. Theories of nonlinear elasticity, viscoelasticity, and poroelasticity are briefly described. Additionally, the relationship between the storage modulus and loss modulus and viscoelasticity are described. The common biomaterials used for mimicking tissue properties and their applications are briefly described in Section 2.4. Chemical concepts of polymers and polymer gels are explained, and different methods and influential factors in producing polymer cryogels detailed. PVA-C properties were described and cryogenic mechanisms gelation of the polymer were discussed. Additionally, the results of the studies on micro/nanostructures of the PVA-C obtained from TEM, SANS, and USANS showed that the PVA-C is a biphasic material which consists of polymer-rich and polymer-poor regions. The final section of the chapter reviews different mechanical tests previously conducted on the PVA-C at different strains and strain rates. Results of tensile, unconfined compression, and indentation tests reveal the mechanical behavior of the material in large strains. Whereby, the results of ultrasound imaging show the behavior of the material in small strains.

Chapter 3 : Study of Materials and Methods

3.1 Overview

To investigate the effect of PVA-C preparation methods on the mechanical properties of the material, PVA-C was manufactured in the laboratory with different polymer concentrations and numbers of freeze/thaw cycles. These samples were then tested using different methods and to investigate their behavior for extremely small, moderate, and large magnitudes of strain.

In this chapter, the procedures for preparation of the PVA-C samples with different polymer concentrations and different numbers of cycles are explained, followed by a description of all of the devices and test procedures used to obtain the desired data. Methods of data analysis and statistical analysis conducted on the data are also explained in this.

3.2 Sample Preparation Method

To prepare the PVA-C samples, PVA solution was heated and then solidified by using low temperature thermal cycles. Methods for hydrogel and cryogel preparation are explained in this section and follow the protocols of Campbell (2014) (115).

To produce a particular polyvinyl alcohol solution (PVA-S) concentration, PVA powder (molecular weight 146000-186000, 99% hydrolyzed, Aldrich Chemical Co., Inc.) was mixed with deionized, distilled water. For instance, 30 g of PVA powder was mixed with 270 ml deionized water to make 300 g of 10% w/w PVA-S. This solution was then added to a 1000 ml, flat bottomed reaction flask with a three-necked top, placed in a heating mantle which power controller was set on 40 Volts. To prevent clumping of the PVA-S on the bottom of the flask during hydrogel preparation, a stainless-steel mixer blade attached to a stirring rod was placed inside the flask through the center neck of the flask top and connected to a mixer. The rotational speed of this mixer depends on the solution mass. A thermometer was then inserted in the other neck of the flask top to continuously read the temperature. The intention was to make sure that it did not exceed 80°C. In addition, a Pyrex condenser was attached to the third neck of the flask to avoid excessive pressure

build-up in the close flask. It also keeps the hydrogel from increasing the PVA concentration by condensing water vapor. The preparation apparatus setup is shown in Figure 3.1. The solution was heated as described for 1 to 2 hours (depending on its mass). As a result of this procedure, clear, jell-like PVA-H with 5%, 10%, 15%, and 20% PVA concentrations was produced. To avoid bacterial growth in the samples, 0.2% w/w of biocide (Germall Plus powder) was added to the PVA-H right after removing the flask from the heating mantle. PVA-H was then poured into the molds to form samples.

Figure 3.1. Setup used for PVA-H preparation.

To ensure homogeneous samples and reproducible data sets, air bubbles should be removed from the PVA-H before starting the thermal cycles. To remove bubbles from the PVA-H with lower PVA concentrations (5% and 10% PVA), hot PVA-H filled molds were allowed to sit for 1 to 2 hours at room temperature. The bubbles are found to disappear while the hydrogel is cooling down. However, removing air bubbles from higher concentration 15% and 20% PVA samples was more challenging. The ideal method for removing air from these samples is to put the molds under vacuum and heat them simultaneously (123).

Unfortunately, this setup was not available for this research. Another method used in this work was therefore to heat the prepared PVA-H at 90°C for 1 to 2 hours. Bubbles were found to be completely removed from 15% PVA-H samples using this method, however there were still a small percentage of bubbles left in the 20% PVA-H samples.

Samples were formed by pouring the PVA-H into LEXAN molds; these were two puck-shaped with different sizes and one cylindrical mold. The mini-puck mold (Figure 3.2) is 38 mm in diameter and 12 mm high, the standard puck mold is 50 mm in diameter and 12 mm high, and the cylindrical mold is 50 mm in diameter and 100 mm high.

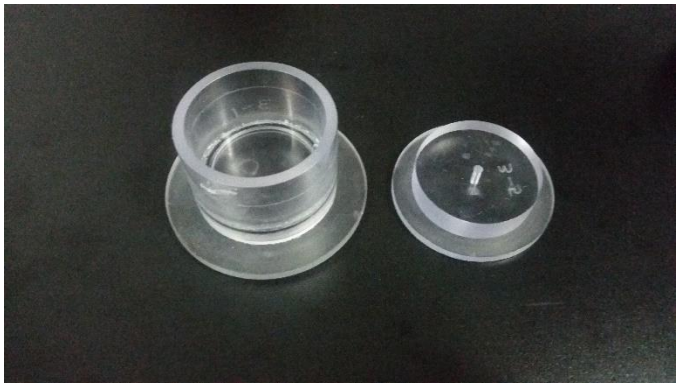

Figure 3.2. Typical LEXAN mold for preparation of mini-puck PVA-C samples.

All of the molds were then put into an environmental chamber (Model 1007S Temperature Chamber, TestEquity Inc., Montreal, Canada) to create the PVA-C samples. During a single freeze/thaw cycle, the samples were cooled from +20°C to -20°C at a constant rate of 0.1 °C/minute (freeze cycle), held at -20°C for one hour, warmed up from -20°C to +20°C at 0.1 °C/minute (thaw cycle), and kept at +20°C for fifteen minutes. This process took approximately fifteen hours and these steps were repeated if additional cycles were needed. Figure 3.3 shows a typical temperature versus time graph for one freeze/thaw cycle (FTC).

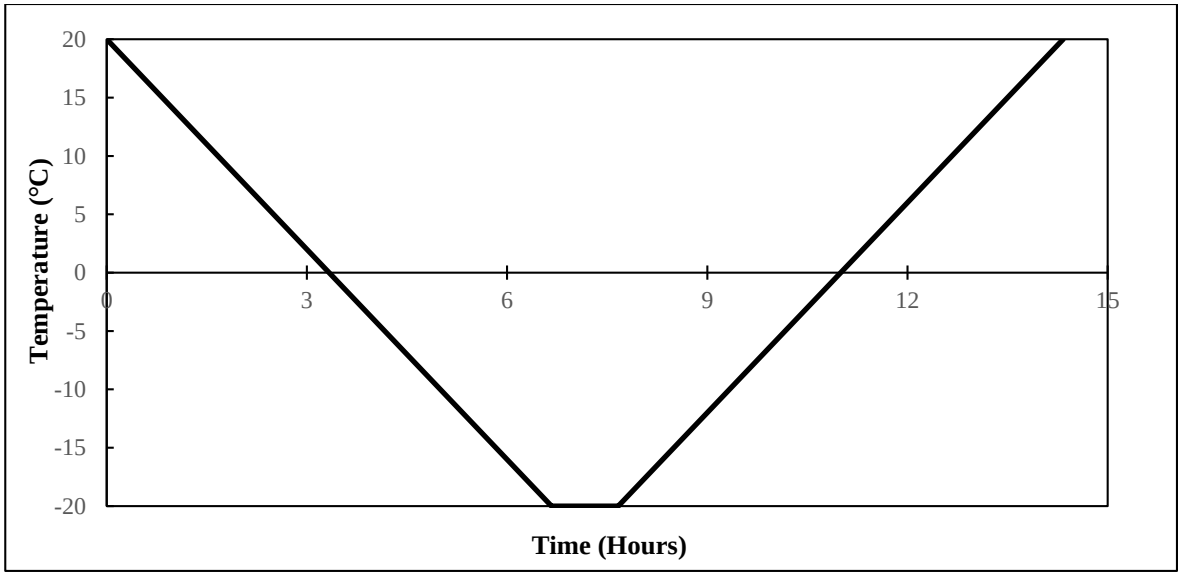

Figure 3.3. Temperature versus time for one freeze/thaw cycle.

The molds were finally taken out of the chamber after 2, 4, or 6 FTCs and stored in airtight containers, submerged in deionized water. While using the samples for mechanical tests, care was taken not to take the sample out of water for long periods. They were returned back to water container right after finishing the tests, to avoid sample dehydration. To investigate effect of dehydration on mass and dimensions of the samples, a series of measurements were conducted on different samples and the results are shown in Appendix A.

3.3 Mechanical Characterization Tests

To investigate the mechanical properties of the PVA-C over different ranges of strain (zero, small, moderate and large) various mechanical tests were conducted on the samples. Descriptions of each test setup and the procedures are described below.

3.3.1 Unconfined Compression Test

One-dimensional unconfined compressive stress-strain of the puck and cylindrical PVA-C samples was conducted using a parallel plate apparatus (Versa-Loader, ELE International, Bedfordshire, U.K.). As shown in Figure 3.4, this apparatus consists of a lower stainless steel plate, which moves upward at a constant rate and compresses the samples (of height

H and radius R) to the desired displacement of ΔH. The upper plate of the apparatus is a rigid acrylic disk, which is connected to a high resolution load cell with the capacity of 500 lbf and accuracy of ±1%. A linear variable displacement transducer (LVDT) (0-10 mm, ±0.25% linearity) continuously records the displacement of the lower plate.

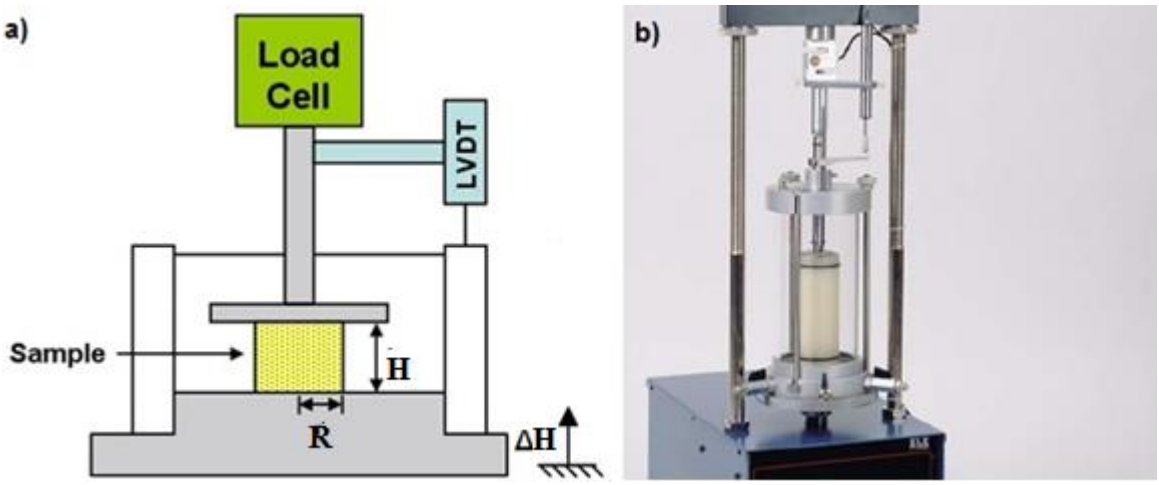

Figure 3.4. a) A schematic of the apparatus used for unconfined compression test. b) Versa Loader apparatus that was used for the test.

A Hoskin Scientific four-channel data readout machine was used to collect data from the load cell and the LVDT. This data was exported for display and analysis using the GETDATA version 4.31a Data Collection Program Software Package.

Flat ended mini-pucks (38mm diameter×12mm height) and large cylindrical samples (50mm diameter×100mm height) with different PVA concentrations and number of freeze/thaw cycles were used for the purpose of this test. Samples were located between the two plates of the Versa-loader. The upper plate was lowered until it was very close to the surface of the sample, but having no contact between them. At this stage, displacement and force in the data readout machine were zeroed and the test was started by moving the lower plate upward. Most of the unconfined compression tests were conducted at a maximum strain rate of 2 mm/min ($0.17s^{-1}$). A limited number of tests were also conducted at a lower strain rate of 0.5 mm/min to investigate the effect of strain rate on the properties of the samples. The upward movement of the lower plate continued until the applied load on the sample reached 1000 g or until the sample was compressed to 30% of its initial

height (whichever occured first), then the sample was unloaded to return it to its initial state. The displacement and corresponding load on the sample were recorded every second by the GETDATA software.

3.3.2 Rigid Indentation Test

Indentation is commonly used to test the mechanical properties of different materials. The importance of this method in characterizing local mechanical properties of bio-polymers and soft tissues has grown significantly (116), (78), (117).

In this study, the indenter employed the same parallel plate apparatus that was used for the unconfined compression test (Versa-Loader, ELE International, Bedfordshire, U.K.). However, the upper plate used in the unconfined compression test was replaced with a cylindrical aluminum punch with a diameter of 8 mm as the indenter tip (Figure 3.5).

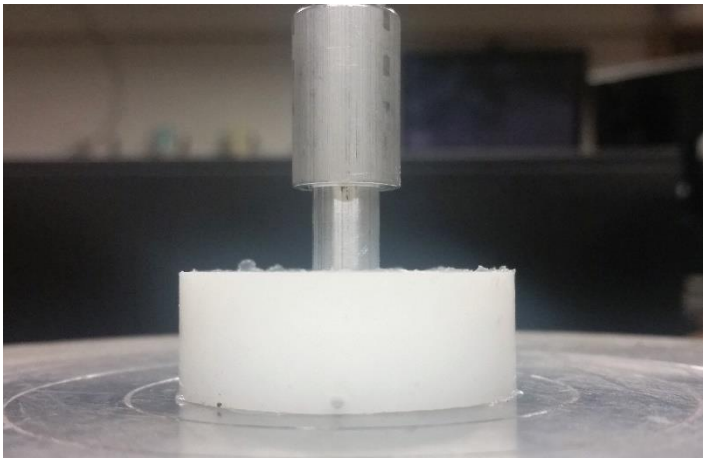

Figure 3.5. Flat ended aluminium indenter tip applying load on a mini-puck sample.

Mini-pucks and large cylindrical samples were used for the purpose of these tests. Samples were placed on the lower plate and the indenter was located at the center of the samples, very close to the face of the sample but not touching it. The data readout was zeroed to accurately measure the amount of initial load and displacement. The lower plate was moved upward at a rate of 2 mm/min (0.17 s^{-1}) (the same rate as the unconfined compression test). The test continued until the sample reached 30% strain or until 1000 g of load was applied to the sample. The sample was then unloaded to reach its initial position. A few tests were also conducted at a strain rate of 0.5 mm/min (0.017 s^{-1}) to investigate if strain rate has an

effect on the mechanical properties. Force (F) and indentation (D) data of the samples were again recorded using GETDATA software.

3.3.2.1 Force Relaxation Test

Force-relaxation indenter tests were also conducted on 5% to 20% PVA mini-pucks. The purpose of this test was to investigate the viscoelastic and poroelastic properties of the samples at a constant displacement.

The samples were loaded until the indenter penetration depth reached 10% (D/H=0.1) of their initial height. The lower plate was then stopped and the indenter remained at that constant displacement for 1000 seconds. Changes in force were recorded every second.

3.3.3 Piezoelectric Ring Actuator

Measuring the velocity of the propagated shear waves in a material is an important method used for characterizing mechanical properties of materials. This method has the ability to measure elastic or shear moduli (reference shear/Young's modulus) at very small strains (less than 0.001% strain), where modulus is not affected by strain magnitude. Elastographic techniques are usually used to send low frequency shear waves to soft biological tissues and measure Young's moduli (118), (18), (119), (120). In addition to ultrasound and elastography, shear waves can also be generated by piezoelectric transducers (114), (121).

In this work, a piezoelectric ring actuator (PRA) was used to send and receive shear waves. This innovative PRA device was fabricated in the geotechnical research laboratory at the University of Western Ontario (122). The piezoelectric ring actuator consists of an upper and a lower piezoelectric plate, which sends and receives shear waves respectively. These plates are connected to an amplifier that is in turn connected to a wave-form generator and then to a computer. The LabView program is used to control and plot the signals.

The PRA was incorporated into a standard oedometer apparatus (91). Figure 3.6 shows the setup for this test. Care was taken to align two piezoelectric plates properly, so that the input and output signals could be recorded satisfactorily. Puck samples with 50 mm diameter and 12 mm height were placed between the upper and lower piezoelectric plates

in the center of the piezoelectric ring. This assembly was then located in the oedometer creating a one-dimensional unconfined compressive loading state. It is necessary to make sure that the fulcrum is leveled, otherwise there is an initial loading on the sample. After leveling the lever, weights were placed on the load hanger. The axial load applied on the sample was ten times larger than the weight on the load hanger. Minimum weight applied was the weight under which a clear signal propagation could occur. Therefore, twelve different weights between 100 g and 2000 g were used to investigate the effect of the axial loading on the wave velocity and reference shear modulus.

Figure 3.6. Piezoelectric ring actuator incorporated in an oedometer. A LVDT is used to track changes in sample's height.

Initial thickness of each sample was measured before any load was applied to the sample. Also, a LVDT (maximum displacement of 10 mm) was used to measure the changes in the thickness of the samples after applying each load. Therefore, the distance traveled by the

wave was accurately measured. Mass of the samples were measured right before starting the test to minimize potential measurement error caused by water mass loss of the samples. The transmitter was then excited with a single-frequency sinusoidal pulse. The input pulse amplitude is a factor depending on the transducer. The amplitude of the input waves transmitted by the PRA was 0.8 mV. To investigate the effect of wave frequency on shear wave velocity and reference shear modulus, waves with four different frequencies were sent to the samples. The optimum frequency of the waves depends on the factors such as sample size, rigidity, and actuator type. According to the literature, wave frequencies should be less than 20 kHz for samples with thicknesses between 10 to 14 cm (114). Based on the initial results for each sample, four frequencies for which the arrival wave was clear, were chosen to be 6, 8, 10, and 12 kHz.

3.3.4 Resonant Column Test

The resonant column test was used to study the dynamic properties of the PVA-C. The resonant column vibrates the cylindrical sample in a fundamental mode of vibration, in an axial or torsional state. Based on the measured resonant frequency and amplitude of vibration, shear wave velocity and shear modulus can be calculated (123), (124).

For the resonant column test, the height to diameter ratio for the optimum results is 2 to 1 (125). Therefore, cylindrical samples with 50 mm diameter and 100 mm height were used for the purpose of this test. The diameter was the same size as the top and bottom cap of the resonant column. Although the resonant column was adjusted for different heights, care was taken to make sure that the height of the top cap was adjusted as accurately as possible so that the specimen was set within the device range. Diameter, height, and mass of the sample was accurately measured before placing the sample in the resonant column apparatus. The sample was then placed on the bottom cap and covered by a latex membrane to avoid any contact with air. Drops of water were added to the membrane to prevent dehydration of the PVA-C sample during the period of the test. Consequently, the top cap was placed in accordance with the system specifications. O-rings were used to keep the membrane on the top and bottom caps and maintain the proper contact between the caps and the sample. After the top cap was positioned, a drive plate containing an electromagnetic drive system was located on top of it. Figure 3.7 shows the drive system

assembled on the sample. The drive system was used to apply a sinusoidal excitation required for the resonant column test. For the torsional tests, four pairs of coils were connected in series inside the drive plate. Thus, a net torque was applied to the sample. The drive system was aligned carefully to make sure that each magnet could move freely within the coils. The device has four leveling screws that allow the experimenter to adjust the height of the drive system where necessary. They also were used to make a rigid connection between the drive plate and the top cap. The top cap was assembled on the drive system at the next level. The purpose of the top plate is twofold: first, to increase the stiffness of the drive system and, second, to incorporate additional transducers such as the LVDT. After being placed accurately and fixed to its position, a LVDT was positioned in place to track any axial displacement of the sample during the test. The cell top with maximum capacity of 1000 kPa was placed on the assembled system. The setup was connected to an air compressor, which allowed changes to the cell pressure within the available range. This was done using a computer controlled valve which controls the cell pressure from the software. Figure 3.7 shows the whole setup for the resonant column test.

Figure 3.7. Left: Drive system on top of the sample. Right: Assembled resonant column apparatus.

To investigate the effect of pressure around the sample on the shear wave velocity and shear modulus, dynamic properties of the samples were tested at five different pressures, from 5 kPa to 100 kPa. GDSLAB software was used to control the cell pressure. It also helped monitoring LVDT (maximum displacement of 10 mm) position and axial displacements.

During the resonant column test, a sinusoidal voltage was applied to the coils, causing the torque to be applied to the specimen. The result was an oscillatory movement in the drive plate. GDS RCA software was used to enter applied voltages with different amplitudes. The range of the frequency of voltage was also entered to the software (2 kHz to 20 kHz). An accelerometer was attached to the drive plate to monitor the amplitude of the vibration. By controlling the frequency and amplitude of the applied voltage, the resonant frequency and the peak output of the sample was obtained as the result of the test. In addition, the maximum output of the accelerometer was plotted against the frequency of applied voltage by the software.

3.4 Data Analysis

This section explains the approaches used to analyze data from the unconfined compression, indentation, piezoelectric ring actuator, and resonant column tests. Methods of statistical analysis used to interpret the results are also described at the end of the section.

3.4.1 Unconfined Compression Test Data Analysis

As explained in Section 3.3.1, force-displacement data were obtained by conducting unconfined compression tests on the samples. The data was then used to investigate material properties of the samples, such as Young's moduli as a function of strain. Methods used for the estimation of the stress-strain data and Young's modulus of the samples at different strains are explained in the following subsection.

3.4.1.1 Stress and Strain Calculation Method

Using the unconfined compression test data and the following equations, stress applied to the sample was calculated as a function of strain.

Initial height and diameter of each sample was measured before the test. Given the initial sample height (H_0), the axial strain of the sample was estimated using equation 3.1 (35), (126):

$$\varepsilon_a = \frac{H - H_0}{H_0} = \frac{\Delta H}{H_0} \tag{3.1}$$

Where:

ε_a	axial strain,
H_0	initial height, mm,
H	height, mm.

Compressive stress can be defined as the amount of compressive force (F) applied to the cross-sectional area of the sample (126). When an axial compressive load is applied to an elastic material, the material expands in the direction perpendicular to the direction of the load to conserve its volume. This lateral expansion caused by a longitudinal compression is called the *Poisson's effect* (127). Due to this effect, the cross-sectional area of the sample is not constant during the test. Equation 3.3 shows the relationship used for calculating the equivalent or corrected area at any given strain (128):

$$A_0 = \pi R^2 \tag{3.2}$$

$$A_c = \frac{A_0}{1 - \varepsilon_a} \tag{3.3}$$

Where:

A_0	initial area, mm^2,
R	sample's radius, mm,
A_c	corrected area, mm^2,
ε_a	axial strain.

Therefore, the axial compressive stress on the sample is:

$$\sigma_a = \frac{F}{A_c} \tag{3.4}$$

$$\sigma_a = \frac{F(1-\varepsilon_a)}{A_0} \quad (3.5)$$

Where:

σ_a	axial stress, MPa,
F	axial force, N,
A_c	corrected area, mm^2,
ε_a	axial strain,
A_0	initial area, mm^2.

Using the above equations, stress versus strain curves were plotted for each sample. Stress-strain curves of PVA-C, similar to soft biological tissues, are nonlinear and most of the equations used for data fitting are exponential in form. Stress-strain curves were fitted according to the following equation 3.6 (129), (130), which has been found to be suitable for representing material responses of soft tissues:

$$\sigma = \alpha\left(e^{\beta\varepsilon_a} - 1\right) \quad (3.6)$$

Where:

σ	axial stress, MPa,
α, β	curve fitting parameters,
ε_a	axial strain.

CurveExpert Professional version 2.5.1 was used to fit the curves and find the curve fitting parameters, as well as the correlation coefficients.

3.4.1.2 Young's modulus Calculation Method

Young's modulus (E), is a measure of the stiffness of the material over a given strain range. During the unconfined compression test, stress and strain were assumed to be uniformly distributed throughout the sample's volume. The relationship between stress and strain for a linear elastic material is known as Hooke's law (Eq. 3.7) (35), (127), (126):

$$\sigma = E\varepsilon \quad (3.7)$$

However, PVA-C is a nonlinear elastic material and the stress-strain curve is also nonlinear. Thus, the Young's modulus is not constant for different ranges of strains. Equation 3.8 was used to calculate the instantaneous Young's modulus at a specific strain:

$$E(\varepsilon_1) = \frac{\sigma(\varepsilon_1)}{\varepsilon_1} \tag{3.8}$$

Where:

ε_1 strain,

$E(\varepsilon_1)$ Young's modulus at $\varepsilon = \varepsilon_1$,

$\sigma(\varepsilon_1)$ stress at $\varepsilon = \varepsilon_1$, MPa.

3.4.1.3 Calculation of Young's Moduli of Rubber Samples

As mentioned before, all of the mechanical tests were also conducted on two rubber samples and the results of these tests were used as a benchmark. Hardness of the rubber samples were obtained by conducting a durometer hardness testing on the samples, and were found to be 39A and 85A for the soft and hard rubber sample, respectively. Gent correlation (149) was used to calculate Young's moduli of the rubber samples:

$$E = \frac{0.0981\,(56+7.62336\times S)}{0.137505\,(254-2.54\times S)} \tag{3.9}$$

Where:

S type A durometer hardness

The value of S in these tests were 39 and 85.

3.4.2 Rigid Indentation Test Data Analysis

Similar to the unconfined compression test, force versus displacement data were acquired from the rigid indentation tests. However, the distribution of pressure is not uniform through the sample during indentation. Therefore, equations more complex than the unconfined compression equations were used to calculate stress, strain, and Young's modulus. Size of the samples was the main factor in determining the method used to solve the problem. In the following section, the equations used to calculate Young's modulus and stress in thick and thin samples are explained.

3.4.2.1 Indentation Analysis of Thick Samples

Rigid indentation tests on large (thick) cylindrical samples can be characterized as an elastic half-space sample under indentation. Sneddon (131) derived the solution of this well-known Boussinesq (132) problem using an elementary solution. According to this solution, the Young's modulus of a half-space deformed by a flat-ended rigid cylinder of known radius can be computed according to the following equations:

$$\mathrm{F} = \frac{4\ \mathrm{E}\ \mathrm{a}\ \mathrm{D}}{1 - \nu}$$

and

$$\mathrm{E} = \frac{\mathrm{F}(1-\nu)}{4\ a\ D} \tag{3.10}$$

Where:

E	Young's modulus, MPa,
F	load, N,
ν	Poisson's ratio, assumed to be 0.5 for an incompressible material,
a	indenter tip radius, 4 mm,
D	indentation depth, mm.

3.4.2.2 Indentation Analysis of Thin Samples

Cao et al. (116), developed an equation to express the relationship between indentation depth and load for finite thickness samples. This equation depends on the size of the indenter and thickness of the sample, as well as the material properties of the sample. They offered the following equation for indentation force which states that the load applied by indenter is a function of Young's modulus, thickness of the sample, and the radius of the indenter.

$$F = \frac{2E}{1-\nu^2} aD\Pi\left(\frac{a}{H_0}, \nu\right) \tag{3.11}$$

Where:

F	load, N,

E	Young's modulus, MPa,
ν	Poisson's ration, 0.5,
a	indenter tip radius, mm,
D	indentation depth, mm,
Π	a dimensionless function,
H_0	initial height of the sample, mm.

Their results showed that the dimensionless function, Π, could change significantly for different values. Thus, they used equation 3.12 to normalize this function:

$$f = 1.03e^{\left(-\frac{a}{5H_0}\right)} + \frac{\pi}{2}\frac{(1-\upsilon)^2}{1-2\upsilon}\frac{a}{H_0}\left[1 - e^{\left(-\frac{a}{H_0}\right)}\right] \quad (3.12)$$

Where e is the exponential function. For the thick samples explained in previous subsection, a/H_0 tends to zero as H_0 increases. Thus, equation 3.12 devolves into Sneddon's solution (equation 3.9). Thin samples, i.e. the mini-pucks with the thickness of 12 mm, were used for this test. For PVA-C mini-pucks indented with a 8 mm-diameter indenter, a/H_0 and Poisson's ratio were equal to 0.33 and 0.5, respectively. In addition, the effect of friction was assumed to be negligible. The value of normalized dimensionless function obtained from curves in (116) was 1.93. Therefore, equation 3.11 reduces to:

$$F = 1.93 \times \frac{2E}{1-\nu^2} aD \quad (3.13)$$

and Young's modulus:

$$E = \frac{F\,(1-\nu^2)}{3.86\ a\ D} \quad (3.14)$$

Where:

E	Young's modulus, MPa,
F	load, N,
ν	Poisson's ratio, 0.5,
a	indenter tip radius, mm,
D	indentation depth, mm.

The Young's moduli of the mini-pucks were calculated using these equations.

3.4.2.3 Load Relaxation Analysis

Load relaxation data were obtained from the indentation of the mini-puck samples, while the position of the indenter tip was kept unchanged. Force against time was plotted for the experimental data. A model proposed by Lin and Hu (2006) was used to analyze the experimental load relaxation data (111). The analysis assumes the material is poroelastic and uses Biot (74) and Scherer (133) based theory. Equation 3.15 was used to estimate the force applied by a smooth circular flat ended indenter at any normalized time (t^*) (83):

$$F(t^*) = 8G_d aD\left[1 - \frac{1-2\nu_d}{1-\nu_d}\frac{Z-(Z^3/3)}{\sqrt{\Pi}}\right] \quad (3.15)$$

and

$$Z = \sqrt{t^*} - 0.23t^* + 0.02t^{*3/2},$$

$$t^* = {}^{t}/_{t_r},$$

$$t_r = {}^{a^2}/_{D_c}$$

Where:

G_d	shear modulus of the drained network, MPa,
a	indenter tip radius, mm,
D	indentation depth, mm,
ν_d	Poisson's ratio of the drained network, 0.22 for drained gel
t	time, s,
t^*	normalized time, s,
t_r	poroelastic characteristic relaxation time, s,
D_c	cooperative diffusion coefficient, m^2/s.

It is also suggested that Equation 3.15 is only valid for the initial portion of the load relaxation curve, where Z<< 1. The value of Z in this project ranged between 0.005 and 0.05 for the initial portion of the load relaxation curve of different samples.

The load relaxation curves obtained from these relaxation experimental tests were fitted using equation 3.15 and the results of this comparison are provided in Section 4.3.2.2.

3.4.3 Piezoelectric Ring Actuator Data Analysis

Signals obtained from the piezoelectric ring actuator were analyzed to calculate the velocity of the shear wave propagation in the samples and, consequently, the reference shear moduli (G_0) of the samples. Methods for calculating arrival time and shear wave velocity of the wave as well as reference shear modulus (i.e. very small strain stiffness) are explained in the following section.

3.4.3.1 Measuring Arrival Time of the shear Wave

The first step in the calculation of the velocity of the shear wave is to properly pick the arrival time of the wave. There are several methods for identifying the arrival time of the shear waves when they are sent by piezoelectric transducers. For all elastic wave methods there is some uncertainty in measuring the travel time of the wave. Some of these uncertainties are because of the problems that can arise due to mixed radiation of the waves, electro-magnetic coupling and cross-talk. There are two general categories of methods for estimating travel time: first, time domain and secondly, frequency domain. Time domain techniques, include the visual picking method, peak-to-peak measuring, and cross-correlation of sent and received signals. A common frequency domain method, is the cross-spectrum wave method. These approaches were used in this study. No specific method has any priority over the other methods (121), (134), (135), (136). The methods are briefly explained further in this section.

Visual picking is the most straightforward method and was widely used in many studies (135), (137). In this method, the first major deflection of the received signal is used as the arrival time of the shear wave. The drawback of this technique is that it is affected by near-field effects with low frequency input waves. As mentioned before, the frequencies of the waves used in this research were less than 15 kHz. Therefore, this method might not be the best method for analyzing the signals.

A second technique used to measure arrival time was the first major peak-to-peak. In this technique, source and received signals are presumed to be highly similar. The shear wave travel time in this method is the time lapse between the peak of the input signal and the first

major peak of the output signal. As a drawback, this method is affected by the quality of the received signals (121), (136).

The cross-correlation method is a measure of the degree of correlation between the output and the input signals. Although this is a time domain technique, the computations, however, are done in the frequency domain using the Fast Fourier Transform. In order to use this technique, the two signals have to be similar and frequency of both waves should be the same order of magnitude. The cross-correlation of an input signal with its response (output signal) is a peak at a time shift that is considered to be the wave travel time between the two points (121), (136).

The cross-spectrum technique is a frequency domain method. In this method, a cross-power spectrum phase diagram versus frequency is plotted. The slope of a linear regression line passing through the data gives the travel time (121), (136).

For the current work, signal analysis software provided by GDS (GDSBEAT) is used to determine arrival time and velocity of the waves propagated inside the PVA-C samples. The software has the ability to perform first arrival, first major peak-to-peak, cross-correlation, and cross-spectrum analysis techniques on the signals.

3.4.3.2 Calculation of Shear Wave Velocity and Reference shear modulus

Travel distance of the wave is the distance between the two piezoelectric plates. The arrival time of a wave, whose measuring methods were explained in the past section, is the time that the shear wave proceeds from the transmitter to the receiver. Shear wave velocity was calculated by equation 3.16 (114), (138), (135):

$$V_s = \frac{H}{t_s} \tag{3.16}$$

Where:

V_s shear wave velocity, m/s,

H travel distance of the wave, mm,

t_s travel time of shear wave, ms.

Reference shear modulus of the sample at near zero strain (G_0) was obtained from shear wave velocity using equation 3.17 (114), (139), (138), (135):

$$G_0 = \rho V_s^2 \tag{3.17}$$

$$\rho = \frac{m}{V} \tag{3.18}$$

Where:

G_0	reference shear modulus, MPa,
V_s	shear wave velocity, m/s,
ρ	mass density of the sample, kg/m^3,
m	density, kg,
V	volume of the sample, m^3.

3.4.4 Resonant Column Test Data Analysis

The result of resonant column test was reported as shear wave velocity and shear modulus as a function of shear strain. Methods for calculation of each of these parameters are explained here.

3.4.4.1 Calculation of Shear Wave Velocity and Shear Modulus

The basic equation for the resonant column is as follows:

$$\frac{I}{I_0} = \zeta \tan(\zeta) \tag{3.19}$$

Where:

I	mass polar moment of inertia of the sample, kg.m^2,
I_0	mass polar moment of inertia of the drive system,
ζ	constant value corresponding with I/I_0.

The value of the mass polar moment of inertia of the drive system (I_0) was found experimentally from resonant column calibration tests (140). The value was 0.0039.

Mass polar moment of inertia defines the ability of a sample to withstand torsion. Cylindrical PVA-C samples were used in this test and their mass polar moment of inertia was obtained from the following equation:

$$I = \frac{md^2}{8} \tag{3.20}$$

Where:

I	mass polar moment of inertia of the sample, $kg.m^2$,
m	density, kg,
d	diameter of the sample, m.

The values of ζ for commonly encountered I/I_0 was obtained from a table in the resonant column system handbook. For example, for I/I_0=0.0171 the value of ζ was 0.1308.

Shear wave velocity was then calculated using the following equation:

$$V_s = \frac{2\pi fH}{\zeta} \tag{3.21}$$

Where:

V_s	shear wave velocity, m/s,
f_n	natural frequency of the sample as found from the resonant column test, Hz,
H	height of the sample, m,
ζ	constant value corresponding with I/I_0.

To calculate shear modulus of the sample, the same equations as for the piezoelectric actuator test were used. Equation 3.18 and 3.17 were used to calculate mass density and shear modulus of the sample respectively.

3.4.4.2 Calculation of Shear Strain

Shear strain was calculated from angle of twist of the sample. Angle of twist is obtained from measurements of acceleration of the drive system, the specimen geometry and the resonant frequency of the sample (141), (142). An accelerometer connected to the drive system was used to measure the acceleration of the drive system. The accelerometer produced a high impedance charge signal proportional to the imposed acceleration, which

requires conditioning to a low impedance voltage suitable for measurement. A charge amplifier was used to achieve this goal. In addition, a transducer sensitivity control on the charge amplifier allowed the sensitivity of the accelerometer to be set based on the transducer gain value. The gain value for this setup was 1000 mv/G.

The charge amplifier was set at 1000 mv/G. Equation 3.27 was used to convert the voltage output from the peak output of G into m/s^2:

$$a_c = 9.81V_t \tag{3.22}$$

Where:

a_c acceleration, m/s^2,

V_t output voltage as reading from the GDS RCA software, volts.

The next step is to calculate the displacement of the accelerometer. The displacement of the accelerometer is related to the angular acceleration by:

$$a_a = \omega^2 Y_{meas} \tag{3.23}$$

and

$$\omega = 2\pi f \tag{3.24}$$

Where:

a_a angular acceleration, m/s^2,

ω angular velocity,

Y_{meas} maximum displacement of the accelerometer,

f_r resonant frequency, Hz.

Therefore, using equations 3.27 and 3.28, the maximum displacement of the accelerometer for a resonance condition is:

$$Y_{meas} = 0.24849 \, {V_t}/{f^2} \tag{3.25}$$

Where:

V_t output voltage, volts,

f_r resonant frequency, Hz.

Angle of twist was measured using the following relationship:

$$\theta = \frac{0.24849\ V}{Kf^2} \tag{3.26}$$

Where:

θ	angle of twist,
K	the offset of accelerometer from the axis of rotation, 0.04325 m.

Finally, shear strain was measured by (58),:

$$\gamma_p = \frac{0.8\ R\ \theta}{H} = \frac{4.596\ V_t\ R}{f^2\ H} \tag{3.27}$$

Where:

γ_p	peak strain,
V_t	output voltage, volts,
R	sample's radius, m,
f_r	resonant frequency, Hz,
H	sample's length, m.

The results of the resonant column test were reported as shear modulus over the shear strain. Following equation was used to fit the experimental data of this test (143):

$$\frac{G}{G_0} = \frac{1}{1+\left(\gamma/\gamma_r\right)^c} \tag{3.28}$$

where

G	shear modulus, MPa,
G_0	reference shear modulus, MPa,
γ	shear strain,
γ_r	reference shear strain,
c	curve fitting parameter.

γ_r is the reference strain value at which $G/G_0=0.5$.

3.4.5 Statistical Analysis

Each test conducted in this study had three replications (each sample was tested for three times), to minimize the risk of error (144). All the calculations including stress, strain, Young's modulus, shear modulus, shear wave velocity, and their means and standard deviations were found using Excel. Error bars in the graphs shown in Chapter 4 present standard deviations of the results. It is assumed that data sets were independent observations of normally distributed random variable. One way and two way ANOVA were used as the method for doing analysis. SigmaStat software version 4.0 was used for ANOVA analysis. SigmaStat makes sure that the assumptions for the ANOVA test, such as normality and equal variance is not violated before running the test. The program shows problems and options if these assumptions do not hold. It also is capable of applying multiple comparison analysis, such as Tukey, if more than two groups of data are compared together. For probability tests, the default p-value 0.05 was used. A report with relevant statistical information was given at the end of each test.

3.5 Summary

In this chapter, materials and methods for preparation of the PVA-S, PVA-H, and PVA-C have been explained. Information about the size and material of the molds used for sample preparation have been provided in detail. The process of freezing and thawing and the most influential factors have been explained. Tests apparatus and configurations for unconfined compression, rigid indentation, piezoelectric ring actuator and resonant column test have been explained. The physical principles of each test and experimental procedures have been provided in detail. Methods of data analysis and theoretical background for interpretations have also been described. Statistical analyses have been explained.

Chapter 4 : Results and Discussion

4.1 Overview

This chapter describes the results of the experiments outlined in the previous chapter and provides discussion of the results. The results of the unconfined compression and rigid indentation tests are shown and the material behavior of PVA-C at large strains are described. The effect of the number of freeze/thaw cycles and PVA concentration on Young's moduli calculated from these tests are explained. Values of shear wave velocity of PVA-C and stiffness for very small strains obtained from the piezoelectric ring actuator setup are presented. Shear wave velocity and shear modulus obtained from the resonant column tests are shown and the behavior of the material at small strains (<0.1) is described. The results of statistical analysis on each data set are provided. All of the results are summarized and compared to those of benchmark elastomers (rubber). The similarities between the material behavior of the hydrogels (PVA-C), elastomers, and some biological tissues are discussed.

4.2 Unconfined Compression Testing

The results of unconfined compression tests show the mechanical behavior of PVA-C for large strains. Results of stress as a function of strain for samples with different polymer concentrations and different numbers of freeze/thaw cycles, as well as calculated Young's moduli, are shown in this section. The majority of the tests were conducted at strain rates of 0.17 s^{-1} and these tests are assumed to be quasi-static at this rate of strain (89). Stress-strain curves of tests with different strain rates are also compared to show the effect of the rate of deformation on the mechanical properties. There is also a comparison between the results of the tests conducted on mini-pucks versus those conducted on larger cylindrical samples, to show the effect of sample size on the estimated properties.

4.2.1 Stress-strain Behavior

Conducting unconfined compression experiments on PVA-C allows us to generate stress-strain curves. The methods of creating these curves parameters were explained previously in Section 3.4.1. The results are sub-divided based on their main aspects of interest.

4.2.1.1 Effect of PVA Concentration

Figures 4.1 to 4.3 show the stress-strain curves for mini-puck samples with 5% to 20% PVA concentration after 2, 4, and 6 freeze/thaw cycles, respectively, during loading phase. The stress-strain curves of two rubber benchmark samples with durometer measurements of 39A and 85A are also added to the graph for the purpose of comparison. As shown in the graphs, the PVA-C samples display nonlinear stress-strain relationships. The slopes of the curves, which are not constant at different strains, reveal the strain dependent Young's moduli or stiffness of the samples.

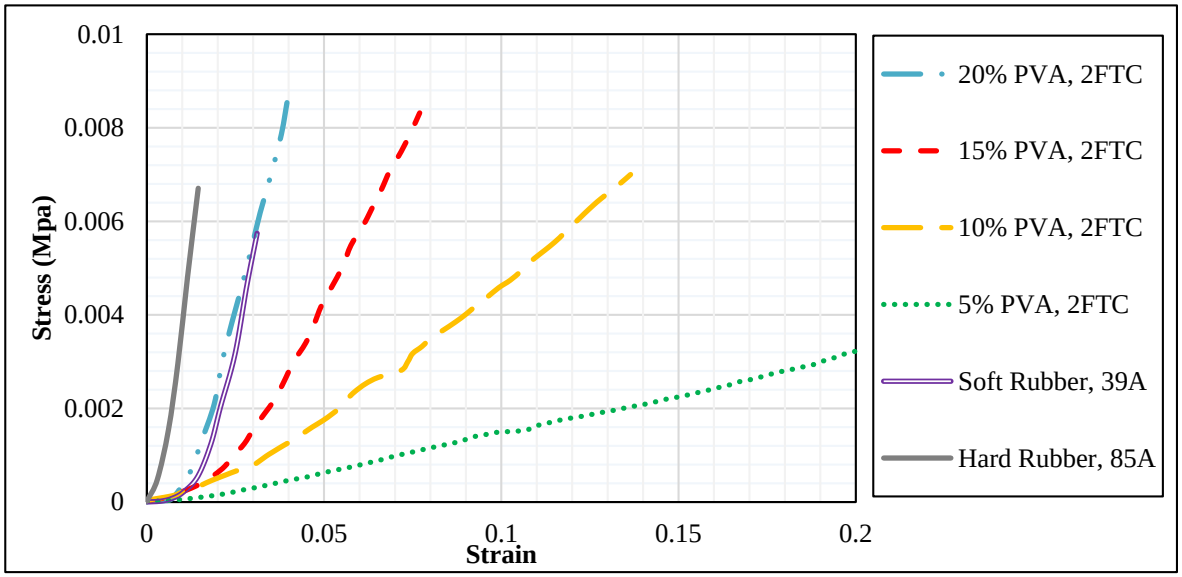

Figure 4.1. Loading stress-strain curves for unconfined compression of PVA-C samples after 2 FTCs, along with curves obtained from two rubber samples.

As shown in the figures, increasing the PVA concentration of the PVA-C results in an increase in the slope of the stress-strain curves and therefore, the stiffness. In all samples, higher stress values were found for higher strains. This general trend of increase in the stiffness with increasing polymer concentration is evident for the different freeze/thaw

cycle repetitions as well. The two rubber samples behaved similarly to the PVA-C samples and showed higher stress values as the strain increased. It is also shown that the stress-strain curve of hard the rubber sample with the durometer value of 85A has a higher slope than the curve for the soft rubber sample with the durometer value of 39A.

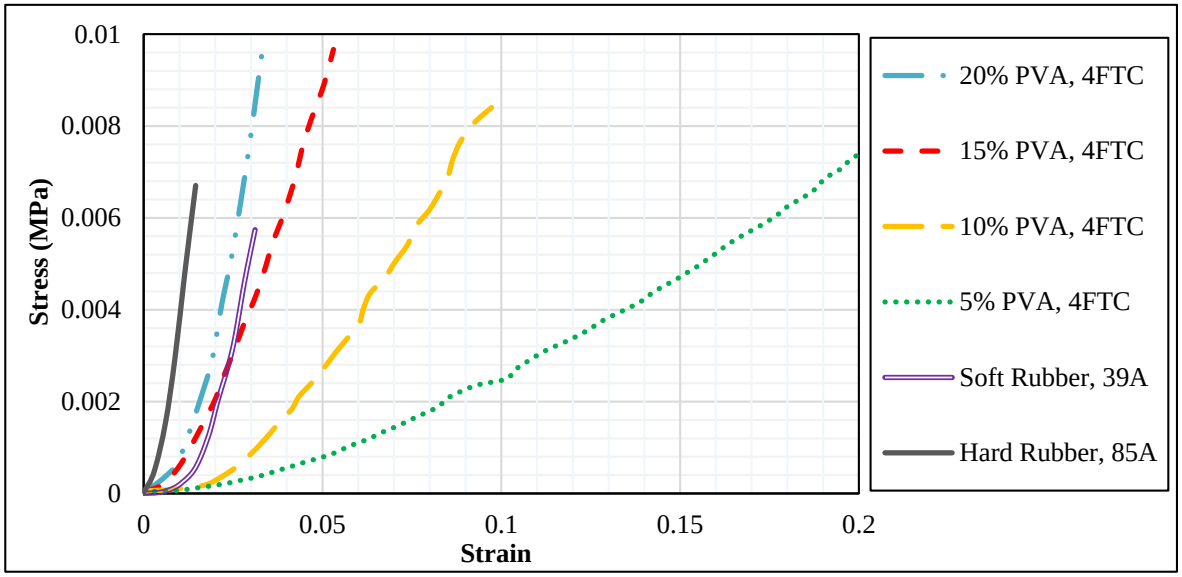

Figure 4.2. Loading stress-strain curves for unconfined compression of PVA-C samples after 4 FTCs, along with curves obtained from two rubber samples.

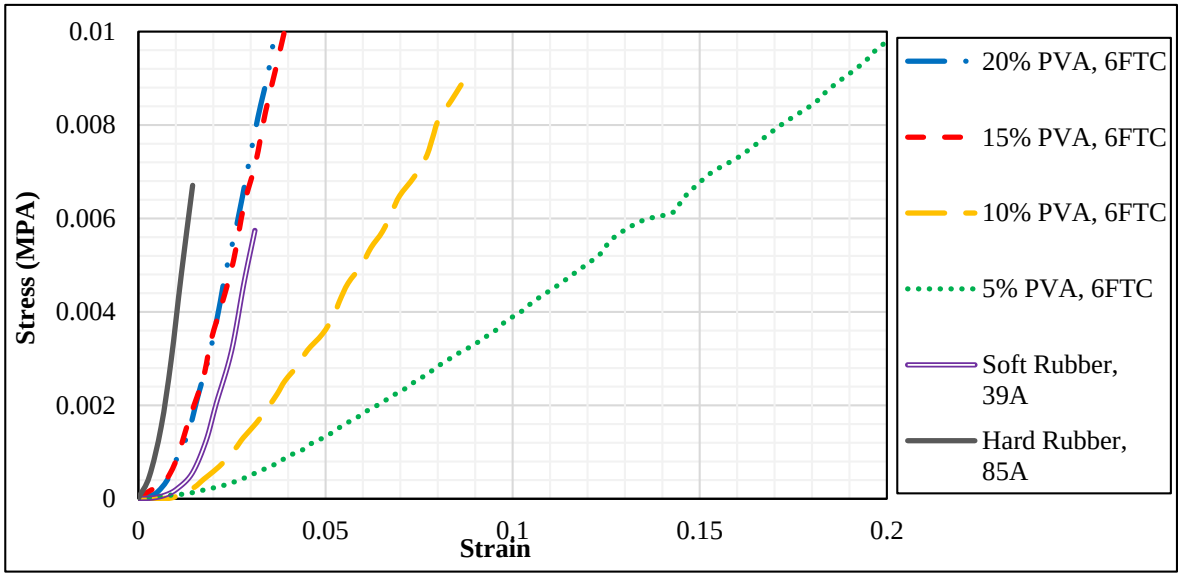

Figure 4.3. Loading stress-strain curves for unconfined compression of PVA-C samples after 6 FTCs, along with curves obtained from two rubber samples.

As shown in Figure 4.1, the stiffest PVA-C material, which is 20 % PVA, has a similar stress-strain curve to the soft rubber sample. By increasing the number of FTCs, PVA-C samples become stiffer. As shown in Figures 4.2 and 4.3, 15% and 20% PVA samples with 4 and 6 FTCs have curves with higher slopes than that for the soft rubber sample. The relationship between stiffness and number of freeze/thaw cycles is explained in more detail in Section 4.2.1.2.

Stress-strain curves shown in Figures 4.1 to 4.3 were fitted to the equation 3.6. Table 4.1 provides these curve fitting parameters and the correlation coefficients for equation 3.6. All the curve fitting parameters and correlation coefficients in this table and also in the future tables are based on the average curve values.

Table 4.1 Stress-strain curve fitting parameters for samples with different PVA concentrations

	α (MPa)	**β**	**r***
5% PVA, 2 FTC	0.9657 ± 0.094	0.0141 ± 0.0015	0.984
10% PVA, 2 FTC	0.0053 ± 0.0007	6.2373 ± 0.4173	0.999
15% PVA, 2 FTC	0.0041 ± 0.0014	15.6829 ± 2.5944	0.995
20% PVA, 2 FTC	0.0023 ± 0.001	40.8553 ± 6.4254	0.989
5% PVA, 4 FTC	0.0037 ± 0.0004	5.5143 ± 0.2954	0.998
10% PVA, 4 FTC	0.0038 ± 0.0013	13.9337 ± 1.4508	0.992
15% PVA, 4 FTC	0.0036 ± 0.0005	27.0810 ± 0.9967	0.997
20% PVA, 4 FTC	0.0015 ± 0.0004	63.3186 ± 6.9552	0.998
5% PVA, 6 FTC	0.0056 ± 0.0008	5.109 ± 0.429	0.997
10% PVA, 6 FTC	0.0021 ± 0.0001	16.7408 ± 0.247	0.999
15% PVA, 6 FTC	0.0018 ± 0.0009	36.1806 ± 3.6021	0.992
20% PVA, 6 FTC	0.0019 ± 0.0004	49.5256 ± 1.3452	0.993
Soft Rubber (39A)	0.0002 ± 0.0001	108.3368 ± 5.996	0.995
Hard Rubber (39A)	0.0021 ± 0.00002	115.003 ± 10.1385	1.000

*Correlation coefficient

Correlation coefficient is a measure that determines the degree to which experimental data and the data obtained from fitting equation are related. The value of correlation coefficient varies between -1 to 1. If the correlation coefficient is 1, there is a perfect positive relationship between the two variables (54).

The relationship between the curve fitting parameters and sample properties is shown in Figure 4.4 which is plotted based on the parameters obtained from samples with different PVA concenterations after 2 FTCs.

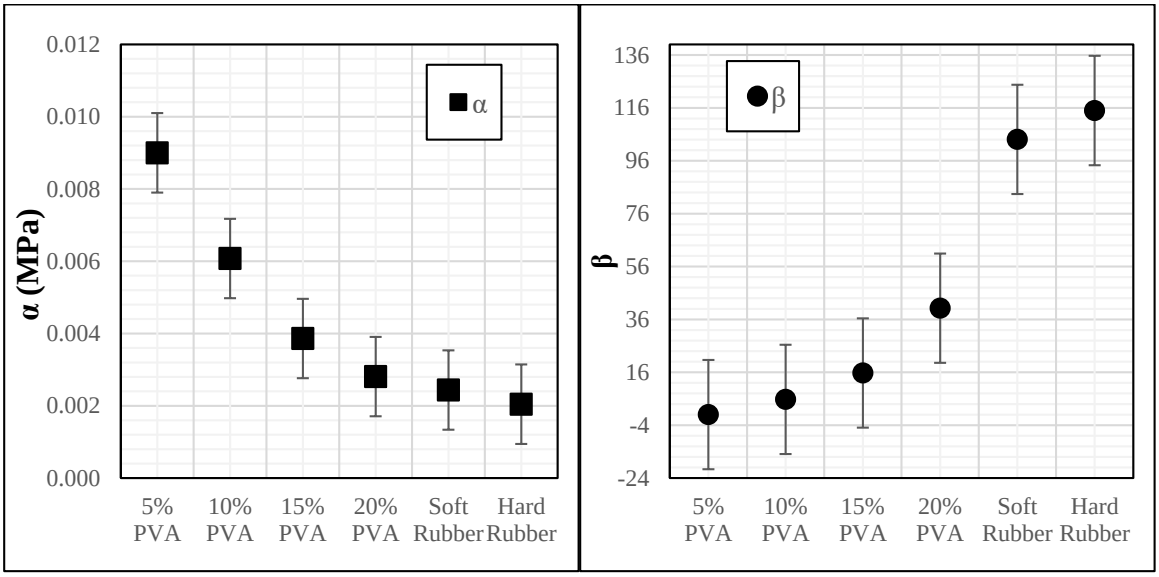

Figure 4.4. Stress-strain curve fitting parameters α (left) and β (right) for samples with different PVA concentrations after 2 FTCs.

As shown in Table 4.1 and Figure 4.4 for samples with 2 FTCs, the curve fitting parameter α has an inverse relationship with the stiffness of the samples. It is shown that increases in PVA concentration of the samples results in lower values for the curve fitting parameter α. This trend is also seen in samples with 6 FTCs (See Appendix B, Figure B.4). For samples with 4 FTCs (see Appendix B, Figure B.3), α is essentially constant for 10% and 15% PVA concentration but decreases for the sample with 20% PVA concentration. The value of α is higher for the soft rubber (39A) sample than the harder one (85A).

The curve fitting parameter β also has a positive correlation with the stiffness. As the PVA concentration of the samples increases, values of β increase significantly. The relationship between curve fitting parameter β and PVA concentration for samples with 2 FTCs is

shown in Figure 4.4. This trend is also seen in samples with 4 and 6 FTCs (Table 4.1). The values of β in rubber samples follow a similar pattern and the hard rubber (85A) sample has a higher β value than the soft rubber (39A) sample.

4.2.1.2 Effect of Number of Freeze/thaw Cycles

Figures 4.5 to 4.8 show the effect of the number of freeze/thaw cycles on the stress-strain behavior of the materials. In each figure, the PVA concentration of the mini-puck sample is constant and the number of cycles is either 2, 4, or 6. The results of the tests on the two samples of rubber are also added to each figure for comparison.

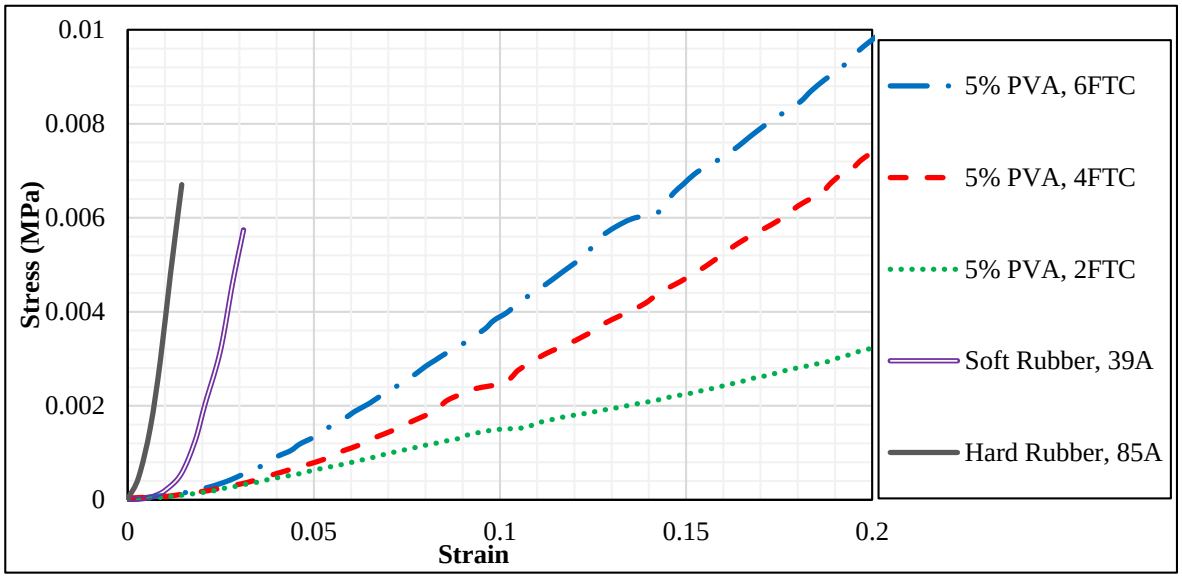

Figure 4.5. Loading stress-strain curves for unconfined compression of 5% PVA after different freeze/thaw cycles.

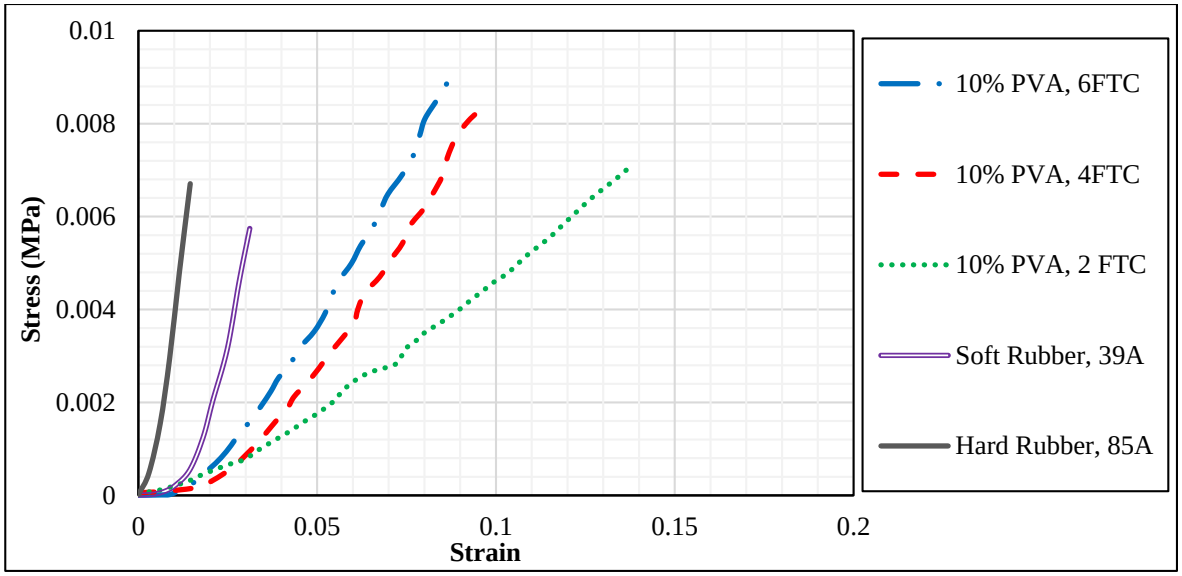

Figure 4.6. Loading stress-strain curves for unconfined compression of 10% PVA after 2, 4, and 6 freeze/thaw cycles.

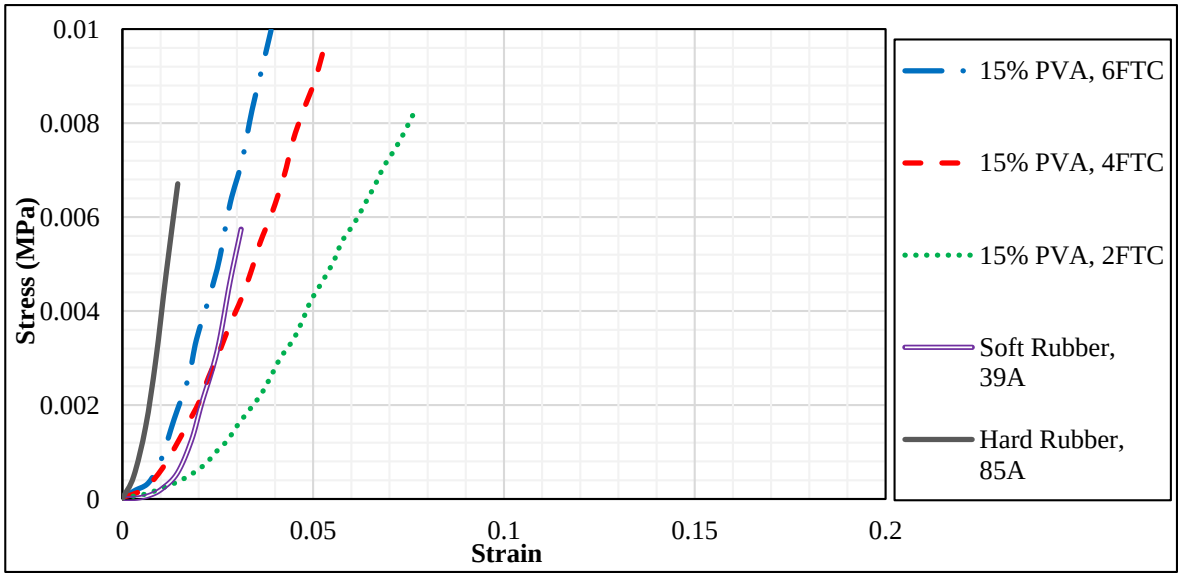

Figure 4.7. Loading stress-strain curves for unconfined compression of 15% PVA after 2, 4, and 6 freeze/thaw cycles.

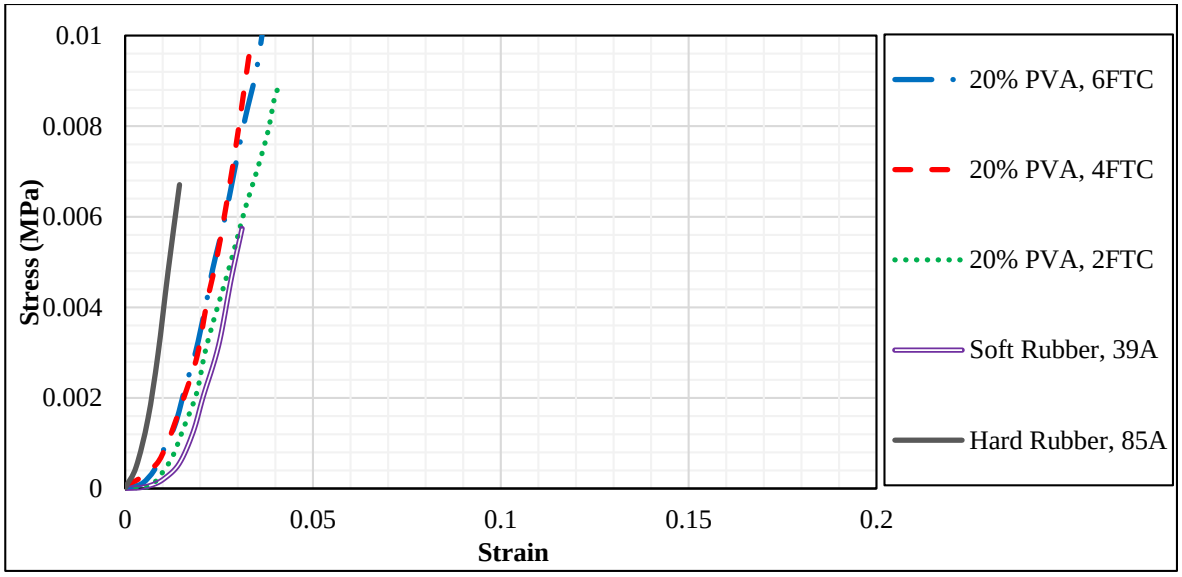

Figure 4.8. Loading stress-strain curves for unconfined compression of 20% PVA after 2, 4, and 6 freeze/thaw cycles.

As shown in the figures, for a given concentration there is a rise in the slope of the stress-strain curves as the number of freeze/thaw cycles increases. Therefore, an increase in the number of cycles results in samples with higher stiffness. Comparison of Figures 4.5 to 4.8 show that as the percentage of PVA increases, slopes of the stress-strain curves of the samples begin to converge on that of the soft rubber sample. For the samples with 20% PVA concentration, the slope of the curves are higher than the soft rubber sample for any FTC number.

Equation 3.6 was again used to fit the stress-strain plots. Table 4.2 provides these curve fitting parameters for equation 3.6. Correlation coefficients (r^*) are based on the average curve values and in the range of 0.995-0.999. This demonstrate that this equation provides a reasonable fit to the data. The values of the curve fitting parameters follow the general trend explained in Section 4.2.1.1. Comparison of the values in Table 4.2 show that the curve fitting parameter α decreased as the number of FTCs increased. However, this value was not significantly different among samples with different numbers of freeze/thaw cycles with higher polymer concentration (20% PVA). Additionally, the value of α was very similar for the soft and hard rubber samples.

Table 4.2. Stress-strain curve fitting parameters for samples with different numbers of freeze/thaw cycles

	α (MPa)	β	r*
5%PVA, 2 FTC	0.9657 ± 0.094	0.0141 ± 0.0015	0.984
5%PVA, 4 FTC	0.0037 ± 0.0004	5.5143 ± 0.2954	0.998
5%PVA, 6 FTC	0.0056 ± 0.0008	5.109 ± 0.429	0.997
10% PVA, 2 FTC	0.0053 ± 0.0007	6.2373 ± 0.4173	0.999
10% PVA, 4 FTC	0.0038 ± 0.0013	13.9337 ± 1.4508	0.992
10% PVA, 6 FTC	0.0021 ± 0.0001	16.7408 ± 0.247	0.999
15% PVA, 2 FTC	0.0041 ± 0.0014	15.6829 ± 2.5944	0.995
15% PVA, 4 FTC	0.0036 ± 0.0005	27.0810 ± 0.9967	0.997
15% PVA, 6 FTC	0.0018 ± 0.0009	36.1806 ± 3.6021	0.992
20 % PVA, 2 FTC	0.0023 ± 0.001	40.8553 ± 6.4254	0.989
20 %PVA, 4 FTC	0.0015 ± 0.0004	63.3186 ± 6.9552	0.998
20% PVA, 6 FTC	0.0019 ± 0.0004	49.5256 ± 1.3452	0.993
Soft Rubber (39A)	0.0002 ± 0.0001	108.3368 ± 5.996	0.995
Hard Rubber (85A)	0.0021 ± 0.00002	115.003 ± 10.1385	1.000

*Correlation coefficient

Figure 4.9 shows the relationship between curve fitting parameters and the number of freeze/thaw cycles for samples with 10% PVA. (See Appendix B, Figures B.5 and B.6 for 5% and 20% PVA, respectively)

For all of the samples with similar PVA concentration, the fitting parameter β was significantly different when the number of cycles changed from 2 to 4. However, this difference was not significant between 4 and 6 freeze/thaw cycles. This trend is seen clearly in Figures 4.6, 4.7, and 4.8. Previous studies showed that there is no change in the stiffness of the material after reaching 7 freeze/thaw cycles (100).

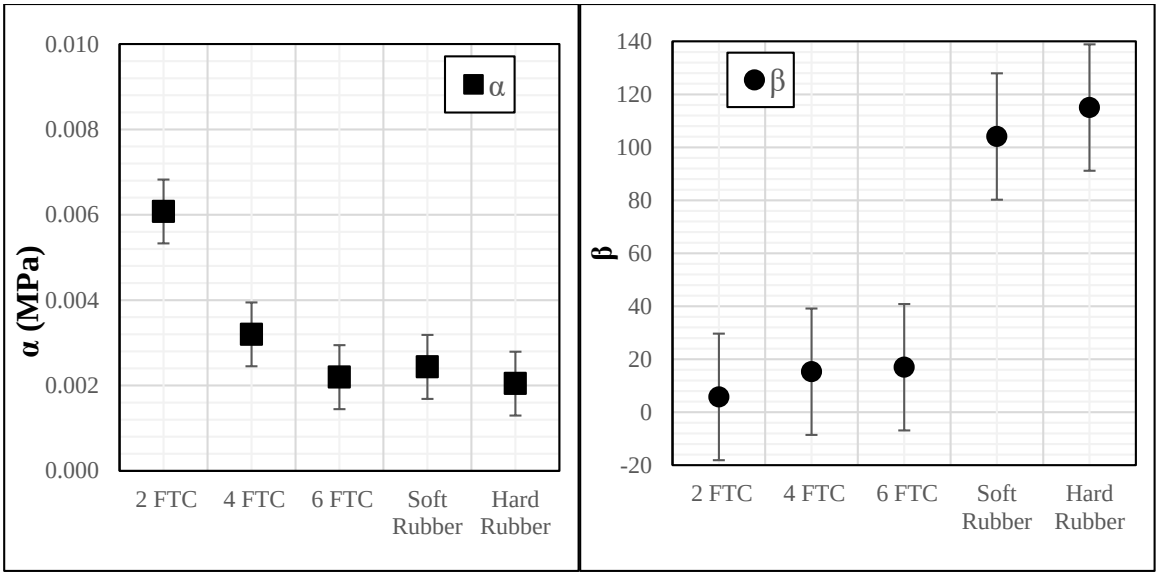

Figure 4.9. Stress-strain curve fitting parameters α (left) and β (right) for 10% PVA samples with different numbers of freeze/thaw cycles.

As shown in Figure 4.8, slopes of the stress-strain curves of 20% PVA samples with different numbers of FTCs are approximately similar and the stiffness is not significantly increasing as the number of cycles increases. This shows that the effect of the number of freeze/thaw cycles on PVA-C stiffness does not affect the samples independently and also has a correlation with PVA concentration of the sample.

4.2.1.3 Effect of Strain Rate

Two different rates of loading were applied to the mini-puck samples as described in Section 3.3.1. Figure 4.10 shows the stress-strain curves of the softest (5% PVA, 2FTC) and the stiffest (20% PVA, 6FTC) samples at two different strain rates of 0.17 s^{-1} and 0.017 s^{-1}. As shown in the figure, the slope of the PVA-C curves increase slightly with increase in the strain rate. This may be due to the apparent viscoelastic nature of the PVA-C. As a viscoelastic material, the rate at which the load is applied to the sample affects the estimated mechanical properties of the sample. The stiffness of sample increases when the load is applied at a higher rate (145). At this strain rates the changes in the rubber material response are negligible. However this may also be a poroelastic phenomenon, so some caution is required in the interpretation of the rubbers.

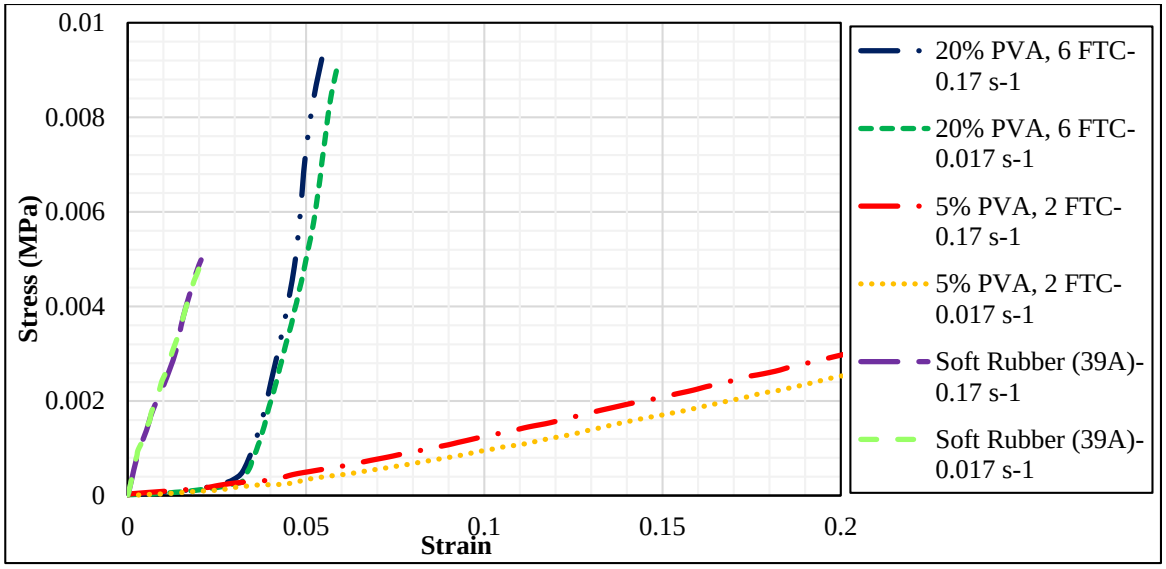

Figure 4.10. Stress-strain curve for unconfined compression of 5% and 20% PVA, 2FTC samples, along with a soft rubber (39A) sample at two different strain rates.

The curves in Figure 4.10 were also fitted by equation 3.6. The value of the curve fitting parameter α decreased as the strain rate increased. However, the difference between the value for 0.17 s^{-1} and 0.017 s^{-1} was not significant. Curve fitting parameter β had a positive relationship with strain rate. However, the increase in the value of β is not significant when the strain rate increases from 0.17 s^{-1} and 0.017 s^{-1}. The same trend is observed in the soft rubber sample. It shows that for stiffer samples, larger differences in strain rate are necessary to see significant changes in the stiffness. Unfortunately, it was not possible to test more dispersed strain rates, due to limitations of the loading equipment.

Previous uniaxial compression tests on rubbers show that the effect of the strain rate on Young's moduli of the rubber is higher when the strain rates are between 10 s^{-1} and 1000 s^{-1}, in comparison to strain rates between 0.001 s^{-1} to 10 s^{-1} (146), (147). Therefore, the strain rates used in this project (0.17 s^{-1} and 0.017 s^{-1}) fall into the latter range of strain rate, where the stiffness of the rubber sample is less dependent on the strain rate. In another study, uniaxial compression and tension stress-strain curves of rubber and pig skin were compared at 0.4, 0.004, 40, and 4000 s^{-1} strain rates. The results revealed that for both rubber and pig skin, the level of stress increases at higher strain rates, but the shape of stress-strain curves are not affected (148). The results of other researchers tests conducted

on PVA hydrogel also showed that elastic and shear moduli are not significantly affected as the strain rate changes from 0.017 s^{-1} to 0.17 s^{-1} (89).

4.2.1.4 Effect of Sample Thickness

To investigate the effect of sample thickness on the stiffness, the results of unconfined compression tests on large cylindrical samples (50 mm diameter and 100 mm height) were compared to those already shown from the mini-pucks (38 mm diameter and 12 mm height).

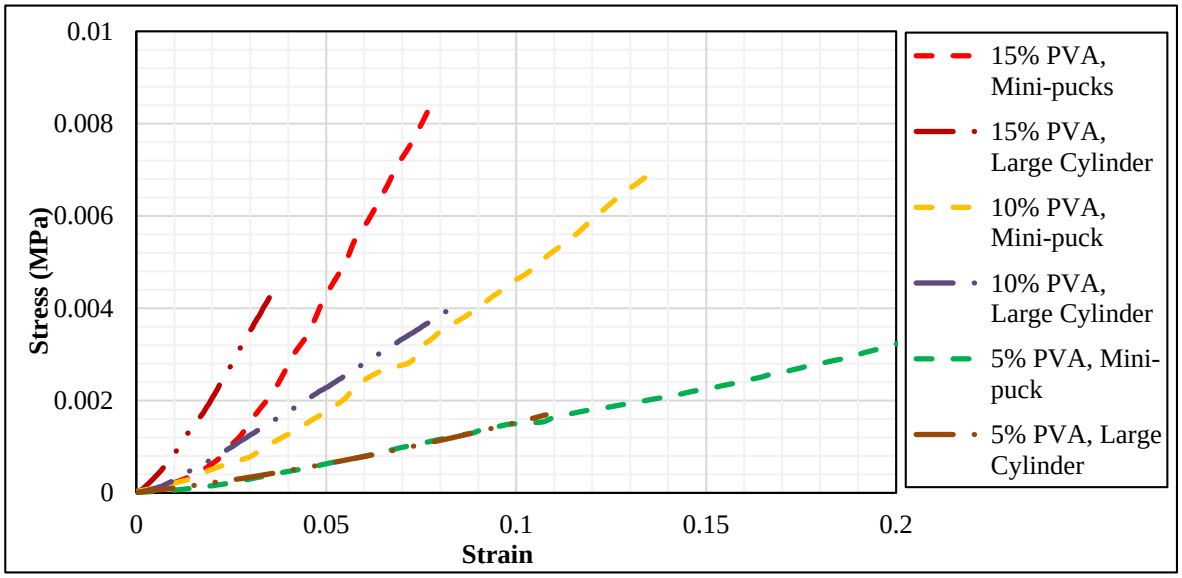

Figure 4.11. Comparison of stress-strain curves of large cylindrical and mini-puck samples of different PVA concentration after 2 FTCs.

Figure 4.11 compares the stress-strain curves of large and mini-puck samples with 5%, 10%, and 15% PVA concentration after 2 FTCs. It is shown that in the softest sample, 5% PVA with 2 FTCs, there is no difference between the curves of the mini-puck and the large cylinder. Therefore, the thickness of the samples does not seem to affect the stiffness of PVA-C samples with 5% PVA, 2 FTCs. However, is also shown in the figure that for both 10% and 15% PVA, 2FTCs the curves for thicker samples have higher stress in similar strains and therefore, they are apparently stiffer than the mini-pucks. Samples with 15% PVA and 2FTCs showed the most difference among the curves for the large cylinder and mini-puck.

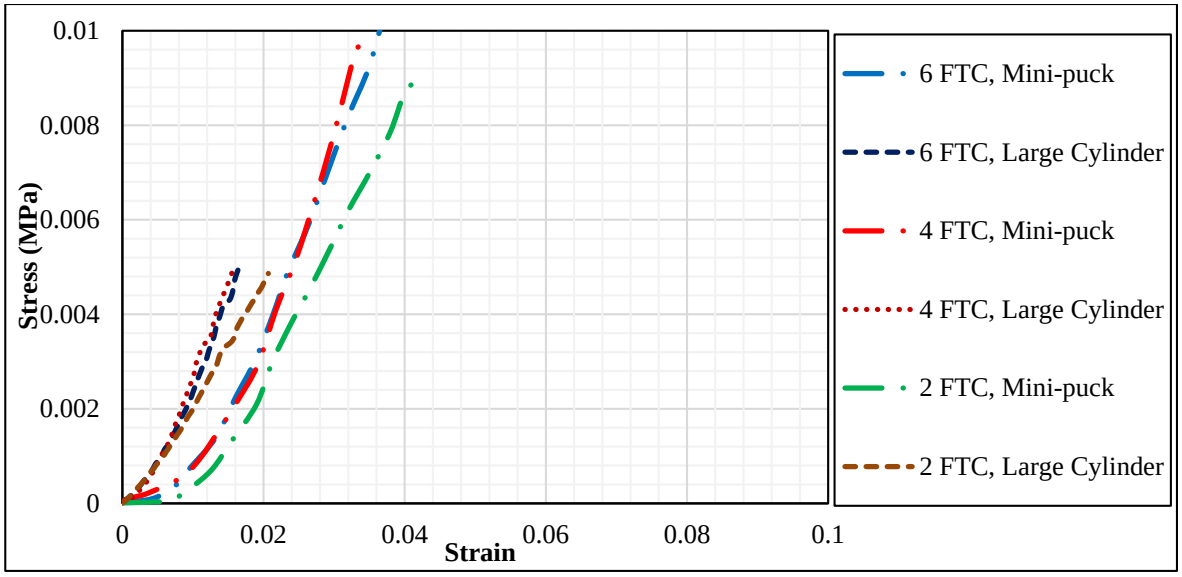

Figure 4.12. Comparison of stress-strain curves of large cylindrical and mini-puck samples with 20% PVA concentration at different FTCs.

Figure 4.12 shows the stress-strain curves of the 20% PVA samples with different numbers of freeze/thaw cycles and different thicknesses. As seen in the figure, the large cylinders are stiffer than the mini-pucks for all three different FTCs. The stress-strain curves for 20% PVA with 4 FTCs converge with those for 6 FTCs in the mini-puck samples. The same trend occurs for large cylinders of 20% PVA with 4 and 6 FTCs and therefore, the difference between large cylinders and mini-pucks is similar in these two samples. Stress-strain curves of 20% PVA samples with 2FTCs have lower slopes than those with 4 and 6 FTCs but the difference between thick and thin samples is similar to those of the stiffer samples. Therefore, the difference between the large cylinders and the mini-pucks is not affected by the number of FTCs in this group of materials.

These results do not meet the initial expectations of the study design that sample size is not a significant factor in the observed stress-strain behavior. This difference could arise due to different thicknesses, inhomogeneity of larger samples (113), and poroelastic material response of the PVA-C. For a poroelastic material the compressive force response will scale with a characteristic time r^2/D_c, where r is the sample diameter and D_c is the cooperative diffusion coefficient. This has been described by Biot (1941) for fluid flow and D_c is a function of elastic modulus, network permeability, and viscosity gel liquid phase (74). If the samples are large enough for this characteristic poroelastic time to be significant, then

this would potentially affect the bigger samples more; this effect would not be expected in viscoelastic materials (77). Inhomogeneity of the large cylinders can also cause the difference in stiffness. Previous research has shown that the increase in diameter of the PVA-C samples directly affects the inhomogeneity through the sample (113). The diameter of the large cylinders in this project is 50 mm, as opposed to that of mini-puck samples which is 38 mm. The larger diameter may lead to more inhomogeneity in the cylindrical samples than the mini-pucks and could affect the stress-strain behavior and cause difference in samples with different sizes.

Table 4.3. Curve fitting parameters for samples with different thicknesses.

		α (MPa)	**β**	**r***
5% PVA, 2 FTCs	**Large Cylinder**	0.9694 ± 0.081	0.0148 ± 0.0022	0.990
	Mini-puck	0.9657 ± 0.094	0.0141 ± 0.0015	0.984
10% PVA, 2 FTCs	**Large Cylinder**	0.0065 ± 0.0006	5.6835 ± 0.1293	0.999
	Mini-puck	0.0053 ± 0.0007	6.2373 ± 0.4173	0.999
15% PVA, 2 FTCs	**Large Cylinder**	0.0038 ± 0.0002	19.6186 ± 3.3736	0.999
	Mini-puck	0.0041 ± 0.0014	15.6829 ± 2.5944	0.995
20% PVA, 2 FTCs	**Large Cylinder**	0.0057 ± 0.0027	30.7158 ± 4.6468	0.996
	Mini-puck	0.0023 ± 0.001	40.8553 ± 6.4254	0.989
20% PVA, 4 FTCs	**Large Cylinder**	0.002 ± 0.0012	80.6778 ± 3.9013	0.995
	Mini-puck	0.0015 ± 0.0004	63.3186 ± 6.9552	0.998
20% PVA, 6 FTCs	**Large Cylinder**	0.0019 ± 0.0002	77.8225 ± 4.05	0.998
	Mini-puck	0.0019 ± 0.0004	49.5256 ± 1.3452	0.993

*Correlation coefficient

Table 4.3 provides curve fitting parameters for the stress-strain curves in Figures 4.11 and 4.12. Equation 3.6 was again used to fit these curves. As shown in the table, the curve fitting parameter α is very similar for the large cylinder and the mini-puck of 5% PVA with 2 FTC and the difference between the β parameters is also negligible. For 10% PVA, 2FTC the value of α is higher in the large cylinders than the mini-pucks. However, β value of the mini-puck sample is larger than those for the large cylinder. For 15% PVA sample with 2

FTC, α is slightly higher in the mini-puck sample while its β value is lower than the large cylinder. Comparison of the curve fitting parameters of 15% PVA, 2FTC samples shows that the thickness of the samples does not affect the values of α parameter and it is very similar in the mini-puck and large cylinder. However, the β value is lower in the mini-puck sample. 20% PVA, 2FTC samples show the highest difference in α values among the samples with different thicknesses. The value of β is larger in the mini-puck sample. In 20% PVA, 4 and 6 FTC samples the value of β is higher in the large cylinders. In 20 % PVA, 4FTC samples the values of α slightly increase as the sample become thicker. However, there is no difference between α values of large cylinders and mini-puck samples of 20% PVA, 6 FTC.

4.2.2 Young's Modulus

Young's moduli of the samples at 3% strain were calculated using equation 3.7. As implied by Figure 4.13, the Young's modulus increases with increasing PVA concentration of the samples. It is also suggested that higher numbers of freeze/thaw cycles lead to larger Young's moduli. Two way ANOVA was conducted on the samples in each group. The results of the statistical analysis showed that Young's moduli of the samples are significantly different ($P<0.001$).

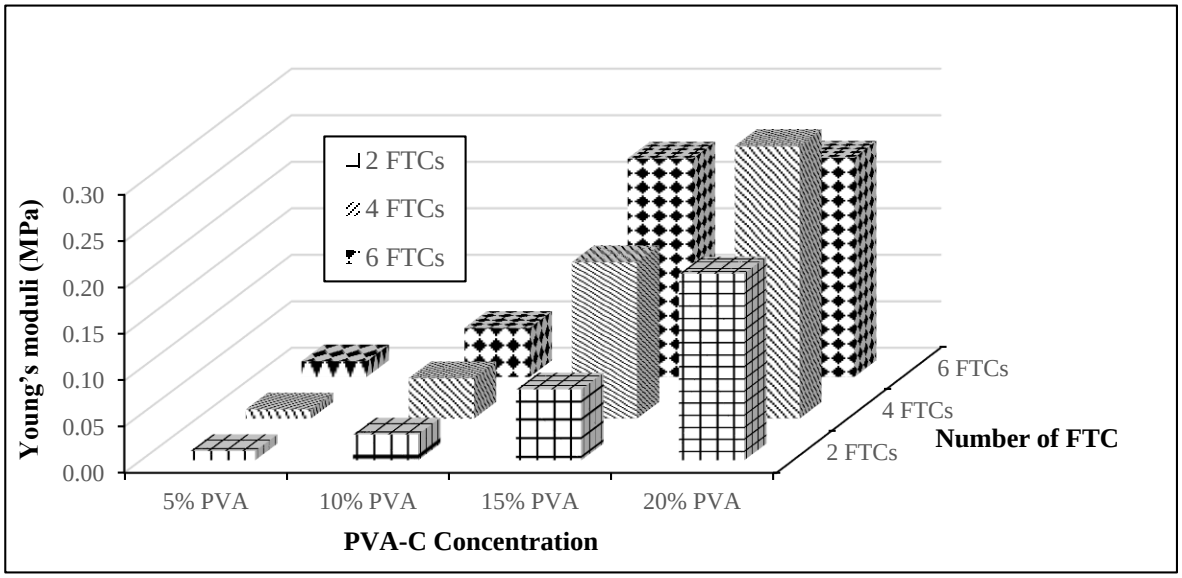

Figure 4.13. Young's moduli of all the samples at 3% strain obtained from the unconfined compression test.

As a nonlinear elastic material, the stiffness of PVA-C is not constant over different ranges of strain. Figure 4.14 compares the value of Young's moduli of 5%, 10%, 15%, and 20% PVA with 2 FTCs, at 1% and 3% strain. These values are also provided in Table B.1 in Appendix B.

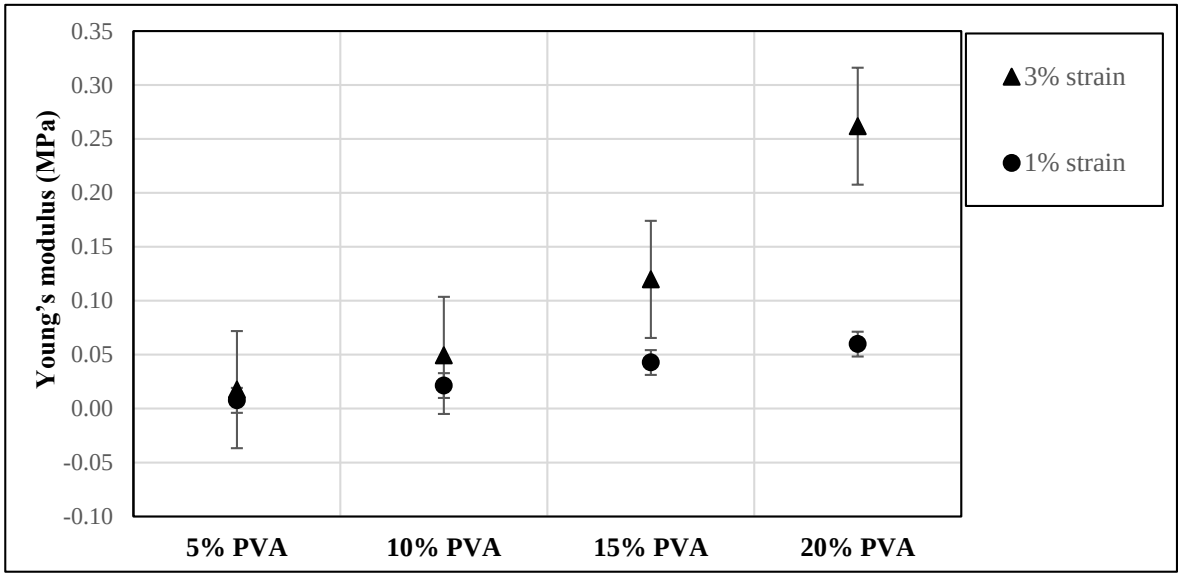

Figure 4.14. Young's moduli of different samples at 1% strain and 3% strain

As illustrated in Figure 4.14, for the softest sample (5% PVA, 2FTCs) the difference between the Young's moduli for the two different strain percentages is not significant. As the PVA concentration of the samples increases, the difference between Young's moduli for 1% and 3% strain becomes more significant. It was not possible to obtain the Young's moduli for strain ranges beyond these values due to the limits of the UC test device. The value of Young's moduli significantly increases in stiffer samples (15 % PVA and 20% PVA, 2 FTCs) as the percentage of strain increases.

4.3 Indentation Testing

Indentation tests were conducted on the samples based on the procedures described in Section 3.3.2. Force and displacement data were recorded with GETDATA software. Figures C.1 and C.2 in Appendix C show indentation force against displacement for the mini-puck PVA-C samples. As mentioned in Section 3.4.2, there are different methods for estimating Young's modulus and stress-strain for samples with different thickness.

Therefore, the results of indentation of thick and thin samples are explained in the following two sections.

4.3.1 Indentation of Thick Samples

For the indentation analysis of the large cylindrical samples were assumed to behave as elastic half-spaces. Results of the tests and calculations are presented below.

4.3.1.1 Young's moduli

Young's modulus of each cylindrical sample was calculated based on equation 3.10. Results of this calculations for 3% strain at the center of the indenter are provided in Table C.1 (Appendix C) and compared in Figure 4.15. As seen in the figure, for samples with PVA concentrations of 20%, Young's modulus increases as samples go through more freeze/thaw cycles. Also, an increase in the PVA concentration of the samples with similar numbers of freeze/thaw cycles, results in an increase in Young's modulus and, therefore, stiffness of the sample. Results of the ANOVA tests also showed that these values are significantly different ($P<0.05$).

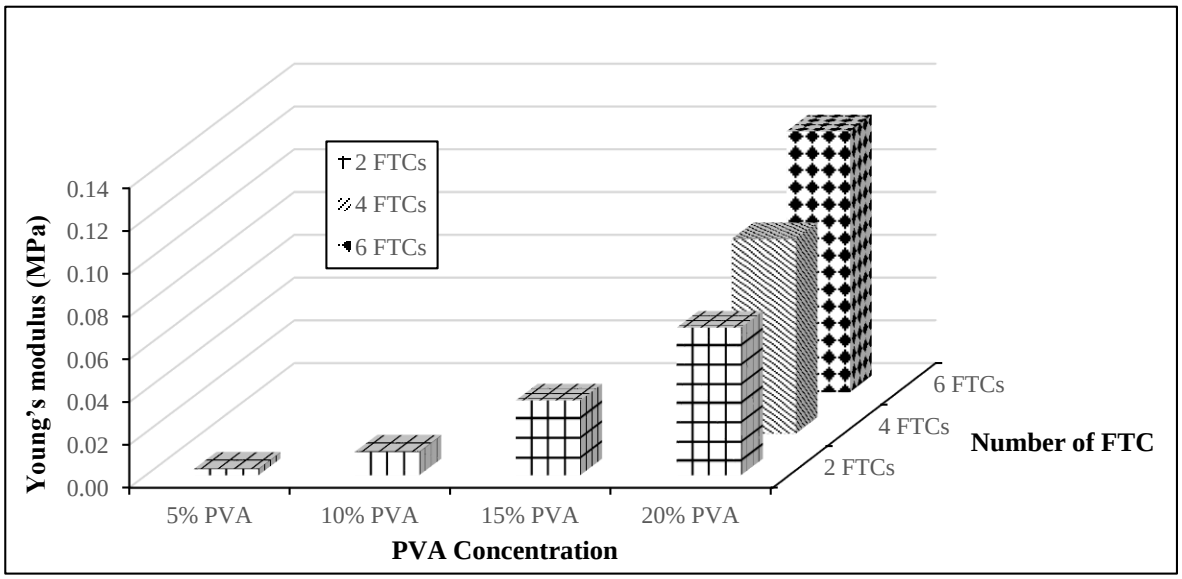

Figure 4.15. Young's moduli for all of the large cylindrical PVA-C samples at 3% strain obtained from rigid indentation tests.

To investigate the effect of strain percentage on Young's moduli of the samples, values of the Young's moduli were compared at two different strains, 0.5% and 3%. Figure 4.16 shows the results of this comparison.

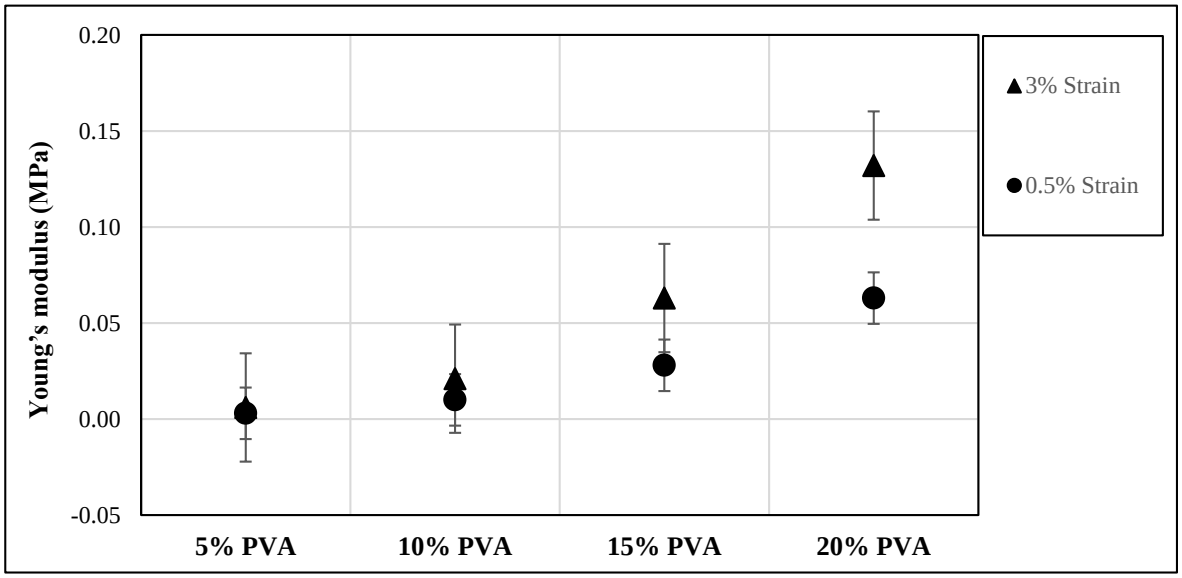

Figure 4.16. Comparison of the Young's moduli of large PVA-C samples of 5%, 10%, 15%, and 20% PVA with 2 FTCs at 0.5 % strain and 3% strain.

It is shown that the material becomes stiffer as the strain increases. This is due to the fact that as the indentation depth increases, the polymer chains of the PVA-C compress and therefore, Young's moduli increases.

4.3.2 Indentation of Thin Samples

Indentation was also conducted on mini-pucks as described in Section 3.3.2. Results of the calculated Young's moduli of the samples are as follows.

4.3.2.1 Young's modulus

Young's moduli of the mini-pucks were calculated using equation 3.14. Figure 4.17 shows the values of Young's moduli for all samples at 3% strain. Table C.2 in Appendix C provides these values in the format of average ± standard deviation. Young's modulus of the soft rubber is also shown for the purpose of comparison. As shown in the figure, the indentation Young's modulus of the soft rubber (39A) sample is 0.681 MPa. Young's

modulus of the soft rubber when indented for about 10% was calculated from equation 3.9 and found to be 1.627 MPa (149). This difference arises from the different test conditions and different strain values at which the Young's modulus is calculated. Unfortunately, it was not possible to calculate this value for hard rubber at this strain, since the largest strain at this load was 1% for the hard rubber sample. It can be seen that Young's moduli of the samples increase as their PVA concentration and number of FTCs increase. However, the difference between stiffer samples (e.g. 20% PVA, 4 and 6 FTCs) is not significant (P>0.05).

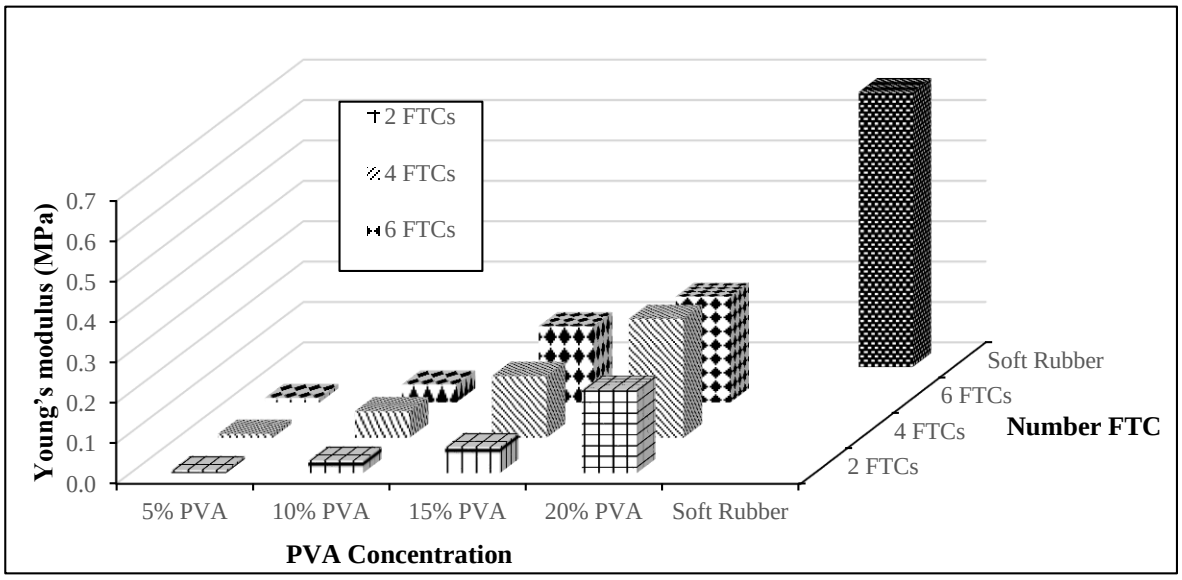

Figure 4.17. Young's moduli of all the PVA-C samples and soft rubber at 3% strain obtained from rigid indentation tests.

The results of ANOVA tests showed that Young's moduli of the samples were significantly different (P<0.001). A comparison between all two groups of the samples was also conducted in SigmaStat. The P values of these comparisons were less than 0.001 except for the comparison between 10% and 15% PVA, 2 FTCs (P=0.006) and 5% and 10% PVA 2FTCs (P=0.019). For 20% PVA samples with 4 and 6 FTCs, P value was higher than 0.05 and, therefore, the Young's moduli of these two samples were not significantly different.

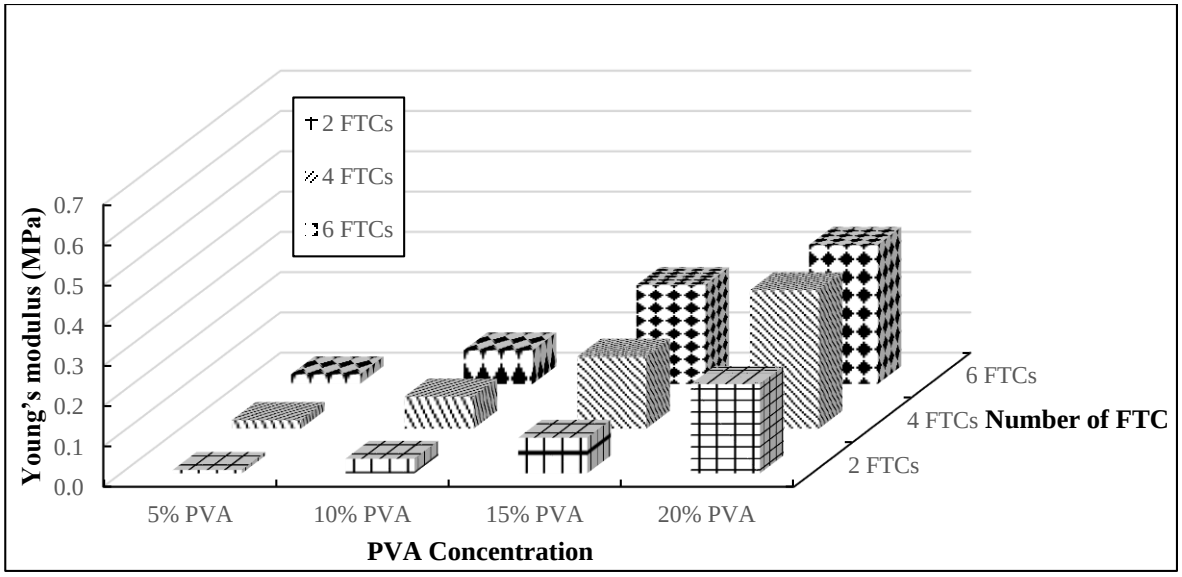

Figure 4.18. Young's moduli of all the PVA-C samples and soft rubber at 10% strain obtained from rigid indentation tests.

Figure 4.18 shows Young's moduli of the samples at the point where samples were indented to 10% of their initial height. The values of Young's moduli regarding to this graph are provided in table C.3 in Appendix C. A comparison between these values and those provided in Figure 4.17 shows that Young's moduli increases at higher strains. This is due to the nonlinear elasticity of the PVA-C (150).

4.3.2.2 Load Relaxation

As previously described in Section 3.3.2.1., different PVA-C samples with 6 FTC were indented to 10% of their initial height (D/H=0.1) and remained indented for 1000 seconds. The changes of the load over 1000 seconds are shown in Figure 4.19. The load is seen to decrease as the samples are held indented over the relaxation period. The result of the test on the soft rubber (39A) sample is also added to the graph for comparison.

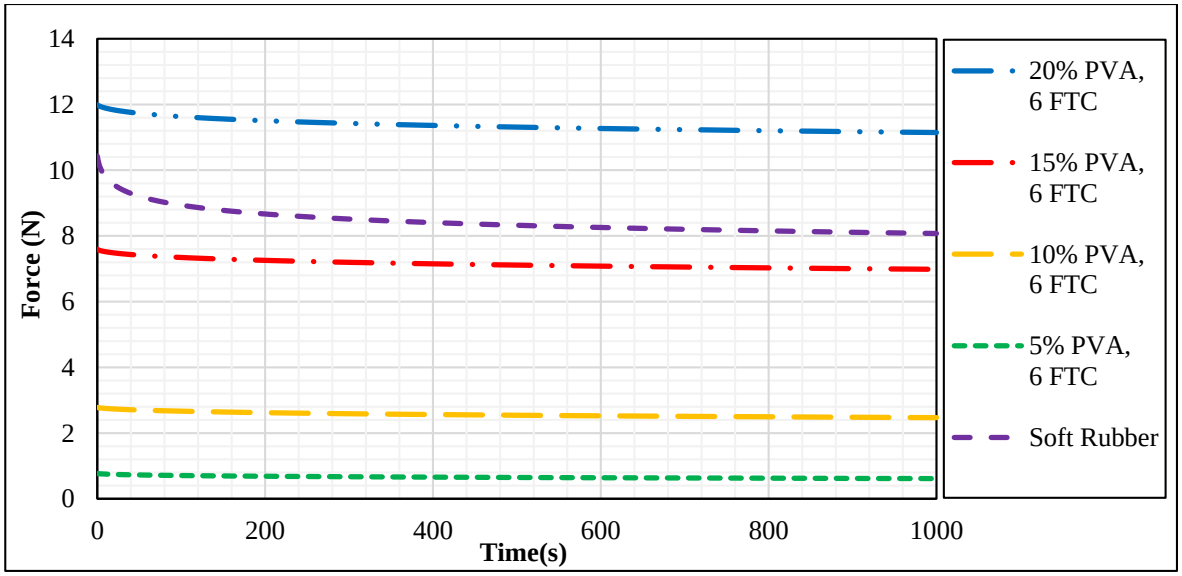

Figure 4.19. Force versus time for the samples held at a constant strain for 1000 s.

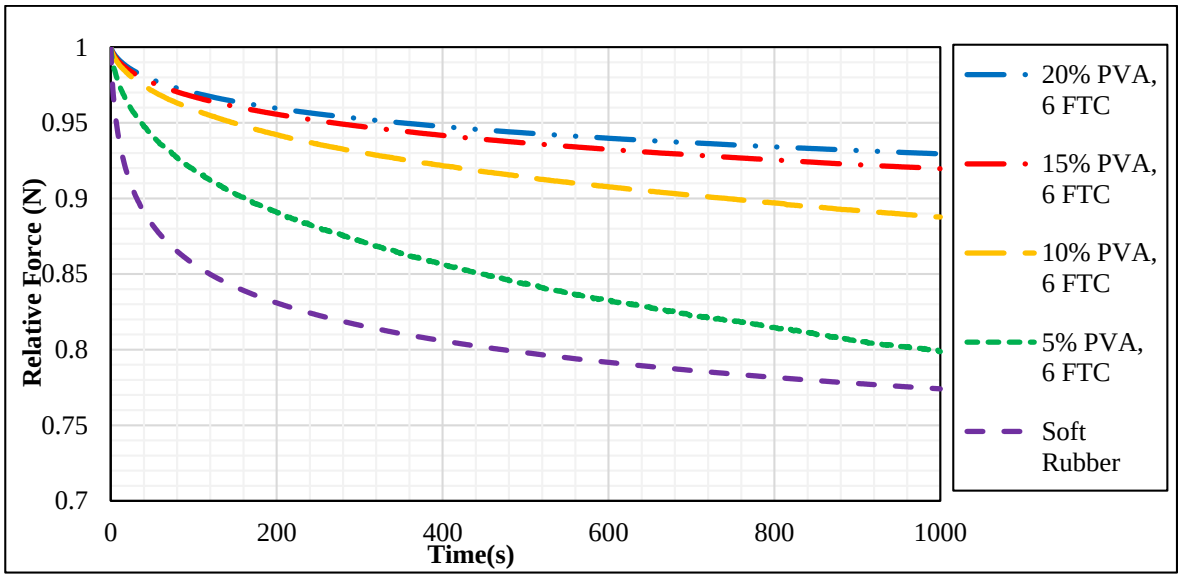

Figure 4.20. Relative force versus time for the samples held at a constant strain for 1000 s.

Figure 4.20 shows the relative load changes over the time of relaxation. It can be seen that for the PVA-C samples, the rate of load relaxation is higher in the softer samples. Samples with higher PVA concentration show less difference in force ratio after 1000 s. If we assume that the samples are behaving as poroelastic materials, this appears to show that the stiffer samples (15% PVA and 20% PVA) need more time to equilibrate the fluid pressures inside the samples.

Equation 3.15 was used to fit the relaxation curves for the different samples. As suggested by Lin and Hu (2006), this equation can be used to fit the initial parts of the relaxation curves (111). Therefore, the first 30 seconds (where the value of Z ranges between 0.005 and 0.05) of the relaxation data were used to do the fitting. Figures D.1 to D.5 in Appendix D show the load versus normalized time (t^*) from the experiment data along with the fitted curves for all of the samples. As shown in the graphs, the experimental data for the stiffer samples (15% PVA and 20% PVA) are fitted well to the equation 3.15, whereas the 5% PVA and 10% PVA samples do not fit the equation as well.

Table 4.4. Cooperative diffusion coefficient for different samples.

	5% PVA, 6FTC	**10% PVA, 6FTC**	**15% PVA, 6FTC**	**20% PVA, 6FTC**	**Soft Rubber**
$D_c \times 10^{-10}$ (m^2/s)	185.67±55.54	14.47±1.25	5.15±0.15	6.46±0.32	367.33±19.86

Table 4.4 shows the estimated values of the cooperative diffusion coefficient (D_c) for the different samples obtained from equation 3.15. As shown in the table, as the PVA concentration increases from 5%, to 10% and 15%, the values of D_c decrease. The D_c value is very similar for the 15% PVA and 20% PVA samples. Cooperative diffusion coefficient has also been measured in light scattering experiments (111). The results of our tests support those of Li et al. (1998). They used PVA-C as a drug delivery vehicle with bovine serum albumin (BSA) as the drug model to investigate the effect of PVA-C processing parameters and PVA concentration on the diffusion of BSA. It was found that increases in the PVA concentration decreases the rate of BSA release (151). The reason for this behavior lies in the microstructure of the PVA-C. The increase in the PVA concentration also increases the PVA volume in the polymer-rich regions of the cryogel. Therefore, the mobility of the particles decreases and results in a lower release rate and D_c. Hickey and Peppas (1995) also suggested that transport of fluids from PVA cryogel membranes is related to the mesh size and therefore, percentage crystallinity (152). Li et al. (1998) also found out that increasing number of freeze/thaw cycle decreases the release rate due to an increase in volume fraction of the crystalline regions (125). This can also been described by the microstructure of the cryogel. As the volume of the crystalline regions increase,

polymer chains in the amorphous region pack tighter and therefore, the network permeability and release rate decreases.

The relaxation behavior of the PVA-C, shown in Figures 4.19 and 4.20, is analogous to consolidation phenomena that occur in porous solids such as soil. Movement of the pore fluid takes finite time and therefore, the PVA-C behaves as an incompressible material immediately after indentation. This produces a pressure gradient in the PVA-C sample and the fluid flows until the pressure inside the sample goes to zero everywhere (83). This is the reason that the indentation force relaxes over time. These result agrees with what was previously found for elastic gels (83).

Wang et al. (2014) suggested that the relaxation of the load in PVA-C is controlled by the poroelastic and viscoelastic behaviors of the gel and depending on the time scale, both of these properties may cause time dependent responses (153). The size of the sample was shown to affect the force-displacement response in Section 4.2.1.4, which is a poroelastic response. There are characteristic times associated with both phenomena and these may be significant at different times during the test (77).

The difficulty in fitting the 5% and 10% PVA methods suggest that these formulations may have more dominant viscoelastic responses. It is feasible that a more appropriate viscoelastic model, such as that proposed by Park and Schapery (1999), involving a Prony series (154) would model the rubber and lower the PVA concentration materials more effectively.

4.4 Shear Wave Velocity Testing

Testing shear wave velocity in a sample provides the PVA-C behavior at very small strain range (about 10^{-5}). Reference shear modulus, the shear modulus at very small strains, is also estimated based on the shear wave velocity. A typical plot of the input and output signals obtained from the GDSBEAT software is shown in Figure 4.21. The arrival times in the frequency domain (cross-spectrum) and time domain (cross-correlation) were also estimated with the software and plotted in the graph.

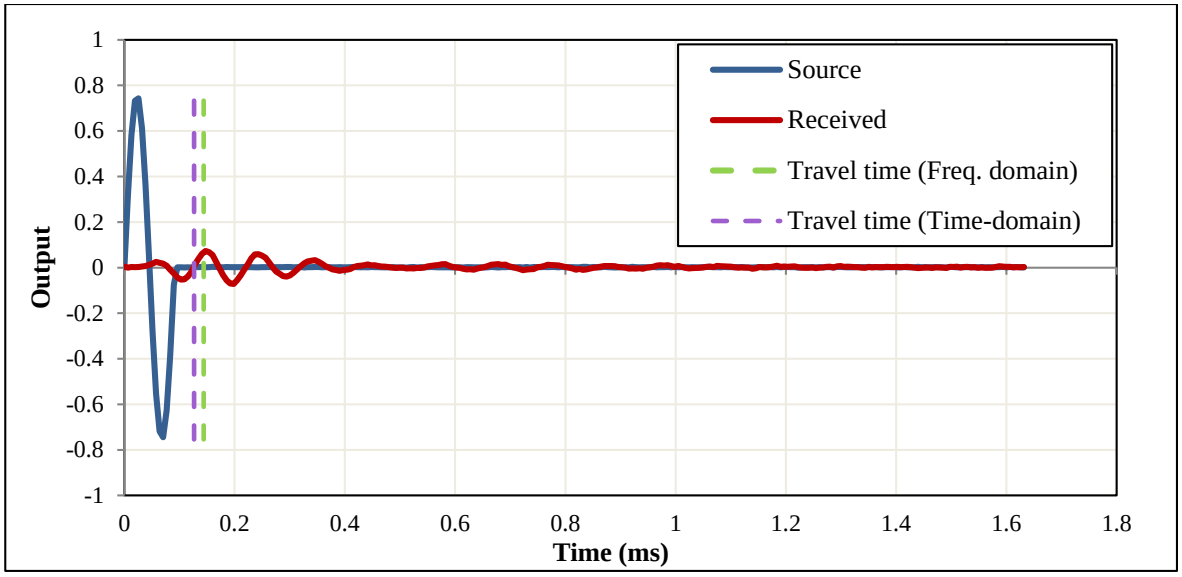

Figure 4.21. Typical source and received signals sent by the piezoelectric ring actuator. Estimated travel times are also shown in the graph.

There are several methods for estimating arrival time of the wave. Section 3.4.3.1 detailed these methods and their advantages and drawbacks. To compare the results of different methods on PVA-C samples, a signal with 8 kHz frequency was sent to a 15% PVA, 4 FTCs PVA-C sample under different axial loads. The arrival time of the output signal was estimated by four different methods. Visual picking, first major peak-to-peak, cross-correlation, and cross-spectrum were the methods used for analysis of these signals. Figure 4.22 indicates the arrival time of the wave estimated by the four methods at various pressures.

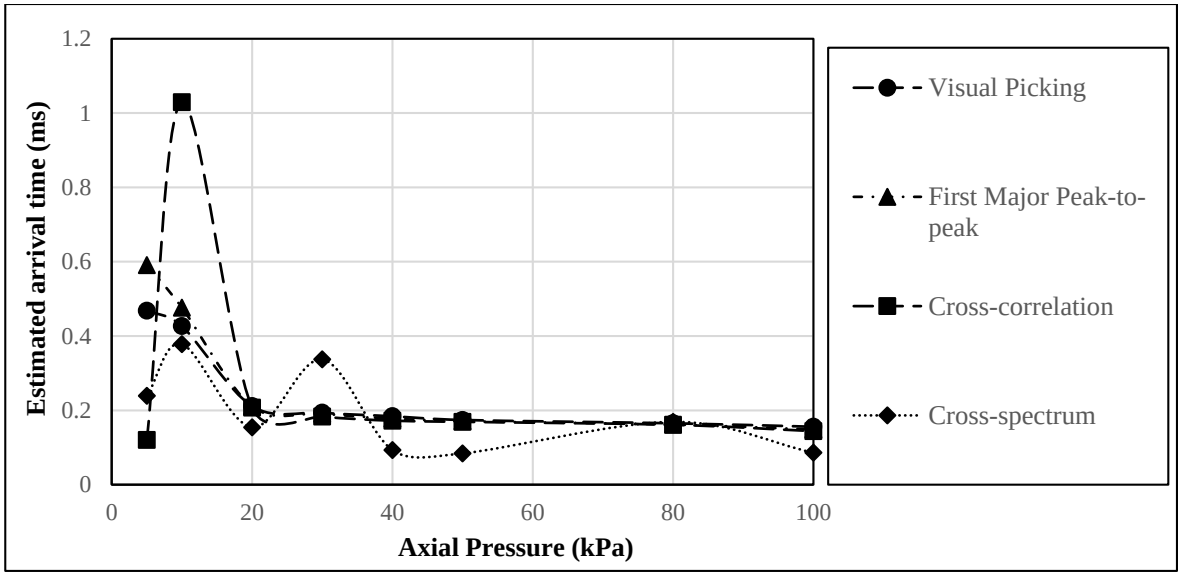

Figure 4.22. Estimated arrival time of the signal at different axial pressures, using four different methods.

As shown in Figure 4.22, the times estimated by the cross-spectrum method do not follow a similar trend at the different pressures. Theoretically, as the axial pressure on the sample increases, shear wave velocity should increase and therefore, the output signal reaches the receiver piezoelectric ring faster. Hence, the arrival time should have a negative relationship with the pressure. Cross-spectrum method does not have this inverse relationship at any pressure. The cross-correlation method has fluctuations at low pressures, but at pressures beyond 20 kPa the arrival times follow a more reasonable decreasing trend. The arrival times obtained from visual picking and first major peak-to-peak methods follow the expected trend at all pressures. To examine these methods, shear wave velocities obtained from these two methods (using equation 3.16) were compared to those obtained from the RC test (Section 4.5) performed on samples with similar properties. It should be noted that these approaches assume that the samples behave as elastic solids. The results of the first major peak-to-peak method showed better correlation with the RC test results. Therefore, the first major peak-to-peak method was used to estimate the arrival time of the wave in the remaining tests.

4.4.1 Effect of Wave Frequency

The results of a test conducted on a 15% PVA, 2FTC sample at different frequencies is shown in Figure 4.23. This test was conducted when 20 kPa pressure was applied to the sample. Error bars represent standard deviations in the results. As seen in the figure, an increase in the frequency of the input signal results in a higher shear wave velocity.

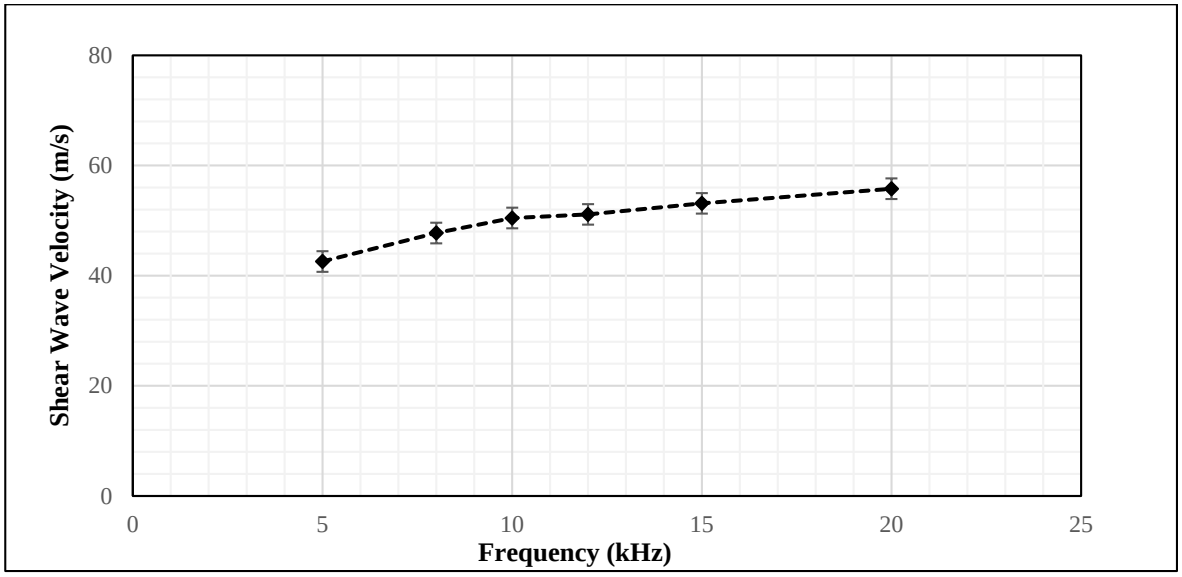

Figure 4.23. Shear wave velocity versus frequency for 15% PVA, 2FTC under 20 kPa pressure.

Using the values of the velocity of the shear wave (shown in Figure 4.23) and the relationship described in equation 3.17, reference shear modulus (G_0) of the samples was calculated. The values of G_0 for a 15% PVA, 2 FTC (at 20 kPa) sample over a range of frequencies is shown in Figure 4.24. The sample is under a constant pressure of 20 kPa. Although this has been referred to as *shear modulus,* care must be taken in the interpretation of the results if significant viscoelasticity is occurring. If this is the case, then this is a measure of the complex shear modulus, G^*.

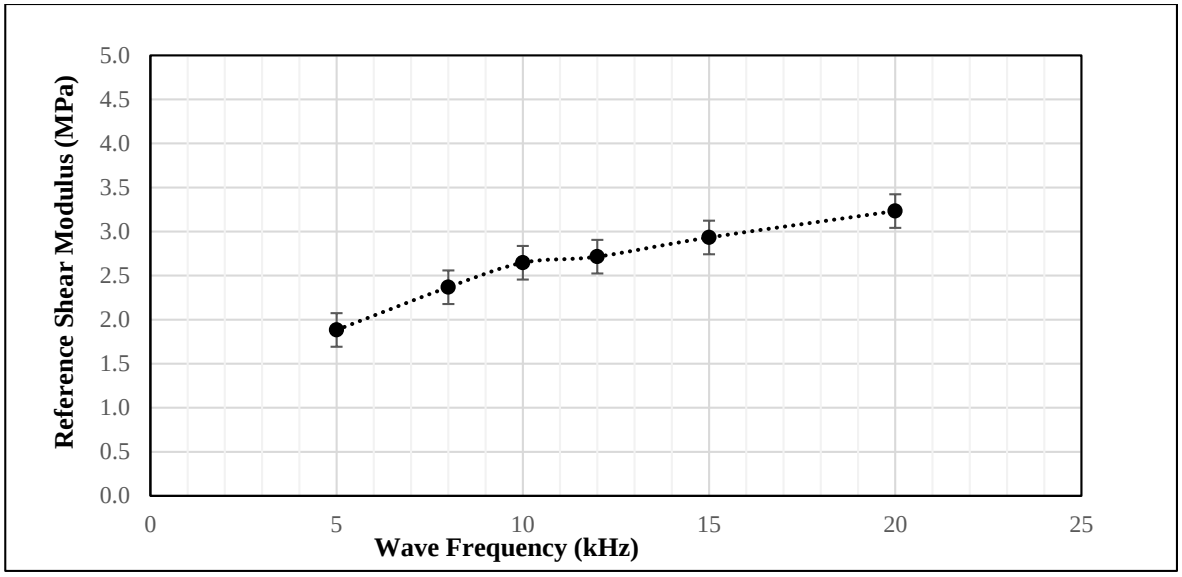

Figure 4.24. Reference shear modulus versus frequency for 15% PVA, 2FTC under 20 kPa pressure.

Reference shear modulus of the sample follows a similar trend to the shear wave velocity at different frequencies. As the frequency of the shear wave increases, the reference shear modulus of the sample goes up.

4.4.2 Effect of Axial Pressure

Figure 4.25 shows the shear wave velocity of 15% PVA, 2FTCs sample at different axial pressures while the frequency of the input signal is kept constant. The graph shows that the velocity of the wave increases when higher pressure is applied to the sample. This can be explained by the stiffness of the sample. Increasing the pressure leads to increases in the stiffness of the sample and therefore, the shear wave travels faster in the sample (18).

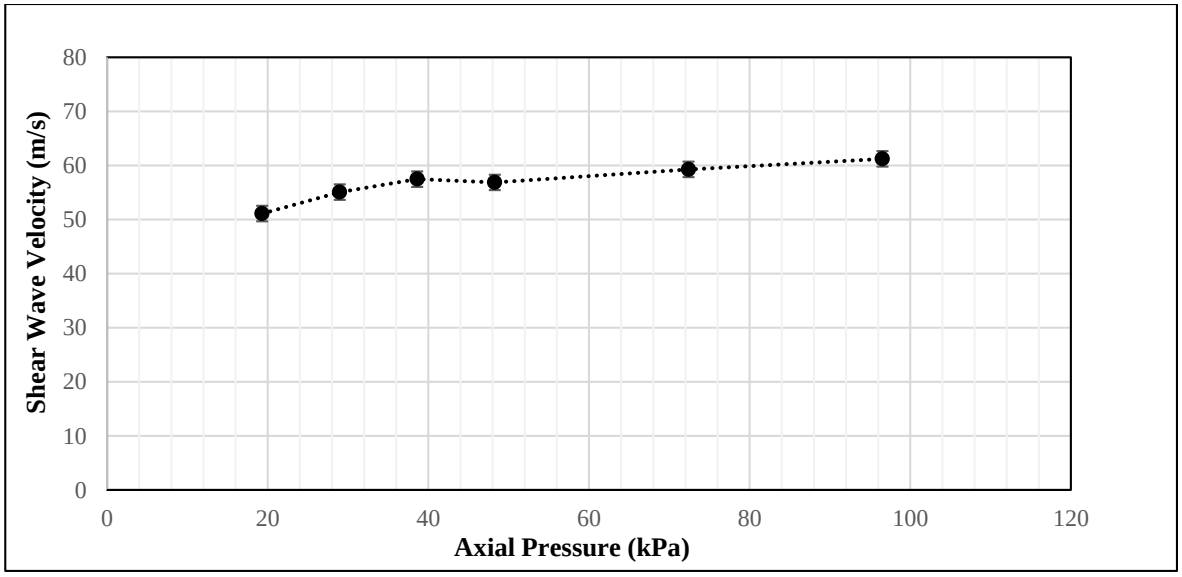

Figure 4.25. Shear wave velocity vs. axial pressure in 15% PVA, 2 FTCs sample, when frequency of the wave is 12 kHz.

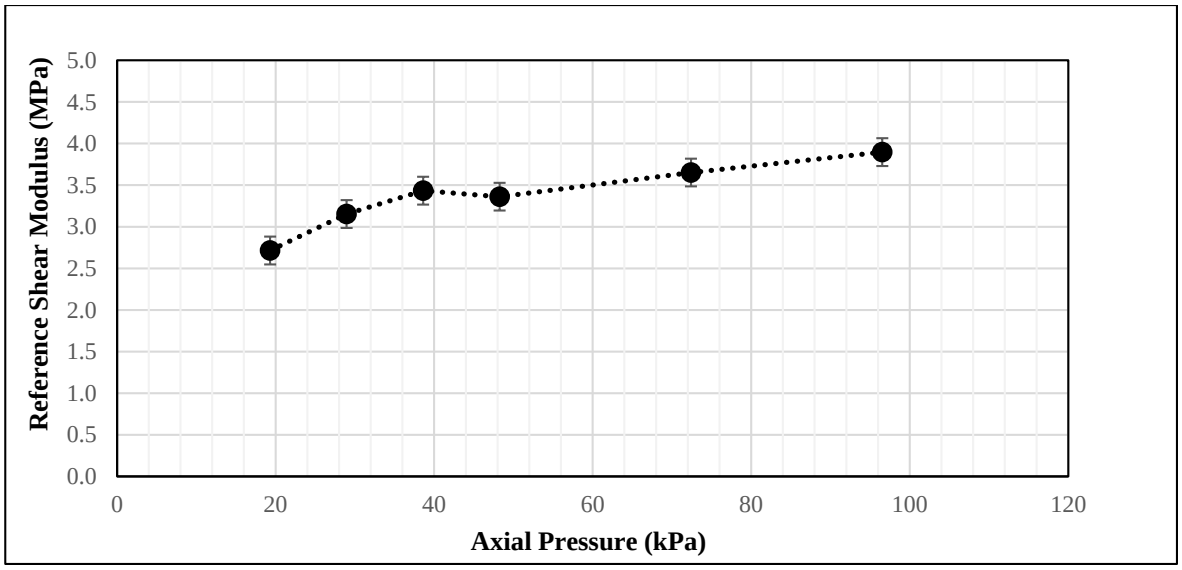

Figure 4.26. Reference shear modulus versus axial pressure in 15% PVA, 2 FTCs sample, when frequency of the wave is 12 kHz.

Figure 4.26 shows the effect of axial pressure on reference shear modulus of the 15% PVA, 2 FTC sample while the frequency of the input signal is 12 kHz. As shown in the figure, reference shear modulus and, therefore, the stiffness of the sample increases as the axial pressure applied to the sample rises. This also supports the fact that the increase in shear wave velocity depends on the material stiffness (18). Error bars in the graph show significant difference.

4.4.3 Effect of PVA Concentration

As previously discussed in Sections 4.2 and 4.3 for unconfined compression and rigid indentation testing, PVA concentration had a direct relationship with the stiffness of the samples. In this section, the effect of PVA concentration on shear wave velocity and reference shear modulus of the samples are investigated.

Figure 4.27 indicates shear wave velocities of samples with different PVA concentrations after 6 FTC over a range of axial pressures applied to the samples. Sinusoidal waves with the frequency of 12 kHz were sent to the samples.

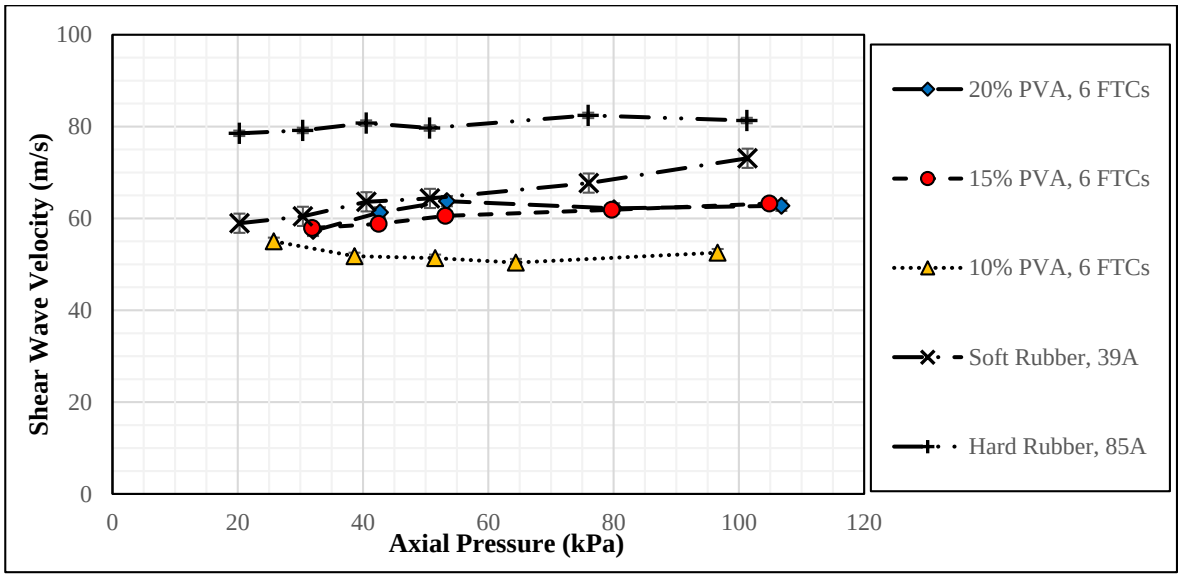

Figure 4.27. Comparison of shear wave velocity of different samples with 6 FTCs, along with the results of two rubber samples.

Reference shear modulus of the samples with different PVA concentrations and 6 FTCs were calculated by means of the velocities provided in Figure 4.27 and equation 3.17. Figure 4.28 shows reference shear modulus of samples with similar FTCs under various axial pressures.

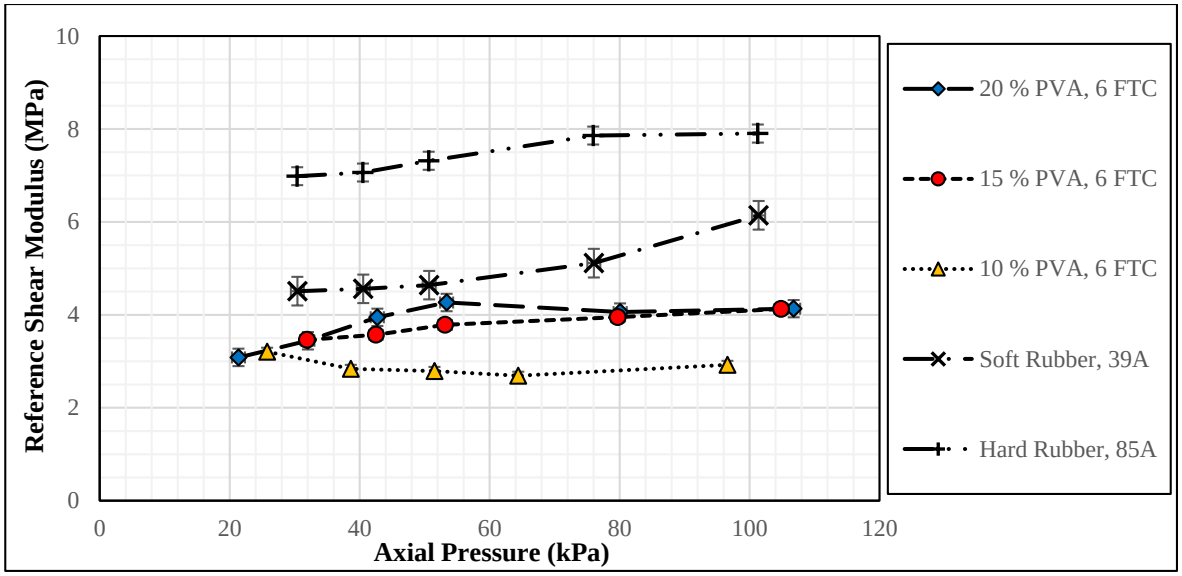

Figure 4.28. Comparison of reference shear modulus of different samples with 6 FTCs, at different axial pressures, along with the results of two rubber samples.

As shown in Figures 4.27 and 4.28, increasing PVA concentration from 10% PVA to 15% PVA increases shear wave velocity and reference shear modulus of the samples significantly. However, the difference between these values in 15% PVA and 20% PVA samples beyond 80 kPa axial pressure is not significant. There is a sudden rise in shear wave velocity as the pressure increases from 20 kPa to 30 kPa. Considering the constant trend observed in velocity and shear modulus of 10% PVA, 6 FTC sample, this issue may arise from the coupling of the piezoelectric ring actuator with the stiffer sample. As samples become stiffer, more load is needed to pressurize the sample and signal the quality is not as good as softer samples at low pressures (18). For soft (39A) and hard (85A) rubber samples, no output signal was observed at pressures below 20 kPa. Shear wave velocity and reference shear modulus in both rubber samples increases at higher pressures. As was previously seen in the results of the unconfined compression and indentation tests, the 20% PVA with 6 FTCs sample has similar stiffness to the soft rubber sample.

4.4.4 Effect of Freeze/thaw Cycles

It was shown in Sections 4.2 and 4.3 that the number of freeze/thaw cycles directly affects the Young's moduli of the samples. To investigate the effect of this parameter on the shear wave velocity and shear modulus of the samples, a series of tests were conducted on 15%

PVA samples with 2, 4, and 6 freeze/thaw cycles. The frequency of the input signal was 12 kHz. Figure 4.29 shows the changes of the data for PVA-C samples over a range of axial pressures. The results of the same test on the soft rubber (39A) and hard rubber (85A) samples are added to the graph for comparison.

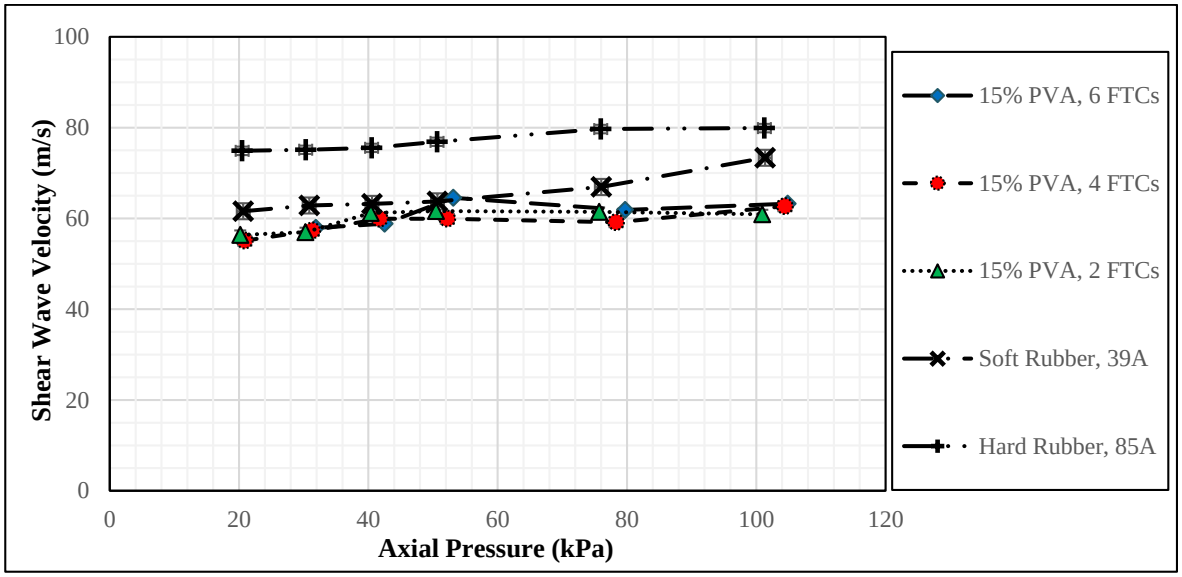

Figure 4.29. Comparison of shear wave velocity in 15% PVA samples with different numbers of FTC, along with the results of two rubber samples.

Figure 4.30 shows the effect of number of freeze/thaw cycles on reference shear modulus of the PVA-C samples at various axial pressures.

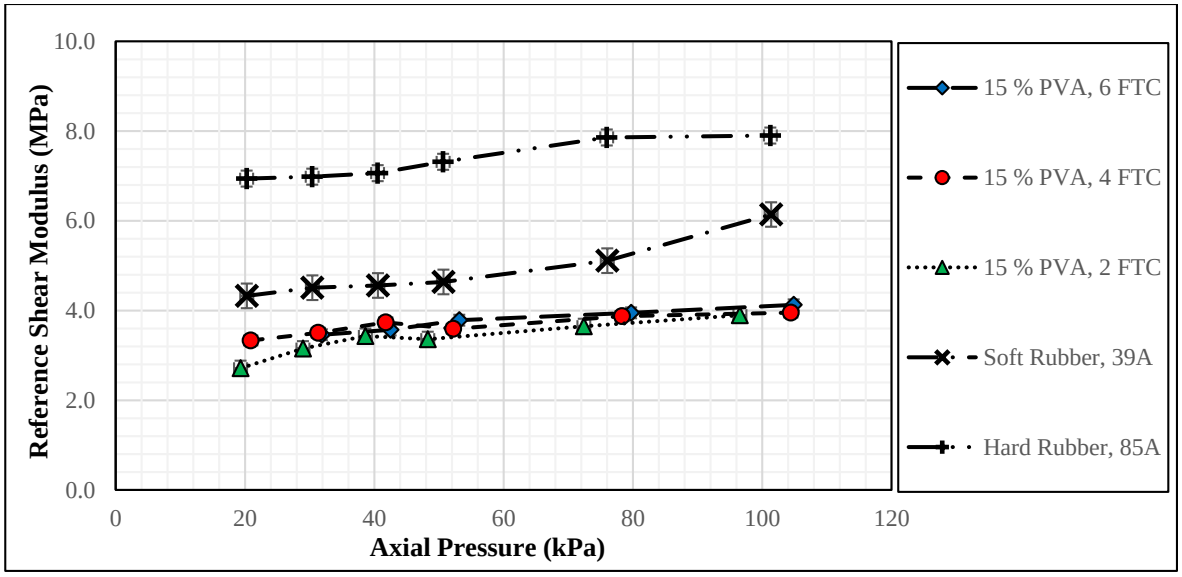

Figure 4.30. Comparison of reference shear modulus in 15% PVA samples with different numbers of FTC, along with the results of two rubber samples. Frequency of the waves are 12 kHz.

Shear wave velocity and reference shear modulus slightly increase as the number of freeze/thaw cycles of the samples increases. However, the difference between these values is not significant. As shown in Figures 4.29 and 4.30, shear wave velocity and reference shear modulus does not follow the expected trend and these values do not increase for higher number of FTCs at pressures lower than 30 kPa. As explained in previous section, this may be due to the coupling of the piezoelectric ring actuator and the samples.

4.5 Resonant Column Test

The resonant column test was conducted on the samples to investigate the mechanical properties for small strains. Pressure around the sample (cell pressure), PVA concentration and number of freeze/thaw cycles of the samples are the main factors affecting estimated shear wave velocity and shear modulus in this test. Effects of cell pressure and sample properties on stiffness of the samples were investigated. The results are provided in the following sections. Again it should be noted that the analysis of the resonant column assumes that standard material is elastic medium with negligible damping ratio (155). Damping ratio is defined for the RCA as the ratio between the system damping and the critical damping. Once the elastic shear modulus of the specimen is found, the material

damping ratio is evaluated independently. However, in a viscoelastic material the dynamic properties are not independent and have to be evaluated together (151). Analysis for viscoelastic interpretation of the RCA are known as non-resonance methods. This approach has not been adopted in this study.

4.5.1 Effect of Cell Pressure

Figures 4.31 and 4.32 illustrate the results of these tests on the softest (15% PVA, 2FTCs) and the stiffest (20% PVA, 6 FTCs) samples, respectively. To investigate the effect of cell pressure on shear moduli of the samples at small strains, the RC test was conducted at five different pressures of 5 kPa, 25 kPa, 50 kPa, 75 kPa, 100 kPa. However, the results are shown for only three different cell pressures of 5 kPa, 50 kPa, and 100 kPa, so that the trends are easier to follow. All of the data obtained from the RC test were fitted using equation 3.28. The fitted curves were included in Figures 4.31 and 4.32.

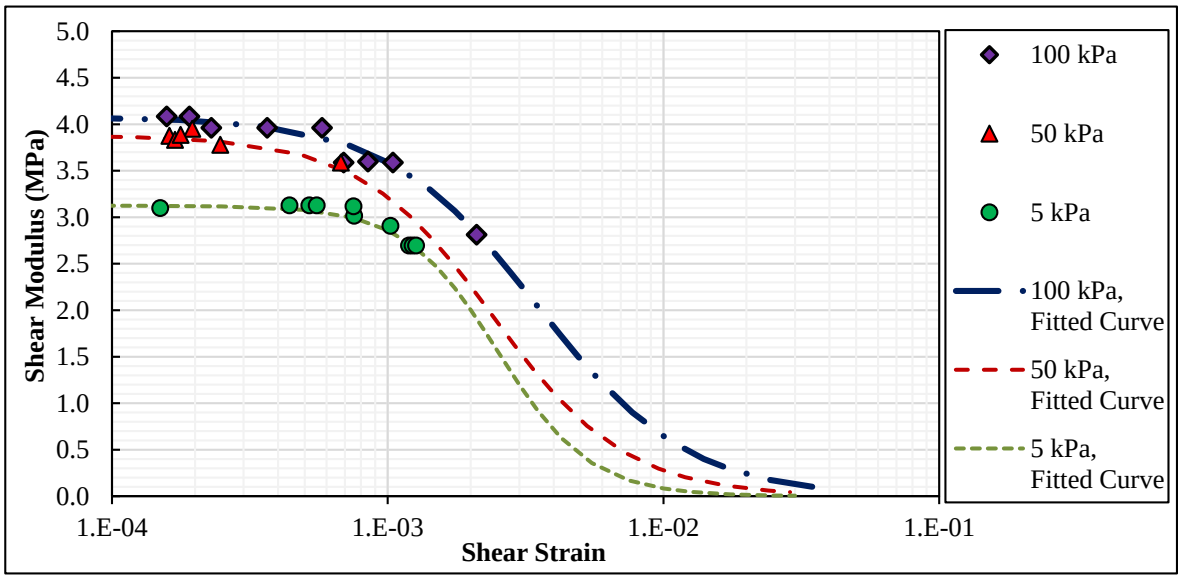

Figure 4.31. Effect of cell pressure on shear modulus of 20% PVA sample after 6FTCs.

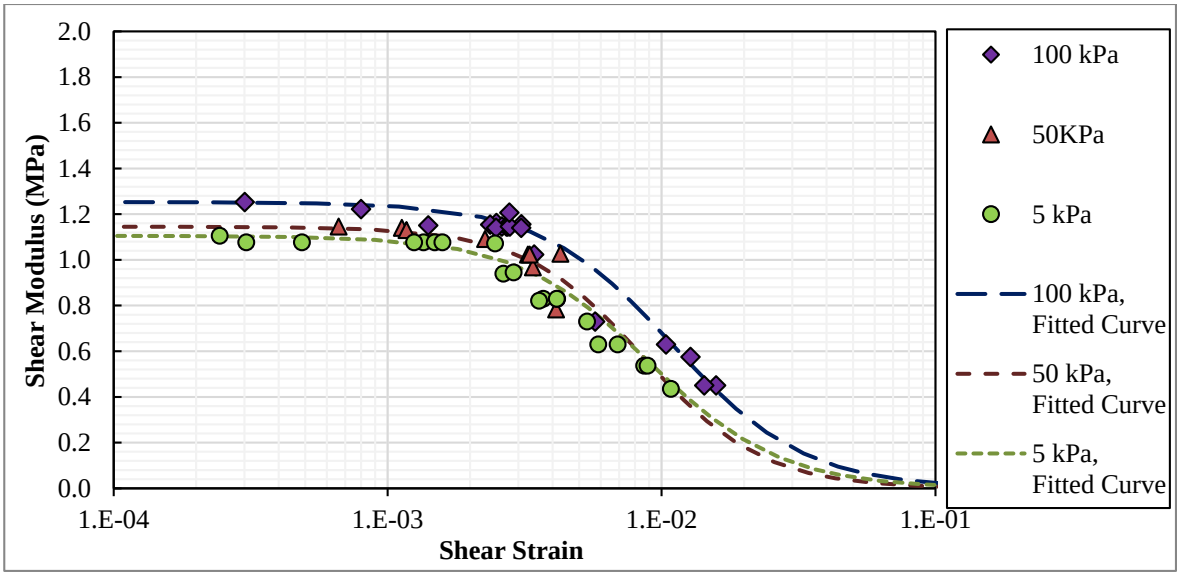

Figure 4.32. Effect of cell pressure on shear modulus of 15% PVA sample after 2FTCs.

As shown in the figures, shear modulus is directly affected by the cell pressure. As the pressure around the sample increases, shear modulus of the samples goes up. This trend is observed in both 15% PVA, 2FTCs and 20% PVA, 6 FTCs. However, the increase in shear modulus is higher in 20% PVA, 6FTCs where it increases from 3 MPa at 5 kPa cell pressure to 4 MPa at 100 kPa. Shear modulus of 15% PVA, 2 FTC starts from approximately 1.1 MPa and reaches 1.3 MPa at 100 kPa of cell pressure.

4.5.2 Effect of PVA Concentration and Freeze/thaw Cycles

Due to the limitations of the RCA, it was not possible to conduct this test on all of the PVA-C samples. The effect of number of freeze/thaw cycles was investigated by testing 20% PVA samples with 2, 4, and 6 FTCs. To investigate the changes in shear modulus caused by PVA concentrations, 15% PVA and 10% PVA samples with 4 and 6 FTCs were tested with the device. These tests were not successful because the size or stiffness of the samples did not meet the requirements for the RCA (See Section 3.3.4). Therefore, the results of tests on 15% PVA and 20% PVA samples with 2 FTCs were used to see the effect of polymer concentration on shear modulus at small strains.

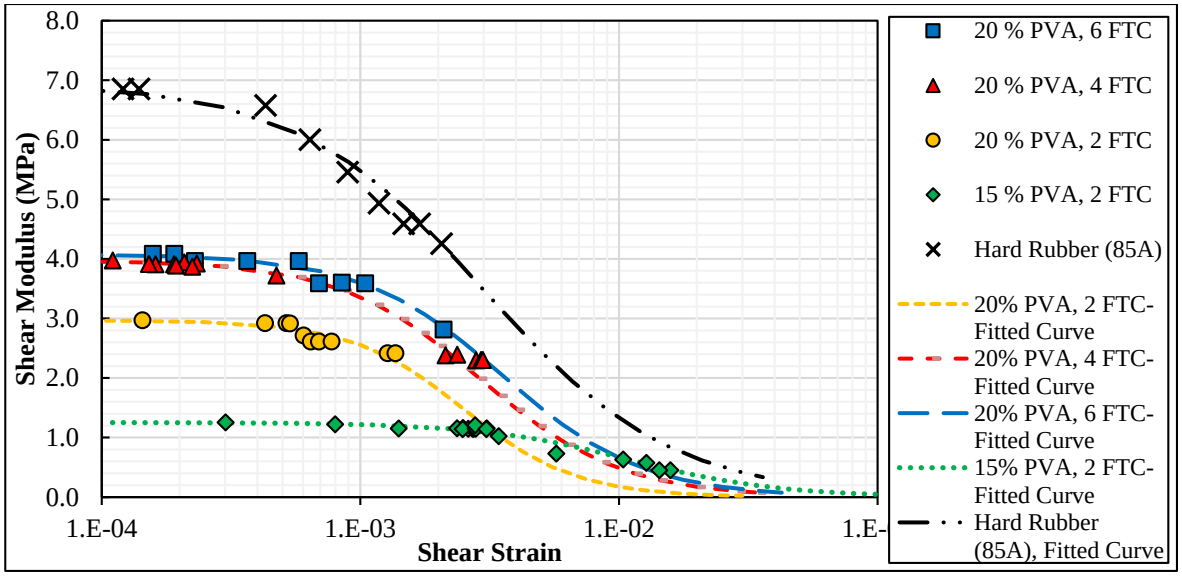

Figure 4.33. Effect of PVA concentration and number of FTCs on shear moduli of the samples, at 100 kPa cell pressure

Figure 4.33 shows the results of the tests on all of the samples at a cell pressure of 100 kPa. It is shown that the increase in the number of FTCs results in higher shear modulus. However, the difference between samples with 4 and 6 FTCs is less significant. This similarity between 20% PVA, 4 and 6 FTCs samples was previously observed in the results of the unconfined compression and rigid indentation tests (see Sections 4.2 and 4.3). As shown in the figure, the shear moduli of 20% PVA and 15% PVA samples with 2 FTCs are significantly different for the small strain range. Thus, for small strain ranges, higher stiffness is observed in samples with higher PVA concentrations. The results of the test on hard rubber (85A) are also shown in the figure for comparison.

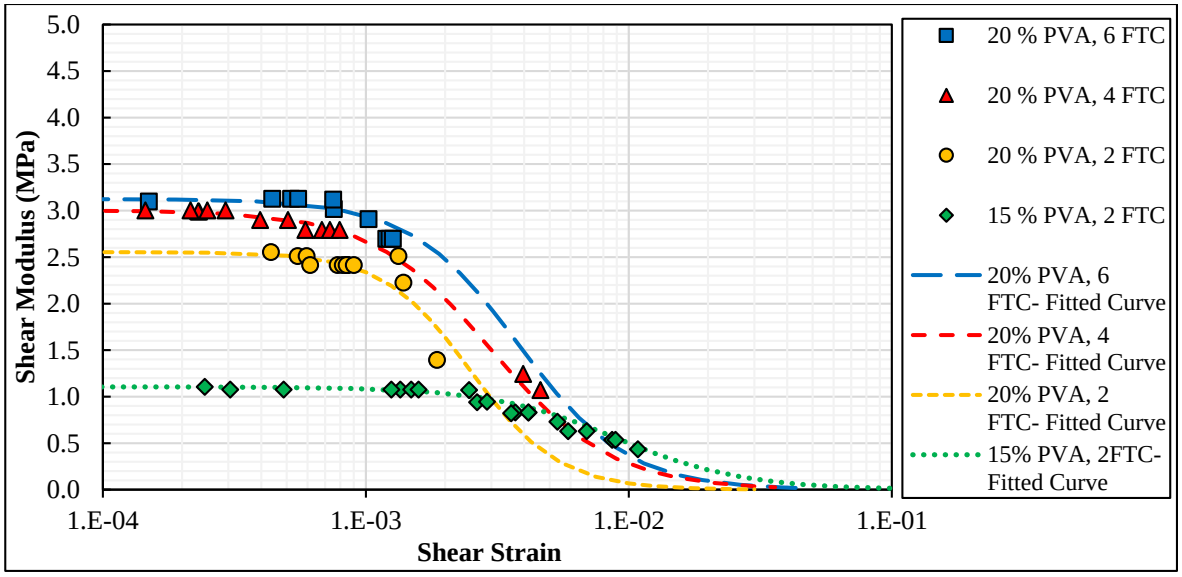

Figure 4.34. Effect of PVA concentration and number of FTCs on shear moduli of the samples, at 5 kPa cell pressure.

The results of the tests conducted at 5 kPa cell pressure are shown in Figure 4.34. Shear moduli of the different samples follow the similar trend to those subjected to the higher pressure. It is shown in both figures that at lower strains, there is no change in the shear modulus of a single sample. 20% PVA samples with 2, 4, and 6 FTCs show a constant value for shear modulus at strains below 0.001. The shear moduli start to decrease as the strain goes beyond this value. The shear moduli of 15% PVA, 2 FTC sample remains unchanged until an approximate strain of 0.0025 and start to decrease as the strain increases. It was not possible to obtain results for the hard rubber at this pressure, unfortunately.

Table 4.5. Curve fitting parameters for samples tested with the resonant column.

	100 kPa		**5 kPa**	
	c	γ_r	**c**	γ_r
15% PVA, 2 FTC	1.5	1.10E-02	1.8	9.00E-03
20% PVA, 2 FTC	2	2.50E-03	2.6	2.50E-03
20% PVA, 4 FTC	1.6	2.90E-03	1.9	3.00E-03
20% PVA, 6 FTC	1.6	3.55E-03	2.1	3.80E-03
Hard Rubber (85A)	1.6	3.50E-03	--	--

The results of resonant column tests were fitted using the equation 3.28. The curve fitting parameters for different samples at two different cell pressures of 100 kPa and 5 kPa, are

provided in Table 4.5. As it in the table, the value of the curve fitting parameter c increases as the PVA concentration changes from 15% to 20 % PVA. At 100 kPa, the value of c is similar for the 20% PVA samples with 4 and 6 FTCs and also the hard rubber sample. It is also see that c has a negative relationship with the cell pressure and decreases as the cell pressure changes from 5 kPa to 100 kPa for all of the samples. The value of the γ_r for the 15% PVA, 2 FTC sample is higher than the 20% PVA, 2 FTC sample in both cell pressures. In 20 % PVA samples, γ_r increases as the samples go through more freeze/thaw cycles. This trend is also seen for both the 5 kPa and 100 kPa pressures.

4.5.3 Damping test

A single damping ratio test was performed on a 20% PVA, 6 FTC sample and the results are shown in Figure 4.35. The damping ratio, $\acute{D}(\omega)$, is also determined as the ratio of the energy during a cycle of sinusoidal oscillation and the dissipated stored energy per unit volume. This is seen to vary between approximately 6 and 14% over a range strain of 0.0001 to 0.01.

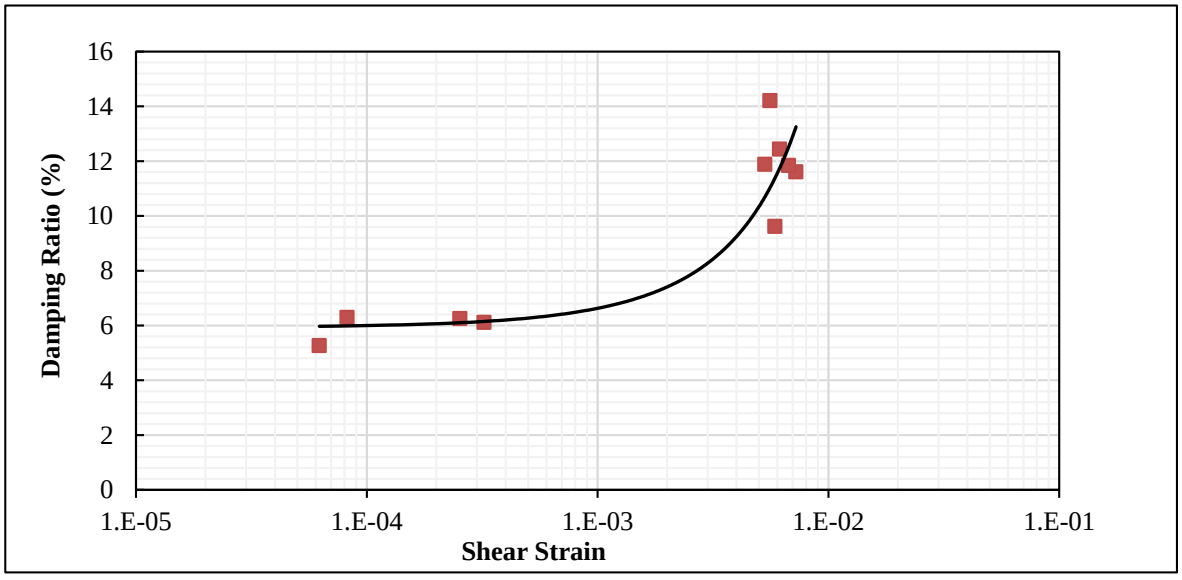

Figure 4.35. Percent damping ratio over shear strain for 20% PVA, 6 FTC sample.

The damping ratio can also be written as (156):

$$\acute{D}(\omega) = \frac{G''}{2G'} = \frac{1}{2}\tan\delta$$

Where G' is the storage modulus, G" the loss modulus and tanδ is the loss tangent. Loss and storage moduli of this sample are calculated and shown in Figures E.1 and E.2 in Appendix E. It is shown that by increasing shear strain from 0.0001 to 0.01, loss modulus decreases from approximately 0.46 to 0.34 MPa. Additionally, the storage modulus of the sample decreases from about 4.2 to 1 MPa over the same shear strain.

Previous estimates of tan δ for filled rubber (157) show values of 7% to 23% over the same strain range. Work by (158) on PVA-C with rheometry also found similar values for the loss tangent.

4.6 Comparison of the Testing Results

In this section, the results of all of the mechanical experiments are compared together and therefore, the behavior of PVA-C over different magnitudes of strain is provided. Stiffness values obtained in these experiments are compared with those of soft biological tissues. Additionally, the results of the tests conducted on this project are compared with other tests previously done on this material. Finally, interpretation of the observed results is provided to link structural and functional outcomes for these materials.

4.6.1 Mechanical Properties in Small to Medium Strains

Figures 4.36 to 4.38 show the change of shear modulus with increasing strain for 15% PVA, 2FTCs, 20% PVA- 6 FTCs, and the hard rubber sample (85A), respectively.

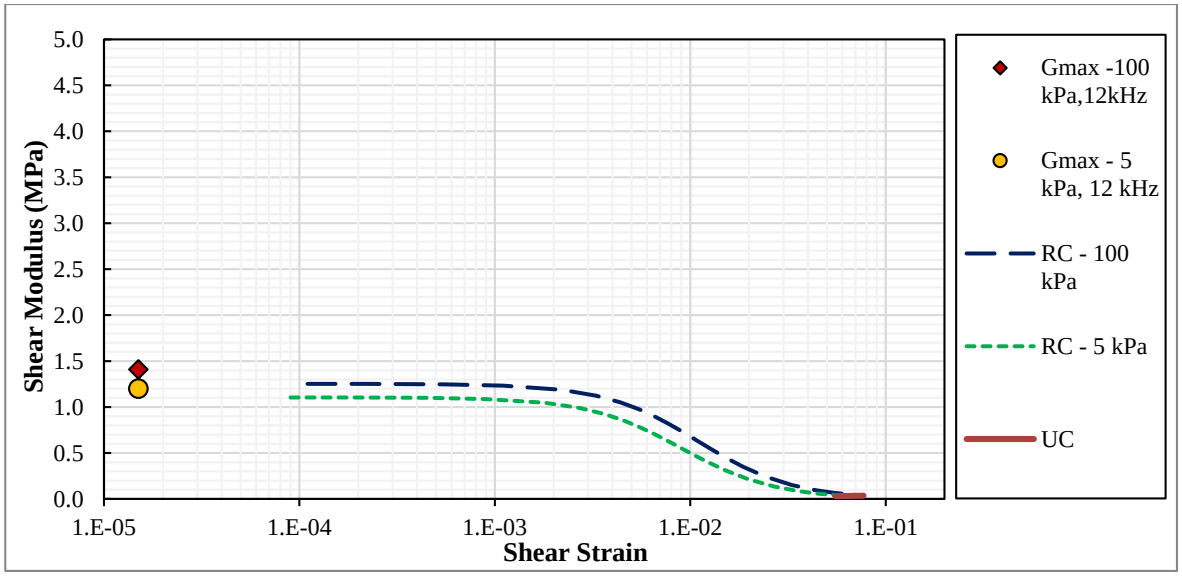

Figure 4.36. Shear modulus of 15% PVA, 2 FTC at different ranges of strain.

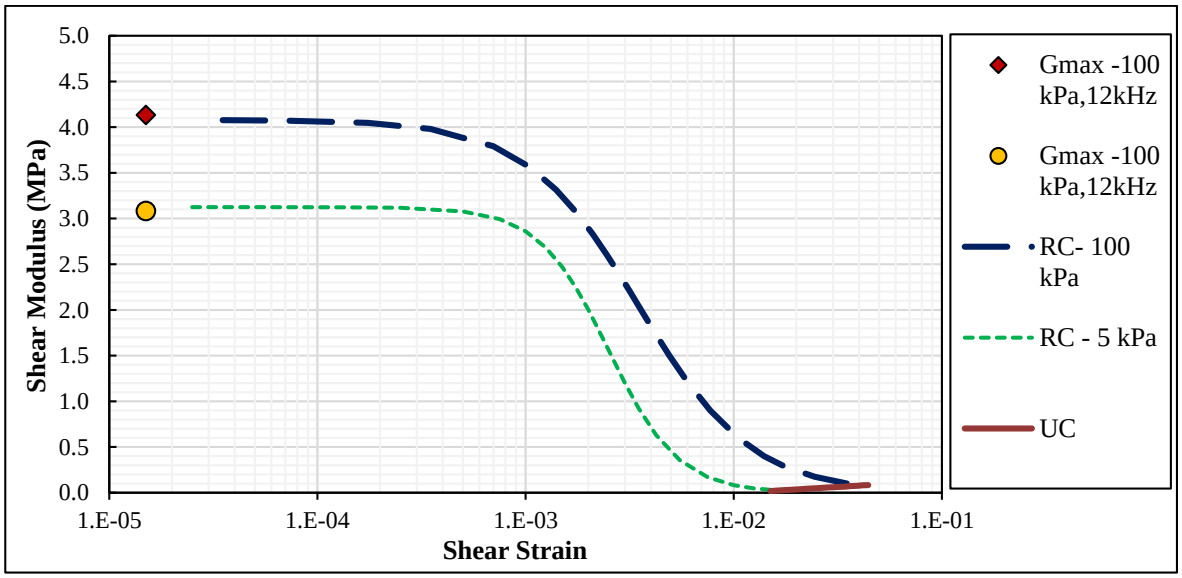

Figure 4.37. Shear modulus of 20% PVA, 6 FTC for different ranges of strain.

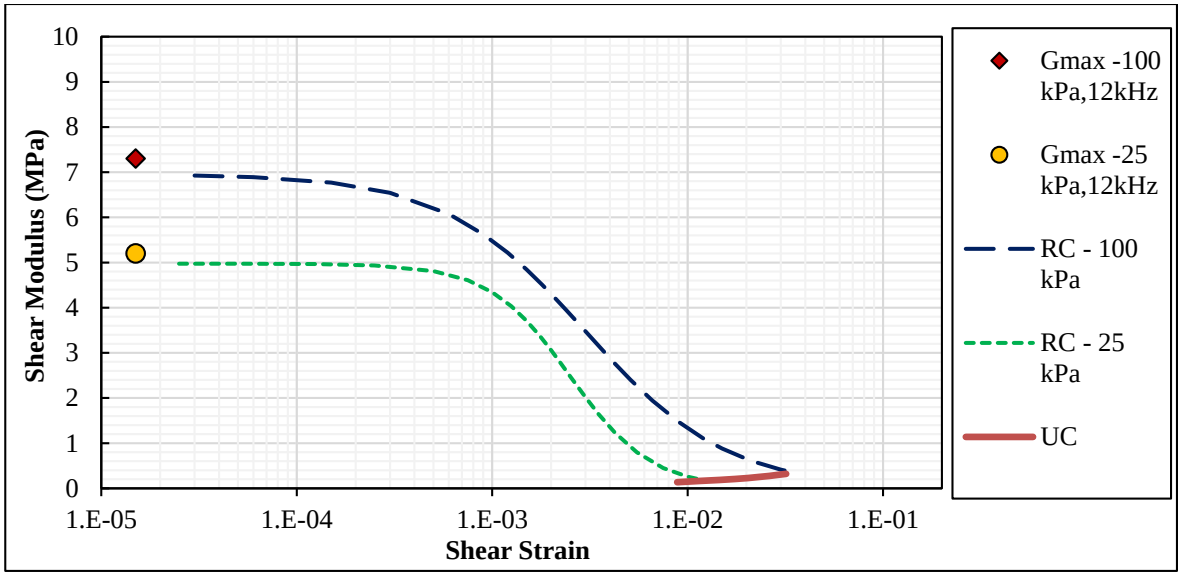

Figure 4.38. Shear modulus of hard rubber 85A for different ranges of strain.

As shown in the figures, for all of the samples, the reference shear moduli that were obtained from the piezoelectric ring actuator (see Section 4.4). The results of the resonant column test obtained for small strains show that shear moduli for PVA-C are essentially independent of strain at strains less than approximately 0.001 and start to decrease at shear strains beyond 0.001. The rubber sample shows that this threshold occurs between 0.001 and 0.01. Finally, the results of the UC test show that at strains near 0.01 (0.1 for 15% PVA, 2FTC), shear moduli begin to again increase as the strain increases. This result supports the reported results of Schubert and Harrison (2015) that showed at large strains (between 0.05 to 0.25), shear modulus has a direct relationship with strain (159). As mentioned before, some care needs to be taken interpreting these comparisons since the effect of viscoelasticity has not been counted for in the small-strain results. However, it does indicate that the shear modulus may be varying up to 2 orders of magnitude at medium strains.

4.6.2 Comparison with Soft Biological Tissues and PVA-C Literature

Table 4.6 shows a summary of the Young's moduli of various soft biological tissues along with estimates of the closest matching PVA-C formulation.

Table 4.6. Young's moduli of soft biological tissues along with suggested PVA-C for mimicking them

Body Organ/tissue	Young's modulus (MPa)	Suggested Formulation(s)
Abdominal Organs (44), (36), (45), (46)		
Bladder	0.128 [1]	10% 4FTC, 15% 2FTC
Gallbladder	0.015-0.05 [1]	15% 6FTC, 20% 4&6
Kidney (Human)	6.7-41.5 [1,2]	_
Liver	0.46-0.56 [1]	20% 6FTC
Large intestine	0.20- 0.33 [2]	15% 6FTC, 20% 4FTC
Small intestine	0.22- 0.60 [2]	20% 4&6FTC
Stomach	0.30-0.52 [1]	20% 6FTC
Spleen	0.18- 0.20 [1]	15% 4&6FTC
Brain (Human) (47), (48), (49)		
White matter	0.0017- 0.0054 [3]	_
Grey Matter	0.0016- 0.0031 [3]	_
Thalamus	0.0025- 0.0032 [3]	_
Midbrain	0.0025- 0.0033 [3]	_
Spinal cord	0.0002- 0.007 [3]	5% 1FTC
Breast (Human) (42), (50)	0.00325- 0.008 [1]	5% 2FTC
Cartilage (Human) (51), (52), (53)		
Articular Cartilage (Fibrous)	0.31- 0.80 [1]	20% 6FTC
Auricular Cartilage (Hyaline)	0.80- 2.78 [1]	_
Eye (38), (54), (55), (56)		
Cornea	0.159- 0.961 [1]	20% 6FTC
Sclera	0.269- 0.412 [1]	20% 6FTC
Intervertebral Disk (57)		
Anulus fibrosus	2.9- 6.6 [1]	_
Nucleus pulposus	0.00169- 0.00481 [1]	5% 1FTC
Muscle (RF) (58)	0.00922- 0.08531 [4]	15% 2FTC
Tendon (PT)	0.0556- 0.3318 [4]	15% 2FTC_ 20% 6FTC
Prostate (46), (59)	0.002- 0.0056 [1]	5% 2FTC
Skin (60)	0.001- 0.008 [1]	5% 2&4FTC
Thyroid (61)	0.009- 0.0114 [1]	5% 4&6FTC

[1]Compressive modulus
[2]Tensile modulus
[3]Dynamic modulus
[4]Shear wave ultrasound

The Young's moduli of those soft biological tissues that have been obtained from indentation, unconfined compression, tensile, dynamic, and shear wave velocity testing can be compared to the data from unconfined compression and rigid indentation of this study. As seen in the table, PVA-C samples produced for this study cannot mimic very soft tissues such as brain tissue. Therefore, PVA-C samples with lower concentrations of PVA and less freeze/thaw cycles are necessary to simulate these tissues.

Figure 4.39 shows stress-strain curves of cornea (38), articular cartilage (52), and gallbladder (36), along with the curves for the softest (5% PVA, 2FTC) and the stiffest (20% PVA, 6FTC) samples produced in this work.

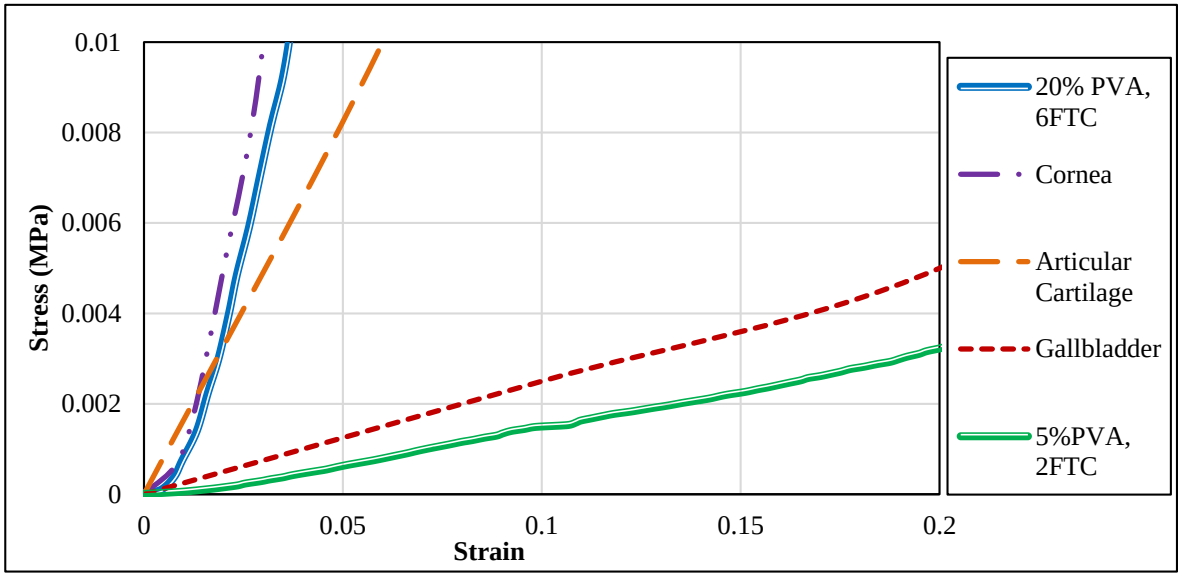

Figure 4.39. Stress-strain curves for soft biological tissues and the softest and stiffest PVA-C samples.

As shown in the figure, stress-strain curves for gallbladder and articular cartilage fall into a range of stiffness that can be simulated with the PVA-C samples in this work. The stress-strain curve for cornea initially is similar to that of the 20% PVA, 6FTC. Starting from about 0.02 strain, the curve for cornea becomes steeper than 20% PVA, 6FTC. This observation suggests that the cornea can be mimicked with 20% PVA, 6FTC at lower strains, but at higher strains stiffer material should be used to mimic this tissue. As previously suggested by Hudson et al. (2009), increasing the number of FTCs from 6 to 7 will not significantly increase the stiffness of the sample (131). Therefore, using some

additives such as dimethyl sulfoxide (DMSO) to the 20% PVA hydrogel will result in a stiffer PVA-C (99) that may be able to mimic the mechanical behavior of the cornea.

Table 4.7 provides the curve fitting parameters for the materials shown in Figure 4.38, fitted by equation 3.6. It can be seen that the value of the curve fitting parameter α for the gallbladder is lower than that of 5% PVA, 2FTC. Articular cartilage has the largest value of α, and the 20% PVA, 6 FTC sample and cornea have equal α parameters. The curve fitting parameter β increases as the stiffness of the samples increase.

Table 4.7. Curve fitting parameters for some of the PVA-C and soft biological tissues.

	α (MPa)	**β**	**r***
5% PVA, 2 FTC	0.966	0.014	0.984
Gallbladder	0.006	2.004	0.977
Articular Cartilage	0.076	2.091	0.993
20% PVA, 6 FTC	0.002	49.526	0.993
Cornea	0.001	72.895	1.000

*Correlation coefficient

The values of the Young's moduli obtained from different tests are compared with previous tests on similar material. The results of this comparison for the Young's moduli obtained from unconfined compression testing are provided in Table 4.8.

Table 4.8. Comparison of the Young's moduli from unconfined compression tests

	Zakeri	**Kazimierska (2015)**	**Wang and Campbell (2009)**	**Duboeuf et al. (2009)**	**Millon et al. (2009)**
Strain	3%	1-5%	5%	3-8%	45%
5% 6FTC	0.017	--	0.046	--	--
10% 2FTC	0.028	--	--	0.065	--
10% 4FTC	0.044	--	--	0.0144	--
10% 6 FTC	0.035	--	--	--	1.18
15% 6 FTC	0.235	--	0.357	--	--
20% 6FTC	0.236	0.241	--	--	--
Reference		(160)	(51)	(128)	(161)

As shown in the table, Young's moduli vary for the similar samples, but they have the same order of magnitude. The difference in the values is primarily due to the differences in the strain at which modulus has been calculated.

Fromageau et al. (2007) used different elastographic methods to assess the shear wave velocity in 10% PVA samples with different numbers of freeze/thaw cycles. They suggested that the increase in number of freeze/thaw cycles increases the shear wave velocity in the samples (12). This trend supports the results of the current work. As previously described in Section 4.4.4, the velocity of the shear wave propagation increased as the number of freeze/thaw cycles increased from 2 to 6. Fromageau et al. (2007) also suggested that the 10% PVA sample with 6 FTCs has a shear wave velocity of approximately 10 m/s when 3% Sigmacell was also added to the samples (12). In the current work, the shear wave velocity in the 10% PVA, 6 FTC samples were approximately 50 m/s at different axial pressures applied to the sample. The difference between the methods of shear wave velocity measurement may cause this difference in the results. In addition, elastography measurements are conducted when there is no load on the sample. However, axial pressures (up to 100 kPa) were applied on the sample in this work.

4.7 Discussion of the results

A number of researchers have found that cross-linked hydrogels are found to have higher stiffness moduli, dependent upon the water content, strain rate and strain magnitude (89). Freeze/thaw cycling is known to physically create cross-links in PVA-C hydrogels, joining the polymer chains together (106). Cycling to low temperatures leads to the formation of ice crystals and increases polymer concentrations in the unfrozen regions of the hydrogel inducing PVA crystallization. As the crystallites form these act as cross-linking sites. These thermal cycles enhance the density variations and expel water from the polymer rich regions. This leads to increases in the size and perfection of existing crystallites and creation of additional crystallites.

Increases in stiffness result from the increase in crystallinity and the increasing size of the largest gel aggregates. More cross-linking creates greater connectivity in the polymer

network and increased participation of polymer strands during deformation. Interestingly, the main structural changes occur in PVA-C up to 3 FTCs, but Young's moduli continue to increase up to 6-7 FTCs (106). This suggests that increasing stiffness is mainly due to improvements in the gel phase within the blobs (polymer nodes) within the gel aggregates (see Figure 2.3 and Section 2.5.2.2 for more discussion on this subject).

It can be assumed that PVA-C is therefore an isotropic polymer network where pairs of cross-linked points are connected by links of independent flexible or semi-flexible strands. In response to external stresses, the network nodes displace and strands stretch/compress, i.e. the network 'strains'. At modest strains the initial strain-stiffening in the network is dominated by entropic effects (106). Nonlinearity is found to be a result of different orientation/length strands participating in different ways; at higher strains more strands are mobilized and are found to orientate along the loading axis. The cross-link density and stiffness are found to have significant effects on the macroscopic stiffness of the hydrogel. Similar small-strain reductions in stiffness have been observed in filled rubber materials due to reversible network-aggregate disruptions (157) and these are found to become more significant between strains of 0.0001 to 0.001.

The time dependent phenomena observed during PVA testing Previously have been described as viscoelastic in nature. However, significant poroelasticity may also exist for PVA-C, where liquid phase flow occurs through the solid matrix during the loading. It is anticipated that less liquid phase exists for samples with high PVA concentration and more number of freeze/thaw cycles, with denser network meshes. This would increase poroelastic characteristics, which has been observed herein. Certainly the PVA-C seems to be displaying both viscoelastic and poroelastic traits; the dominant phenomenon may change for different PVA concentrations and number of freeze/thaw cycles. Further work needs to be conducted to better understand the results.

4.8 Summary

The results of the mechanical experiments conducted on the PVA-C samples were provided in this chapter. The results of unconfined compression and rigid indentation testing showed the mechanical behavior of the samples at large strains. Stress-strain curves, as well as,

Young's moduli of the samples were obtained from the unconfined compression test results. Additionally, the effect of strain rate and strain magnitude on the stiffness of the samples was discussed. Young's moduli of thick and thin samples were calculated using the rigid indentation test data with the Sneddon and Cao solutions. Shear wave velocity and reference shear modulus of the samples were estimated based on the data provided from the piezoelectric ring actuator. The results of resonant column tests provided information about the behavior of the PVA-C at small strains. At the end of this chapter, the results of all of the mechanical tests were compared together. It was shown that there are ranges of strains in which shear moduli stays constant. Once the strain exceeds a threshold of 0.001, the shear moduli appear to decrease. The shear moduli are found to increase again as the shear strain exceeds 0.05. The comparison of the Young's moduli obtained from unconfined compression tests to those of soft biological tissues show that the PVA-C samples are capable of mimicking different biological tissues. However, very soft and very stiff tissues cannot be simulated by the PVA-C samples produced in this study. Further studies of the poroelastic and viscoelastic behavior of the PVA-C would provide better understanding of the material and ultimately enable more appropriate use of PVA-C in medical applications.

Chapter 5 : Summary and Conclusion

5.1 Overview

For this study, PVA-C samples with 5%, 10%, 15%, and 20% PVA concentration and 2, 4, and 6 freeze/thaw cycles were made in different sizes. Nonlinear stress-strain curves for these materials at large strains were obtained from unconfined compression tests. The effect of strain rates on Young's moduli of the samples were also studied. Relaxation indentation tests were conducted to investigate the time dependent responses of the samples. Additionally, nonlinear behavior of the material at near zero strain was obtained by means of an innovative piezoelectric ring actuator. Finally, dynamic mechanical properties of PVA-C were investigated using the resonant column apparatus. The results of all of these tests were used to analyze the nonlinear stiffness properties of PVA-C.

5.2 Findings and Conclusions

Stress-strain curves were obtained from unconfined compression at moderate and high strains (higher than 1%). Slope of the curves and therefore, stiffness increased with increasing PVA concentration and number of freeze/thaw cycles. Stress-strain curves were also fitted to an equation previously used for fitting soft biological tissues experimental data. Curve fitting parameters were found to be affected by PVA concentration and the number of freeze/thaw cycles of the samples. To investigate the dependency of the mechanical properties on strain rate, stress-strain curves were obtained at two different strain rates of 0.17 s^{-1} and 0.017 s^{-1}. The results showed that the mechanical properties of PVA-C is also affected by the strain rate. However, the magnitude of the rate is important for observing significant differences occur between the stiffness of the samples at low and high strain rates. Additionally, the effect of sample thickness on the observed mechanical behavior was investigated by comparing the stress-strain curves of the mini-pucks and large cylindrical samples. Except for the softest sample (5% PVA, 2 FTC) the slope of the stress-strain curves was higher for the large cylindrical samples. This may be due to the boundary conditions, poroelasticity, and inhomogeneity of the large cylindrical samples.

For the indentation tests, Young's moduli of the large cylindrical samples were calculated based on Sneddon's theory for elastic half spaces. The effect of strain magnitude on the mechanical behavior of the materials was investigated by comparing the Young's moduli at 5% and 10% strain. It was shown that the PVA-C samples have higher Young's moduli at higher strain magnitudes and this is due to the nonlinear elasticity of the PVA-C. Indentation testing was also conducted on the mini-puck samples and the data were analyzed using Cao's solution for thin samples. Young's moduli of the samples at medium strain magnitude of 3% were found to vary between 0.0001 and 0.3 MPa. It was also shown for both thick and thin samples that increasing PVA concentration and number of freeze/thaw cycles will result in samples with higher stiffness. To investigate the time dependent properties of the PVA-C, force relaxation indentation tests were conducted on samples with different PVA concentrations. Force relaxation curves were fitted to a model proposed for poroelastic materials. The cooperative diffusion coefficient was found to decrease from 1.9×10^{-8} m^2/s for 5% PVA, 6FTC to 6.1×10^{-10} m^2/s for 20% PVA, 6FTC.

Data gathered from the piezoelectric ring actuator were used to measure the velocity of shear wave propagation in PVA-C samples. To investigate the effect of wave frequency, waves were sent to the samples at different frequencies of 5, 8, 10, 12, 15, and 20 kHz. The shear wave velocity of 15% PVA, 2 FTC samples were found to increase from approximately 40 m/s to 56 m/s at the corresponding frequencies. Consequently, reference shear modulus of samples increased from 2 MPa (at 5 kHz) to about 3.25 MPa (at 20 kHz). The effect of axial pressure was also investigated on the samples by applying axial pressures from 20 to 100 kPa to the samples. Shear wave velocity for 15% PVA, 2FTC samples increased from 56 to 61 m/s as the axial pressure increased (shear modulus varied between 2.7 and 4 MPa). The results of the tests conducted on samples with different PVA concentrations showed that samples with higher PVA concentrations have higher shear wave velocity and therefore, higher shear modulus. However, the difference between 15% PVA and 20% PVA with 6FTC was not significant. The shear wave velocity in these two samples at 100 kPa was about 65 m/s, which is higher than the 50 m/s for 10% PVA, 6FTC. Reference shear moduli for 10% PVA with 6 FTC at an axial pressure of 100 kPa was about 2.5 MPa and for 15% and 20% PVA samples with 6 FTCs was about 4 MPa. Comparison

of the shear wave velocities and reference shear moduli of samples with different numbers of freeze/thaw cycles showed that the shear wave velocity did not significantly increase in samples with more freeze/thaw cycles. In the 15% PVA sample, the velocity of the wave varied from 60 to 65 m/s as the number of FTCs increased from 2 to 4 (shear modulus changed from 3.75 to 4.25 MPa, correspondingly).

The results of the resonant column test showed that the shear modulus is not affected by shear strain when the shear strain in small strains (less than 0.001). The result of the resonant column test on the 20% PVA, 6 FTC sample at different cell pressures showed that as the cell pressure increases from 5 to 100 kPa, the small strain shear modulus increases from approximately 3 to 4 MPa. Similar trends were also observed in other samples. Therefore, an increase in the cell pressure directly affects the shear modulus of PVA-C samples. The results of the test conducted on the different samples at a constant cell pressure of 100 kPa, showed an increase in small-strain shear modulus of the 20% PVA samples as the number of freeze/thaw cycles increased from 2 to 4. Shear modulus is essentially the same for 20% PVA samples with 4 and 6 FTCs (about 4 MPa). Comparison between small-strain shear moduli of 15% PVA (1.2 MPa) and 20% PVA (3 MPa) samples with 2 FTCs show that the increase in PVA concentrations will result in higher small-strain shear moduli. The results of a single damping test on 20% PVA with 6 FTC showed that the damping ratio varies between 6 to 14% over the strain magnitudes of 10^{-4} to 10^{-2}, giving a loss tangent equal to 0.03 to 0.07.

Comparison of the results of all of the mechanical tests showed that the shear modulus is independent of shear strain when the strain is lower than 0.001. The shear modulus starts to decrease as the shear strain goes beyond 0.001. At strain magnitudes over 0.05, the shear modulus begins to increase again as the network of polymer chains begins to stretch significantly.

Interpretation of the observed shear modulus-strain responses can be based on information found in this study and in the literature. At very low strains, the shear moduli appear to be dependent purely on the structure of the developed polymer network (i.e. related to the PVA-C concentration and number of freeze/thaw cycles). Increases in pressure lead to

compression of this structure and increases in the shear moduli are observed. At small to intermediate strains, reductions in shear modulus are seen and therefore, the network must be degrading to some extent and reducing the cross-links between polymer chains. Presumably this is a very short term phenomena and is reversible. Similar structural degradation of filled rubber has been found previously (157) for the same strain ranges. At large strains, the classic non-linear stress-strain response begins to occur with the polymer network and chains being stretched with increasing strain; the shear moduli begin to increase significantly as the material begins to approach rupture.

Comparison of the observed mechanical behavior of PVA-C with biological tissues, suggests that it could be used as a tissue mimic for a wide range of tissues and organs. Further work is required for specific problems to fine-tune these properties and to investigate other mechanical properties of interest, e.g. Flow/diffusion properties, transparency, anisotropy, etc.

5.3 Future work

A number of modifications of the current testing can be proposed to improve the results. Increasing the homogeneity of the PVA-C samples will improve the variability of the mechanical tests. Implementing more efficient methods to remove air bubbles from the PVA hydrogel with higher PVA concentrations will improve the quality of the samples. To obtain this goal, two methods can be suggested. The first method is to design a setup which can maintain heat of the sample and vacuum at the same time. Therefore, bubbles will be removed before the hydrogel solidifies. The second method is adding non-toxic chemicals, such as dimethyl sulfoxide (DMSO) to PVA-S, which increases the stiffness of the cryogel without increase in concentration of the polymer. Homogeneity of the large cylindrical samples can also be increased by modifying the freeze/thaw cycle profile. Adding isotherms near the freezing and thawing points will improve the homogeneity of the samples. Better control of the moisture content of the samples during testing may also help reduce some of the scatter in the data.

To increase the signal quality and accuracy of the shear wave measurement technique, the mechanical contact between the sample and the piezoelectric plate should be improved. Increasing the roughness of the samples ends (e.g. by adding sand particles) or using base plates with pins or ridges would help this issue.

The RCA is usually designed to measure the properties of samples with higher stiffness than the PVA-C. Samples with more freeze/thaw cycles show higher stiffness, however, more shrinkage is observed as the number of freeze/thaw cycle increases which causes some problem in testing. Producing molds with more sizes by considering the poroelastic percent shrinkage/swelling of the samples or testing the samples in a submerged water bath will address the issues associated with shrinkage in the samples.

Other aspects of the testing that could be investigated to broaden the existing database and provide greater understanding could include: a) a wide range of strain rates, b) Further investigation of sample size effects, c) Further comparison of compression, shear and tensile properties, and d) a wide range of PVA-C concentrations and freeze/thaw cycles. The development of a rigorous analysis for the RCA using a viscoelastic model, would be extremely helpful and the development of interpretive methods to identity the storage and loss moduli would be very informative. Numerical and constitutive modeling of the results of the tests in this study using non-linear elastic (hyperelastic) and poro/viscoelastic models would help interpretation and understanding of the behavior. This could be linked to more investigation of the structural characteristics of the material. Finally, further enhancements of the PVA-C structure using anisotropic formation methods and chemical manipulation could be used to fine-tune the mechanical characteristics of this material for further medical applications.

References

1. Enderle JD, Bronzino JD. Introduction to biomedical engineering. Elsevier/Academic Press; 2012. 1252 p.

2. Roberts KE, Bell RL, Duffy AJ. Evolution of surgical skills training. World J Gastroenterol. 2006;12(20):3219–24.

3. Ziv A, Small SD, Wolpe PR. Patient safety and simulation-based medical education. Med Teach. 2000;22(5):489–95.

4. Matthews a, Hutnik C, Hill K, Newson T, Chan T, Campbell G. Indentation and needle insertion properties of the human eye. Eye. Nature Publishing Group; 2014;28(7):880–7.

5. Kneebone R. Simulation in surgical training: Educational issues and practical implications. Med Educ. 2003;37(3):267–277.

6. Sutherland LM, Middleton PF, Anthony A, Hamdorf J, Cregan P, Scott D, et al. Surgical Simulation. Ann Surg. 2006;243(3):291–300.

7. Śliwiński G, Schneider A, Schulz M, Wolf M, Fiolka A, Meyer M, et al. Physical Organ Phantoms for Training in Minimal Invasive Surgery (MIS). Springer Berlin Heidelberg. 2009: 120–3.

8. Sidhu RS, Park J, Brydges R, MacRae HM, Dubrowski A. Laboratory-based vascular anastomosis training: A randomized controlled trial evaluating the effects of bench model fidelity and level of training on skill acquisition. J Vasc Surg. 2007;45(2):343–9.

9. Ratner BD. Biomaterials science : an introduction to materials in medicine. Elsevier Academic Press; 2004. 851 p.

10. Surry KJM, Austin HJB, Fenster A, Peters TM. Poly(vinyl alcohol) cryogel phantoms for use in ultrasound and MR imaging. Phys Med Biol.

2004;49(24):5529–46.

11. Kharine A, Manohar S, Seeton R, Kolkman RGM, Bolt R a, Steenbergen W, et al. Poly(vinyl alcohol) gels for use as tissue phantoms in photoacoustic mammography. Phys Med Biol. 2003;48(3):357–70.

12. Fromageau J, Brusseau E, Vray D, Gimenez G, Delachartre P. Characterization of PVA cryogel for intravascular ultrasound elasticity imaging. IEEE Trans Ultrason Ferroelectr Freq Control. 2003;50(10):1318–24.

13. Chu KC, Rutt BK. Polyvinyl Alcohol Cryogel : An Ideal Phantom Material for MR Studies of Arterial Flow and Elasticity. (18):314–9.

14. Madsen EL, Hobson MA, Shi H, Varghese T, Frank GR. Tissue-mimicking agar/gelatin materials for use in heterogeneous elastography phantoms. Phys Med Biol. 2005;50(23):5597–618.

15. Hall TJ, Bilgen M, Insana MF, Krouskop TA. Phantom materials for elastography. IEEE Trans Ultrason Ferroelectr Freq Control. 1997;44(6):1355–65.

16. Madsen EL, Zagzebski J a, Banjavie R a, Jutila RE. Tissue mimicking materials for ultrasound phantoms. Med Phys. 2008;5(5):391–4.

17. Anseth KS, Bowman CN, Brannon-peppas L. REVIEW Mechanical properties of hydrogels and their experimental determination. Biomaterials. 1996;17(17):1647–57.

18. Fromageau J, Gennisson JL, Schmitt C, Maurice RL, Mongrain R, Cloutier G. Estimation of polyvinyl alcohol cryogel mechanical properties with four ultrasound elastography methods and comparison with gold standard testings. IEEE Trans Ultrason Ferroelectr Freq Control. 2007;54(3):498–508.

19. Stupp SI. iomaterials for Regenerative Medicine. MRS Bull. 2005;30(July):546–53.

20. Huebsch N, Mooney DJ. Inspiration and application in the evolution of biomaterials.

Nature. 2009;462(7272):426–32.

21. Chaikof EL, Matthew H, Kohn J, Mikos AG, Prestwich GD, Yip CM. Biomaterials and scaffolds in reparative medicine. Ann N Y Acad Sci. 2002;961:96–105.

22. Lysaght M, Webster TJ. Biomaterials for artificial organs. Woodhead Pub; 2011. 298 p.

23. Hoffman AS. Hydrogels for biomedical applications. Adv Drug Deliv Rev. 2002;54:3–12.

24. Wichterle O, Lím D. Hydrophilic Gels for Biological Use. Nature. 1960;185(4706):117–8.

25. Tanaka T. Phase transitions in gels and a single polymer. Polymer (Guildf). 1979;20(11):1404–12.

26. Hassan CM, Peppas NA. Structure and Applications of Poly(vinyl alcohol) Hydrogels Produced by Conventional Crosslinking or by Freezing/Thawing Methods. Biopolymers · PVA Hydrogels, Anionic Polymerisation Nanocomposites. Berlin, Heidelberg: Springer Berlin Heidelberg; p. 37–65.

27. Baker MI, Walsh SP, Schwartz Z, Boyan BD. A review of polyvinyl alcohol and its uses in cartilage and orthopedic applications. J Biomed Mater Res - Part B Appl Biomater. 2012;100 B(5):1451–7.

28. Lozinsky VI. Cryotropic gelation of poly (vinyl alcohol) solutions. Russ Chem Rev 1998;67(7).

29. Święszkowski W, Ku DN, Bersee HEN, Kurzydlowski KJ. An elastic material for cartilage replacement in an arthritic shoulder joint. Biomaterials. 2006;27(8):1534–41.

30. Kobayashi M, Toguchida J, Oka M. Preliminary study of polyvinyl alcohol-hydrogel (PVA-H) artificial meniscus. Biomaterials. 2003;24(4):639–47.

31. Kobayashi M, Chang YS, Oka M. A two year in vivo study of polyvinyl alcohol-hydrogel (PVA-H) artificial meniscus. Biomaterials. 2005;26(16):3243–8.

32. Jiang H, Campbell G, Boughner D, Wan WK, Quantz M. Design and manufacture of a polyvinyl alcohol (PVA) cryogel tri-leaflet heart valve prosthesis. Med Eng Phys. 2004;26(4):269–77.

33. Young TH, Yao NK, Chang RF, Chen LW. Evaluation of asymmetric poly(vinyl alcohol) membranes for use in artificial islets. Biomaterials. 1996;17(22):2139–45.

34. Burczak K, Gamian E, Kochman A. Long-term in vivo performance and biocompatibility of poly(vinyl alcohol) hydrogel macrocapsules for hybrid-type artificial pancreas. Biomaterials. 1996;17(24):2351–6.

35. Fung YC. Biomechanics: Mechanical Properties of Living Tissues. 2013. p 273.

36. Rosen J, Brown JD, De S, Sinanan M, Hannaford B. Biomechanical Properties of Abdominal Organs In Vivo and Postmortem Under Compression Loads. J Biomech Eng. 2008;130(2):21020.

37. Federico S, Gasser TC, Federico S, Gasser TC. Nonlinear elasticity of biological tissues with statistical fibre orientation Nonlinear elasticity of biological tissues with statistical fibre orientation. 2010;3(January):955–66.

38. Elsheikh A, Wang D, Brown M, Rama P, Campanelli M, Pye D. Assessment of corneal biomechanical properties and their variation with age. Curr Eye Res. 2007;32(1):11–9.

39. Galli M, Comley KSC, Shean T a. V, Oyen ML. Viscoelastic and poroelastic mechanical characterization of hydrated gels. J Mater Res. 2009;24(3):973–9.

40. Hu Y, Suo Z. Viscoelasticity and poroelasticity in elastomeric gels. Acta Mech Solida Sin. The Chinese Society of Theoretical and Applied Mechanics; 2012;25(5):441–58.

41. Özkaya N, Nordin M, Goldsheyder D Leger D. Mechanical Properties of Biological Tissues. Fundamentals of Biomechanics. 2012. p. 221–8.

42. Miller K. Diagnostics and Medical Technology Biomechanics of soft tissues. Med Sci Monit. 2000;6(1):158–67.

43. Jayasuriya AC, Ghosh S, Scheinbeim JI, Lubkin V, Bennett G, Kramer P. A study of piezoelectric and mechanical anisotropies of the human cornea. Biosens Bioelectron. 2003;18(4):381–7.

44. Rubod C, Brieu M, Cosson M, Rivaux G, Clay JC, De Landsheere L, et al. Biomechanical properties of human pelvic organs. Urology. Elsevier Inc.; 2012;79(4):968.e17-968.e22.

45. Snedeker JG, Niederer P, Schmidlin FR, Farshad M, Demetropoulos CK, Lee JB, et al. Strain-rate dependent material properties of the porcine and human kidney capsule. J Biomech. 2005;38(5):1011–21.

46. Samani A, Bishop J, Luginbuhl C, Plewes DB. Measuring the elastic modulus of ex vivo small tissue samples. Phys Med Biol. 2003;48(14):2183–98.

47. Schiavone P, Chassat F, Boudou T, Promayon E, Valdivia F, Payan Y. In vivo measurement of human brain elasticity using a light aspiration device. Med Image Anal. Elsevier B.V.; 2009;13(4):673–8.

48. van Dommelen JAW, van der Sande TPJ, Hrapko M, Peters GWM. Mechanical properties of brain tissue by indentation: Interregional variation. J Mech Behav Biomed Mater. Elsevier Ltd; 2010;3(2):158–66.

49. McKee CT, Last J, Russell P, Murphy CJ. Indentation Versus Tensile Measurements of Young's Modulus for Soft Biological Tissues. Tissue Eng Part B Rev. 2011;17.

50. Samani A, Zubovits J, Plewes D. Elastic moduli of normal and pathological human breast tissues: an inversion-technique-based investigation of 169 samples. Phys Med Biol. 2007;52:1565–76.

51. Spiller KL, Maher SA, Lowman AM. Hydrogels for the repair of articular cartilage defects. Tissue Eng Part B Rev. 2011;17(4):281–99.

52. Korhonen RK, Laasanen MS, Töyräs J, Rieppo J, Hirvonen J, Helminen HJ, et al. Comparison of the equilibrium response of articular cartilage in unconfined compression, confined compression and indentation. J Biomech. 2002;35(7):903–9.

53. Griffin MF, Premakumar Y, Seifalian AM, Szarko M, Butler PEM. Biomechanical Characterisation of the Human Auricular Cartilages; Implications for Tissue Engineering. Ann Biomed Eng. 2016;44(12):3460–7.

54. Elsheikh A, Wang D, Pye D. Determination of the modulus of elasticity of the human cornea. J Refract Surg. 2007;23(8):808–18.

55. Barraglioli JL, Kamm RD. Measurements of the Compressive Properties of Sclerol Tissue. Invest Ophthalmol Vis Sci. 1984;59–65.

56. Sjontoft E, Carsten E. In vivo determination of Young's modulus for the human cornea. Bull Math Biol. 1987;49(2):217–32.

57. Wang BH, Campbell G. Formulations of polyvinyl alcohol cryogel that mimic the biomechanical properties of soft tissues in the natural lumbar intervertebral disc. Spine (Phila Pa 1976). 2009;34(25):2745–53.

58. Kot BCW, Zhang ZJ, Lee AWC, Leung VYF, Fu SN. Elastic Modulus of Muscle and Tendon with Shear Wave Ultrasound Elastography: Variations with Different Technical Settings. PLoS One. 2012;7(8):2–7.

59. Hoyt K, Castaneda B, Zhang M, Nigwekar P, di Sant'Agnese PA, Joseph J V, et al. Tissue elasticity properties as biomarkers for prostate cancer. Cancer Biomark. 2008;4(4–5):213–25.

60. Pailler-Mattei C, Bec S, Zahouani H. In vivo measurements of the elastic mechanical properties of human skin by indentation tests. Med Eng Phys. 2008;30(5):599–606.

61. Lyshchik A, Higashi T, Asato R, Tanaka S, Ito J, Hiraoka M, et al. Elas tic Moduli Of Thy roid Tis sues Un der Com pres sion. 2005;110:101–10.

62. Holzapfel G. Biomechanics of Soft Tissues. Graz Univ Technol. 2000.

63. Mooney M. A Theory of Large Elastic Deformation. J Appl Phys. 1940 Sep;11(9):582–92.

64. Rivlin R. Large Elastic Deformations of Isotropic Materials . IV . Further Developments of the General Theory. Philos Trans R Soc London Ser A, Math Phys Sci. 1948;241(835):379–97.

65. Martins PALS, Natal Jorge RM, Ferreira AJM. A Comparative Study of Several Material Models for Prediction of Hyperelastic Properties: Application to Silicone-Rubber and Soft Tissues. Strain. 2006 Aug;42(3):135–47.

66. Ogden RW, Saccomandi G, Sgura I. Fitting hyperelastic models to experimental data. Comput Mech. 2004;34(6):484–502.

67. Holzapfel G. Nonlinear solid mechanics. Newyork: JOHN WILEY & SONS; 2000.

68. Ogden RW. Non-linear Elastic Deformations. Mineola, Newyork: Dover Publications; 1984.

69. Humphrey JD, Yin FCP. On Constitutive Relations and Finite Deformations of Passive Cardiac Tissue: I. A Pseudostrain-Energy Function. J Biomech Eng. American Society of Mechanical Engineers; 1987 Nov 1;109(4):298.

70. Ozkaya N, et al. Mechanical Properties of Biological Tissues. Fundamentals of Biomechanics: Equilibrium, Motion, and Deformation. Springer Sciences+ Business Media; 2012.

71. Roylance D. Engineering viscoelasticity. Massachusetts Institute of Technology. Cambridge, MA; 2001. p. 1–353.

72. M.A. M, K.k. C. Mechanical Behavior of Materials. CAMBRIDGE UNIVERSITY

PRESS. Cambridge, UK; 2009. 148-149 p.

73. Cowin SC. Bone poroelasticity. J Biomech. 1999;32(3):217–38.

74. Biot MA. General Theory of Three-Dimensional Consolidation. Repr from J Appliced Phys. 1941;12(2):155–64.

75. Cowin SC, Doty SB, editors. Tissue Mechanics. New York, NY: Springer New York; 2007.

76. Strange DGT, Fletcher TL, Tonsomboon K, Brawn H, Zhao X, Oyen ML. Separating poroviscoelastic deformation mechanisms in hydrogels. Appl Phys Lett. 2013;102(3):3–7.

77. Anirudh QW, Michelle CM, Zhao LOX. Separating viscoelasticity and poroelasticity of gels with different length and time scales. Acta Mech Sin. 2014;30(1):20–7.

78. Hu Y, Zhao X, Vlassak JJ, Suo Z. Using indentation to characterize the poroelasticity of gels. Appl Phys Lett. 2010;96(12):2009–11.

79. De Korte CL,Cespedes EI, van Der Steen AFW, Lancee CT. Intravascular elasticity imaging using ultrasound: feasibility studies in phantoms. Ultrasound Med Biol. 1997;23(5):735–46.

80. Gao L, Parker KJ, Alam SK, Lernel RM. Sonoelasticity imaging: theory and experimental verification. J Acoust Soc Am. 1995;97(6):3875–86.

81. Rosato D V. Polymer, Processes and properties of medical plastics: including markets and applications. Biocompatible polymers, metals, and composites. Lancaster, PA: ed. Technomic Publ.; 1983.

82. Nicolson PC, Vogt J. Soft contact lens polymers: An evolution. Biomaterials. 2001;22(24):3273–83.

83. Rodriguez F. Principles of polymer systems. 2nd ed. Newyork: McGraw Hill; 1982.

84. Billmeyer FW. Textbook of polymer science. Wiley; 1984. 578 p.

85. Bovey FA, Winslow FH. Macromolecules : an introduction to polymer science. Academic Press; 1979. 549 p.

86. Kariduraganavar MY, Kittur AA, Kamble RR. Polymer Synthesis and Processing. Natural and Synthetic Biomedical Polymers. Elsevier Inc.; 2014. p. 1:31.

87. Lozinsky VI, Plieva FM, Galaev IY, Mattiasson B. The potential of polymeric cryogels in bioseparation. Bioseparation. 2001;10(4–5):163–88.

88. Tanaka T. Gels. Structure and Dynamics of Biopolymers [Internet]. Dordrecht: Springer Netherlands; 1987. p. 237–57.

89. Stammen JA, Williams S, Ku DN, Guldberg RE. Mechanical properties of a novel PVA hydrogel in shear and unconfined compression. 2001;22:799–806.

90. Wan WK, Campbell G, Zhang ZF, Hui AJ, Boughner DR. Optimizing the tensile properties of polyvinyl alcohol hydrogel for the construction of a bioprosthetic heart valve stent. J Biomed Mater Res. 2002;63(6):854–61.

91. Lee KY, Mooney DJ. Hydrogels for tissue engineering. Chem Rev. 2001;101(7):1869–79.

92. Gulrez SKH, Al-Assaf S, Phillips GO. Hydrogels : Methods of Preparation, Characterisation and Applications. Prog Mol Environ Bioeng. 2003;51:117–50.

93. Lozinsky VI. Cryogels on the basis of natural and synthetic polymers: preparation, properties and application. Russ Chem Rev. 2002;71(6):489–511.

94. de Bruyn JR. private communication; 2017.

95. Jiang S, Liu S, Feng W. PVA hydrogel properties for biomedical application. J Mech Behav Biomed Mater. Elsevier Ltd; 2011;4(7):1228–33.

96. Burczak K, Gamian E, Kochman A. Long-term in vivo performance and

biocompatibility of poly(vinyl alcohol) hydrogel macrocapsules for hybrid-type artificial pancreas. Biomaterials. 1996;17(24):2351–6.

97. Finch CA. Polyvinyl alcohol : properties and applications. London New York: Wiley; 1973. 622 p.

98. Dai W., Barbari T. Hydrogel membranes with mesh size asymmetry based on the gradient crosslinking of poly(vinyl alcohol). J Memb Sci. 1999;156(1):67–79.

99. Okay O. Polymeric Cryogels. 2014. 333 p.

100. Wan WK, Campbell G, Zhang ZF, Hui a. J, Boughner DR. Optimizing the tensile properties of polyvinyl alcohol hydrogel for the construction of a bioprosthetic heart valve stent. J Biomed Mater Res. 2002;63:854–61.

101. Hassan CM, Peppas N. Structure and morphology of freeze/thawed PVA hydrogels. Macromolecules. 2000;33(7):2472–9.

102. Lozinsky VI, Vainerman ES, Domotenko L V., Mamtsis AM, Titova EF, Belavtseva EM, et al. Study of cryostructurization of polymer systems VII. Structure formation under freezing of poly(vinyl alcohol) aqueous solutions. Colloid Polym Sci. Steinkopff-Verlag; 1986 Jan;264(1):19–24.

103. Willcox PJ, Howie DW, Schmidt-rohr K, Hoagland DA, Gido SP, Pudjijanto S, et al. Microstructure of Poly(vinyl alcohol) Hydrogels Produced by Freeze/Thaw Cycling. J Polym Sci Part B Polym Phys. 1999;37:3438–54.

104. Talmon Y. Transmission Electron Microscopy of Complex Fluids: The State of the Art. Berichte der Bunsengesellschaft für Phys Chemie. 1996;100(3):364–72.

105. Pynn R. Neutron Scattering_ A Non-destructive Microscope for Seeing Inside Matter. Neutron Application in Earth, Energy and Environmental Sciences, Neutron Scattering Applications and Techniques. 2009. p. 1–29.

106. Hudson SD, Hutter JL, Nieh MP, Pencer J, Millon LE, Wan W. Characterization of

anisotropic poly(vinyl alcohol) hydrogel by small and ultra-small angle neutron scattering. J Chem Phys. 2009;130(3).

107. Millon LE, Nieh MP, Hutter JL, Wan K. SANS characterization of an anisotropic poly(vinyl alcohol) hydrogel with vascular applications. Macromolecules. 2007;40(10):3655–62.

108. Hudson S. Structure and Strength: Anisotropic Polyvinyl Alcohol Hydrogels and Spider Mite Silk Fibres Graduate Program in Physics. The University of Western Ontario; 2011.

109. Wan W, Bannerman AD, Yang L, Mak H. Poly(Vinyl Alcohol) Cryogels for Biomedical Applications. Polymeric cryogels Advances in Polymer Science. Sweitzerland: Springer International Publishing; 2014. p. iii–iv.

110. Millon LE, Mohammadi H, Wan WK. Anisotropic Polyvinyl Alcohol Hydrogel for Cardiovascular Applications. J Biomed Mater Res B Appl Biomater. 2006;79B(2):305–11.

111. Lin YY, Hu BW. Load relaxation of a flat rigid circular indenter on a gel half space. J Non Cryst Solids. 2006;352(38–39):4034–40.

112. Shibayama M, Uesaka M, Shiwa Y. Swelling/shrinking kinetics of chemically cross-linked poly(vinyl alcohol) gels in the presence of borate ions. J Chem Phys. 1996;105(10):4350.

113. Minton J a., Iravani A, Azizeh-Mitra Yousefi. Improving the homogeneity of tissue-mimicking cryogel phantoms for medical imaging. Med Phys. 2012;39(2012):6796–807.

114. Brignoli EGM, Gotti M, Stokoe KH. Measurement of shear waves in laboratory specimens by means of piezoelectric transducers. Geotech Test J. 1996;19(4):384–97.

115. Campbell G. Standard Operating Procedures 001. 2014.

116. Cao Y, Ma D, Raabe D. The use of flat punch indentation to determine the viscoelastic properties in the time and frequency domains of a soft layer bonded to a rigid substrate. Acta Biomater. Acta Materialia Inc.; 2009;5(1):240–8.

117. Elkut F, Bradley GR, Krywonos J, Fenwick J, Ren XJ. Numerical study of the mechanics of indentation bending tests of thin membranes and inverse materials parameters prediction. Comput Mater Sci. Elsevier B.V.; 2012;52(1):123–7.

118. Engel AJ, Bashford GR. Enabling real-time ultrasound imaging of soft tissue mechanical properties by simplification of the shear wave motion equation. Proc Annu Int Conf IEEE Eng Med Biol Soc EMBS. 2015;2015–Novem:3831–4.

119. Gennisson J-L, Catheline S, Chaffaï S, Fink M. Transient elastography in anisotropic medium: application to the measurement of slow and fast shear wave speeds in muscles. J Acoust Soc Am. 2003;114(1):536–41.

120. Catheline S, Wu F, Fink M. A solution to diffraction biases in sonoelasticity: the acoustic impulse technique. J Acoust Soc Am. 1999;105(5):2941–50.

121. Karray M, Romdhan M Ben, Hussien MN, Éthier Y. Measuring shear wave velocity of granular material using the Piezoelectric Ring Actuator Technique (P-RAT). Can Geotech J. 2015;1317(January):1302–17.

122. Ahmad S. Piezoelectric Device for Measuring Shear Wave Velocity of Soils and Evaluation of Low and High Strain Shear Modulus. Electron Thesis Diss Repos. 2016;

123. Campbell G. private communication; 2015.

124. Drnevich V, Hardin B, Shippy D. Modulus and damping of soils by the resonant-column method. Dyn Geotech Test. 1978.

125. Liu H, Liu D, Bo J. Effects of Maximum Shear Modulus on Soil Dynamic Properties and Seismic Response of Soil Layer. JettyEcnPurdueEdu. 2008;541–54.

126. Askeland DR, Haddleton F, Green P, Robertson H. The science and engineering of materials. Stanley Thornes; 1998. 854 p.

127. Vable M. Mechanical Properties of Materials. Springer. 2012;190:645.

128. Duboeuf F, Basarab A, Liebgott H, Brusseau E, Delachartre P, Vray D. Investigation of PVA cryogel Young's modulus stability with time, controlled by a simple reliable technique. Med Phys. 2009;36(2):656–61.

129. Cloyd JM, Malhotra NR, Weng L, Chen W, Mauck RL, Elliott DM. Material properties in unconfined compression of human nucleus pulposus, injectable hyaluronic acid-based hydrogels and tissue engineering scaffolds. Eur Spine J. 2007;16(11):1892–8.

130. Elsheikh A, Ross S, Alhasso D, Rama P. Numerical study of the effect of corneal layered structure on ocular biomechanics. Curr Eye Res. 2009 Jan;34(1):26–35.

131. Sneddon IN. The relation between load and penetration in the axisymmetric boussinesq problem for a punch of arbitrary profile. Int J Eng Sci. 1965;3(638):47–57.

132. Selvadurai APS. On Boussinesq's problem. Int J Eng Sci. 2001;39:317–22.

133. Scherer GW. Relaxation of a viscoelastic gel bar: I. Theory. J Sol-Gel Sci Technol. 1994;2(1–3):199–204.

134. Chan CM. Variations of Shear Wave Arrival Time in Unconfined Soil Specimens Measured with Bender Elements. Geotech Geol Eng. 2012;30(2):461–8.

135. Coop MR, Jovičić V, Simić M. Objective criteria for determining Gmax from bender element tests. Géotechnique. 1996;46(2):357–62.

136. Chan CM. Bender element test in soil specimens: Identifying the shear wave arrival time. Electron J Geotech Eng. 2010;15 M:1263–76.

137. Viggiani G, Atkinson JH. Interpretation of bender element tests. Int J Rock Mech

Min Sci Geomech Abstr. 1995;8(32):373A.

138. Lee J-S, Santamarina JC. Bender Elements: Performance and Signal Interpretation. J Geotech Geoenvironmental Eng. 2005;131(9):1063–70.

139. Youn JU, Choo YW, Kim DS. of Dry and Saturated Sands By Bender Element, Resonant Column, and Torsional Shear Tests. Can Geotech J. 2008;45(10):1426–38.

140. Hurtado J, Newson T. Measuring the small-strain elastic modulus of gap-graded soils using an effective-medium model and the resonant column apparatus. 68th Canadian Geotechnical Conference. Quebec City, Quebec.; 2015.

141. Drnevich VP, Werden S, Ashlock JC, Hall JR. Applications of the new approach to resonant column testing. Geotech Test J. 2015;38(1):23–39.

142. Kumar J, Clayton CRI. Effect of sample torsional stiffness on resonant column test results. 2007;230:221–30.

143. Oztoprak S, Bolton MD. Stiffness of sands through a laboratory test database. Géotechnique. 2012;(1):1–17.

144. Mcdonald JH. Handbook of Biological Statistics. 2008;

145. Narita T, Mayumi K, Ducouret G, Braud P. Viscoelastic properties of poly(vinyl alcohol) hydrogels having permanent and transient cross-links studied by microrheology, classical rheometry, and dynamic light scattering. Macromolecules. 2013;46(10):4174–83.

146. Lee OS, Kim M soo, Kim K, Hwang SW. Dynamic deformation behavior of rubber under high strain rate compressive loading. Int J Mod Phys B. 2003;17:1415–20.

147. Bergström JS, Boyce MC. Constitutive modeling of the large strain time-dependent behavior of elastomers. J Mech Phys Solids. 1998;46(5):931–54.

148. Shergold OA, Fleck NA, Radford D. The uniaxial stress versus strain response of

pig skin and silicone rubber at low and high strain rates. Int J Impact Eng. 2006;32(9):1384–402.

149. Larson K. Can You Estimate Modulus From Durometer Hardness for Silicones? Dow Corning Corporation;

150. Fu YB, Ogden RW. Nonlinear elasticity : theory and applications. Cambridge University Press; 2001. 525 p.

151. Li JK, Wang N, Wu XS. Poly(vinyl alcohol) nanoparticles prepared by freezing-thawing process for protein/peptide drug delivery. J Control Release. 1998;56(1–3):117–26.

152. Hickey AS, Peppas NA. Mesh size and diffusive characteristics of semicrystalline poly(vinyl alcohol) membranes prepared by freezing/thawing techniques. J Memb Sci. 1995;107(3):229–37.

153. Wang QM, Mohan AC, Oyen ML, Zhao XH. Separating viscoelasticity and poroelasticity of gels with different length and time scales. Acta Mech Sin Xuebao. 2014;30(1):20–7.

154. Schapery R a., Park SW. Methods of interconversion between linear viscoelastic material functions. Part II—an approximate analytical method. Int J Solids Struct. 1999;36(11):1677–99.

155. Lai CG, Pallara O, Presti DLCF Lo, Turco E, Lo Presti DCF. Low-strain stiffness and material damping ratio coupling in soils. Proc Adv Lab Stress Test Geomaterials. 2001;(January 2016):265–74.

156. Foti S, Lai CG, Rix GJ, Strobbia C. Surface wave methods for near-surface site characterization. CRS Press; 2014.

157. Roland CM. Dynamic mechanical behavior of filled rubber at small strains. J Rheol (N Y N Y). 1990;34:25–34.

158. Fortais A. private communication; 2015.

159. Schubert G, Harrison P. Large-strain behaviour of Magneto-Rheological Elastomers tested under uniaxial compression and tension, and pure shear deformations. Polym Test. Elsevier Ltd; 2015;42:122–34.

160. Kazimierska-Drobny K, El Fray M, Kaczmarek M. Determination of mechanical and hydraulic properties of PVA hydrogels. Mater Sci Eng C Mater Biol Appl. Elsevier B.V.; 2015 Mar;48:48–54.

161. Millon LE, Oates CJ, Wan W. Compression properties of polyvinyl alcohol-bacterial cellulose nanocomposite. J Biomed Mater Res - Part B Appl Biomater. 2009;90 B(2):922–9.

162. Storm C, Pastore JJ, MacKintosh F, Lubensky T, Jamney PA. Nonlinear elasticity in biological gels. Nature. 2005;435(May):191–4.

Appendix A: Mass Loss and Shrinkage of PVA-C, During Testing

A.1 Mass Loss of PVA-C

The changes in the mass of the PVA-C samples was observed for the large cylinder tests to assess potential changes during the resonant column testing. It was observed that the mass of the samples was not constant and decreases after short periods of time.

Changes in the mass of the samples was measured at 30-minute intervals for 210 minutes. The results for changes in the mass based on the PVA concentration and number of freeze/thaw cycles of the samples are provided as follows.

A.1.1 Effect of Number of Freeze/thaw Cycle

Figures A.1 to A.3 show the changes in the mass over time for different samples with 2 and 6 FTCs.

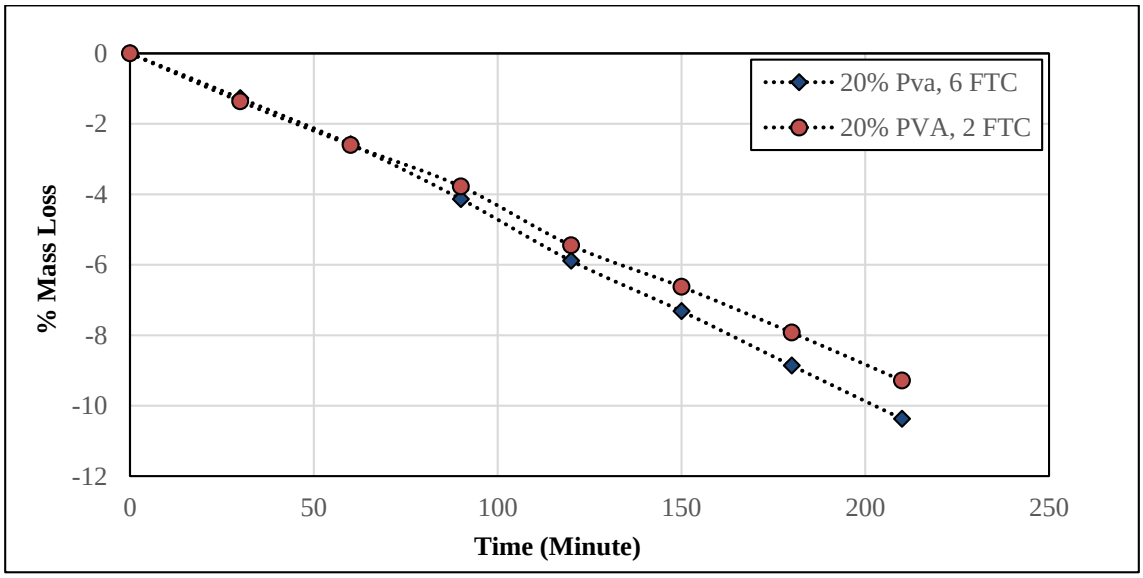

Figure A.1. Percent mass loss for 20 % PVA samples with different number of freeze/thaw cycles.

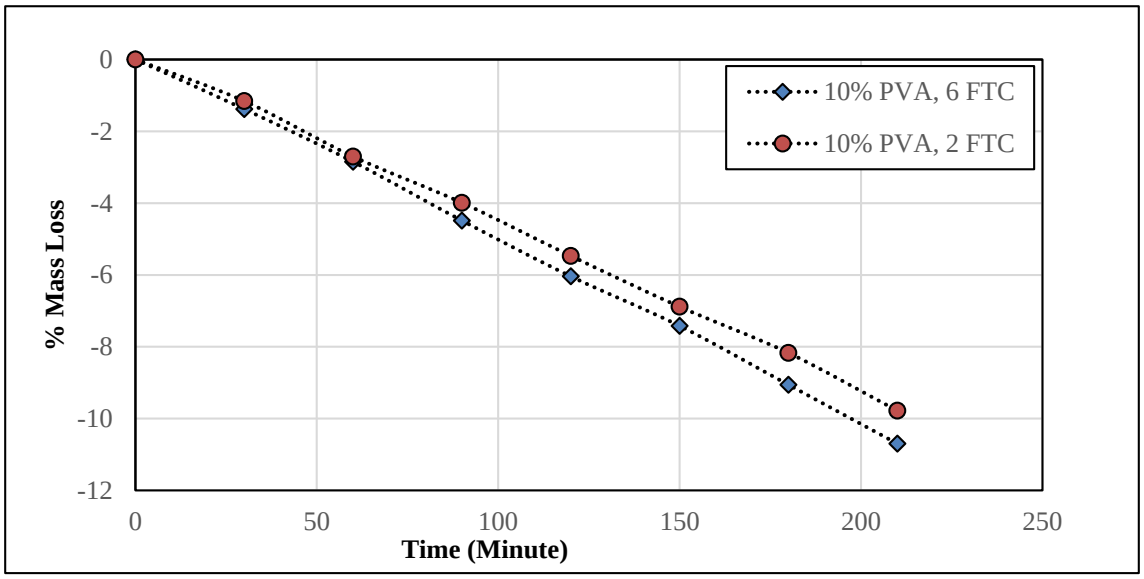

Figure A.2. Percent mass loss for 10 % PVA samples with different number of freeze/thaw cycles.

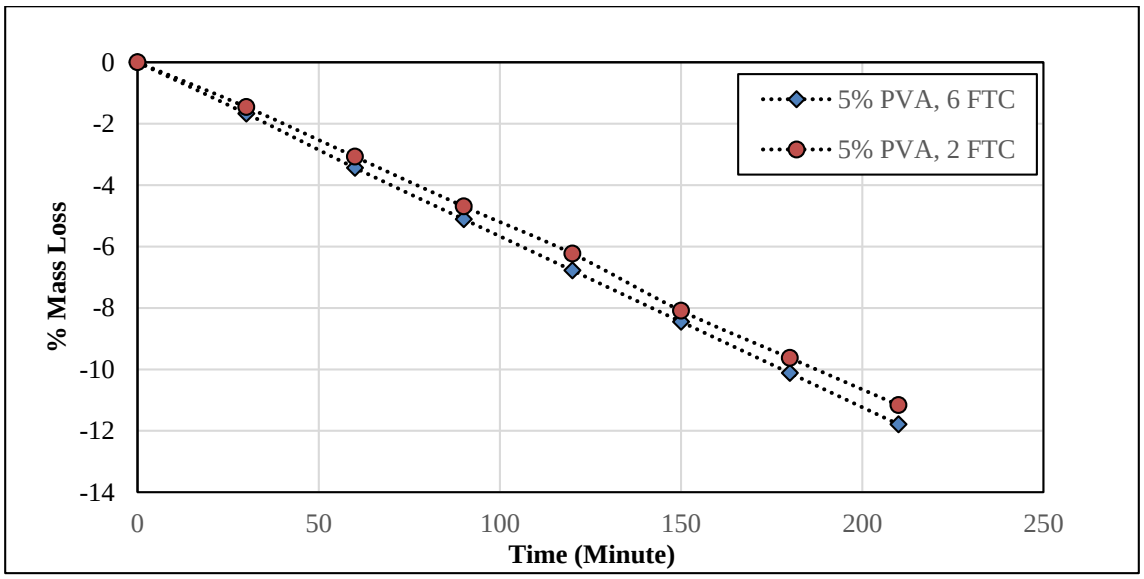

Figure A.3. Percent mass loss for 5 % PVA samples with different number of freeze/thaw cycles.

As shown in the graphs, for all of the samples, the percentage of changes in the mass are equal for the first hour of the measurement. After that, an increase in the mass loss over time is observed for 5%, 10%, and 20% PVA samples when the number of freeze/thaw cycles increases. The overall loss percent moisture also increases with reducing PVA

concentration. Assuming that the rates of evaporations from the samples were constant, then the water loss is most likely due to the available volumes of unchained water molecules in the specimens and permeability of the different formulations. Since increasing number of freeze/thaw cycles and PVA concentration are assumed to provide denser polymer networks, this is consistent with the results.

A.1.2 Effect of PVA Concentration

The changes in the mass of samples with different PVA concentration are shown in Figures A.4 and A.5.

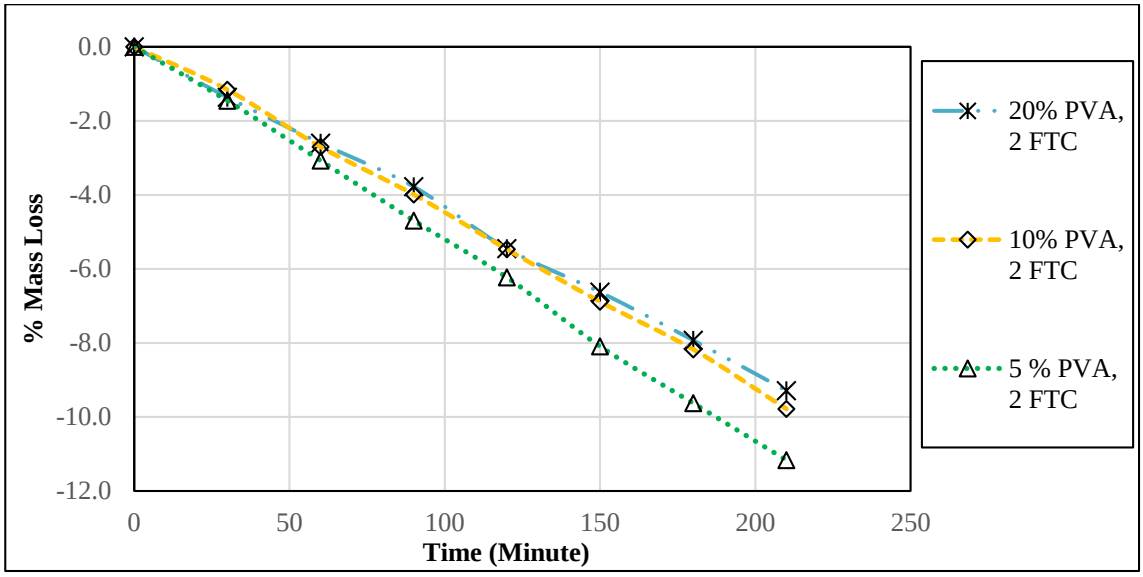

Figure A.4. Percent mass loss in different samples after 2 FTCs.

As shown in Figure A.4 for samples with different PVA concentrations after 2 FTC, the sample with 5% PVA has the most changes in its mass over the time of the test and the final mass of the sample after 210 minutes is approximately 12% lower than the initial mass. There is not a significant difference in the percent mass loss of the other samples over time and all of them lose about 10% of their mass at the end of the test.

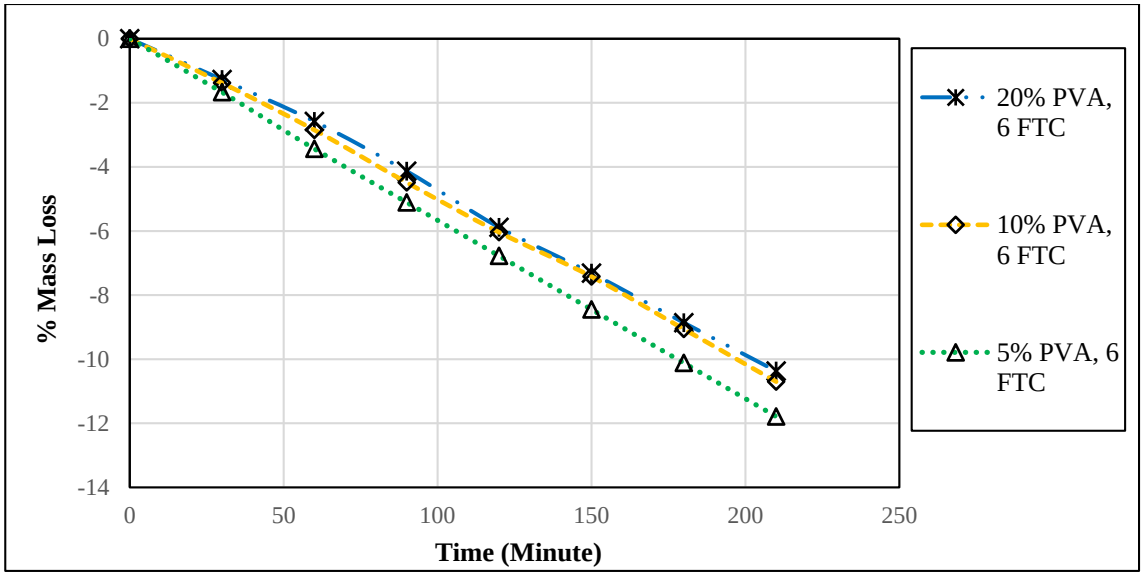

Figure A.5. Percent mass loss in different samples after 6 FTCs.

Figure A.5 shows the mass loss of samples after 6 FTCs and the material behaves in a similar manner to samples with 2 FTC (Figure A.4). During the tests, the samples with 10%, 15%, and 20% PVA lose about 10% of their mass at the end of the test. This behavior may be explained by microstructure of the PVA-C. 5% PVA sample has more water and therefore, more unchained water molecules in comparison to the stiffer samples. Thus, these unchained molecules can flow from the network more easily and cause higher changes in the mass.

A.2 Shrinkage of PVA-C

While conducting mechanical tests on the PVA-C samples, shrinkage of the PVA-C was noticed if the samples were kept out of water for more than one hour. Dimensional assessments for the shrinkage of the PVA-C are important because size of the samples is a crucial factor in some of the tests such as resonant column test.

The measurement of shrinkage of the PVA-C was investigated using the mini-puck samples with different PVA concentrations after 2 and 6 FTCs. Therefore, the relationship between PVA concentration and number of freeze/thaw cycles on shrinkage of the samples was investigated. The dimensions (diameter and height) of each mini-puck PVA-C samples were measured by means of a Vernier caliper, and considered to be the original dimensions.

This measurement was conducted right after removing the samples from the deionized water and the samples were not dehydrated. The results are reported as an average of six measurements. These measurements were repeated after two hours and the shrinkage was calculated by comparing the average diameter and length of each sample at the two different times.

The results of the measurements are compared between the samples with different PVA concentrations and number of freeze/thaw cycles.

A.3.1 Effect of Number of Freeze/thaw Cycles

To investigate the effect of freeze/thaw cycles on the shrinkage of the samples, samples with 2 and 6 FTCs were compared together. Results of these comparisons are provided in figures A.6 to A.9. Error bars show the significant differences between the values.

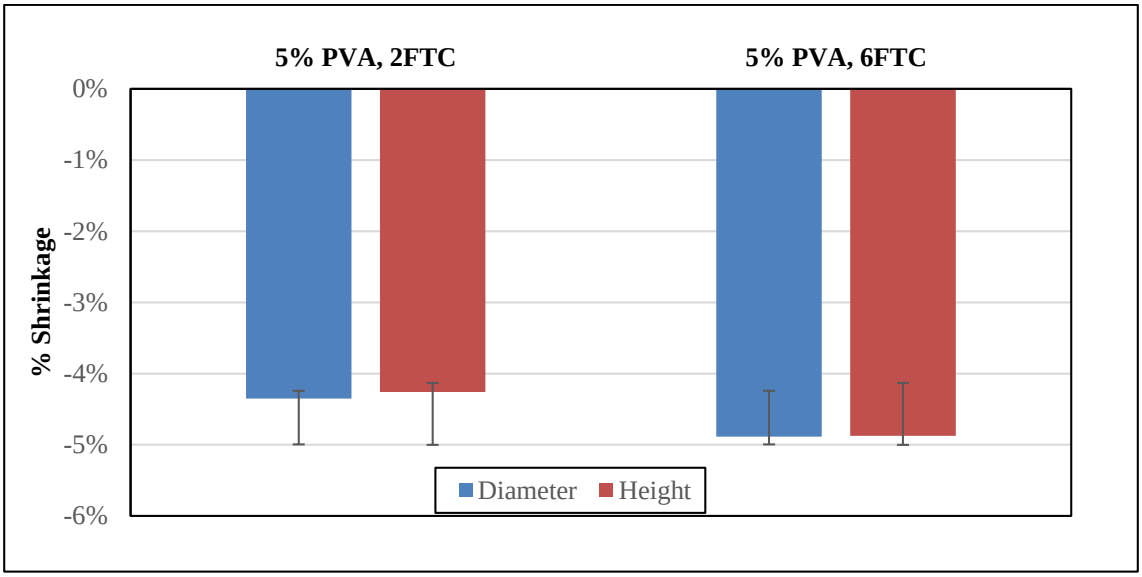

Figure A.6. Effect of number of freeze/thaw cycle on the shrinkage of 5% PVA mini-pucks

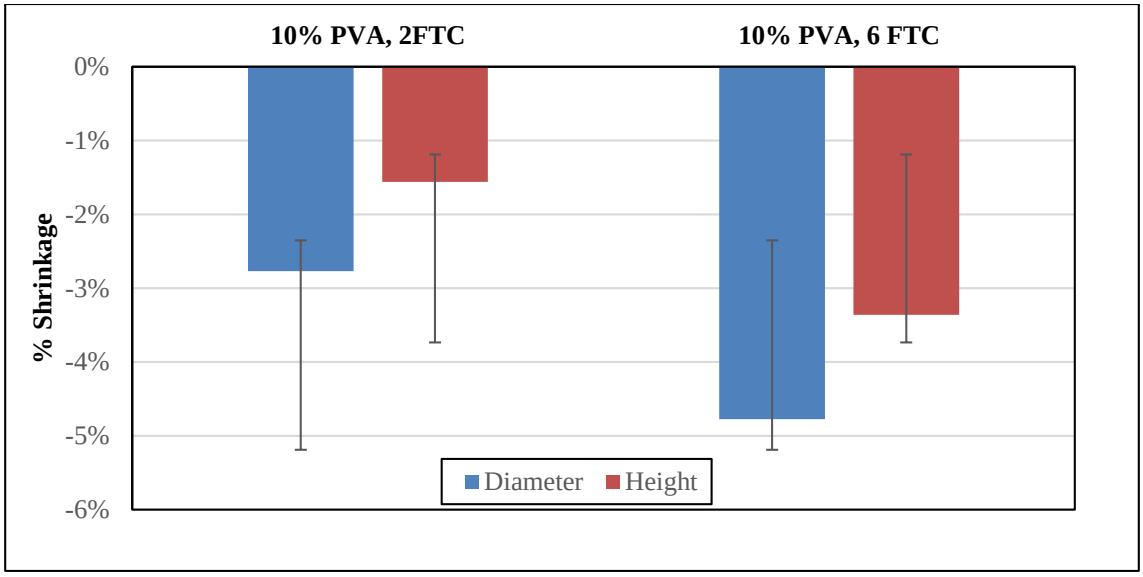

Figure A.7. Effect of number of freeze/thaw cycle on the shrinkage of 10% PVA mini-pucks.

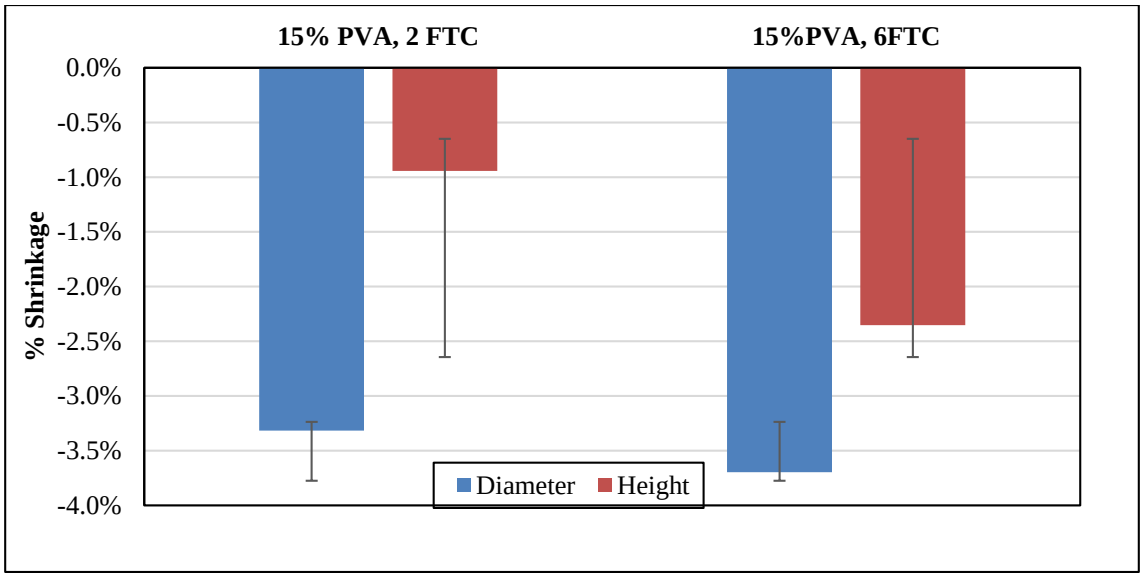

Figure A.8. Effect of number of freeze/thaw cycle on the shrinkage of 15% PVA mini-pucks.

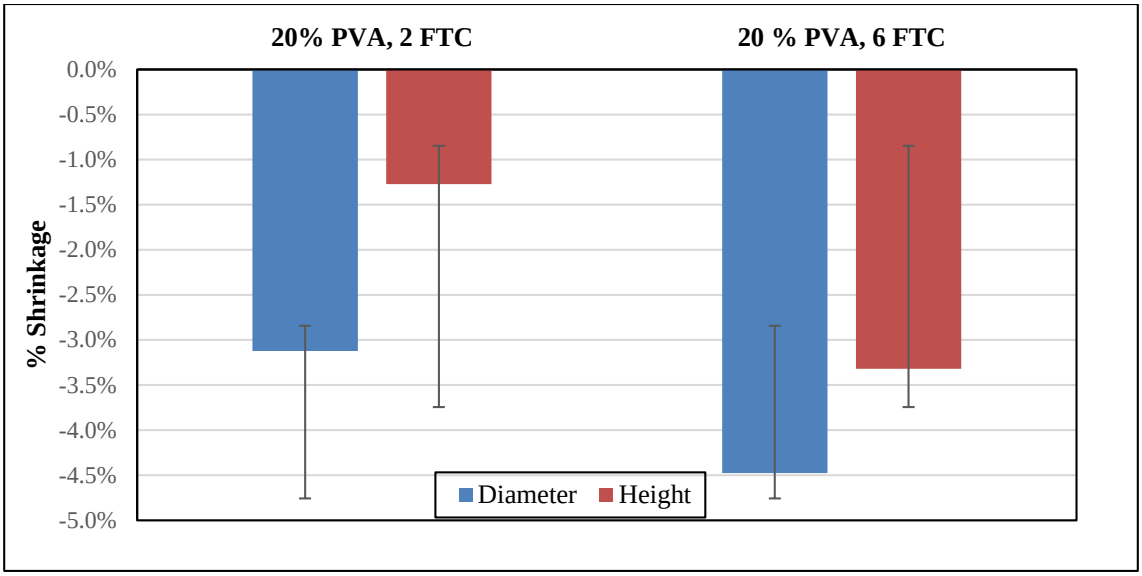

Figure A.9. Effect of number of freeze/thaw cycle on the shrinkage of 20% PVA mini-pucks.

As shown in Figure A.7, there is not a significant difference between the shrinkage of the height and diameter of the 5% PVA samples. However, Figures A.8 and A.9 show that for other samples the percent shrinkage of the dimeter of the samples is higher than the height and therefore, the diameter of the samples has shrunk more than their height. As shown in all of the figures, for all of the samples both height and diameter shrink more when the number of freeze/thaw cycle goes from 2 to 6 FTC. This is due to the changes in the microstructure of the samples. As they go through more freeze/thaw cycle, the crystallites pack tighter and therefore, the size of the samples decreases.

A.3.2 Effect of PVA Concentration

Effect of PVA concentration on percent shrinkage in height and diameter of different samples is shown in Figures A.10 and A.11. Again, error bars show the significant difference.

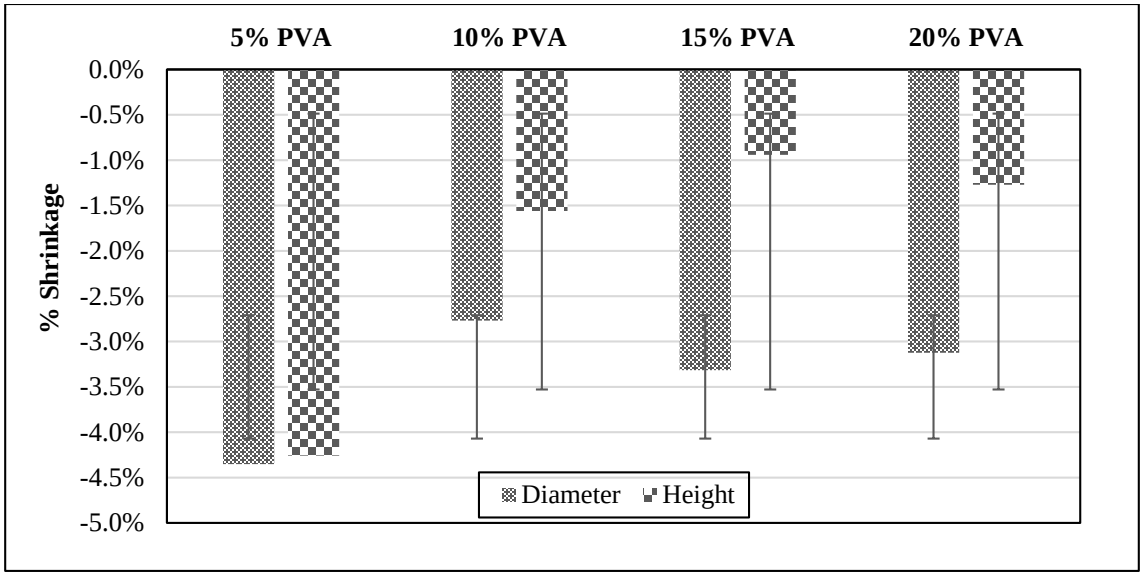

Figure A.10. Effect of PVA concentrations on samples after 2 FTCs.

As shown in Figure A.10, the shrinkage of the height of the samples decreases as the PVA concentration increases from 5% to 15%. The shrinkage of the height of the 20% PVA is higher than that of 15% PVA, but still lower than the 5% and 10% PVA samples. The diameter of the samples shrinks when the PVA concentration increases from 5% to 10%. The shrinkage of the diameter in the 15% PVA sample is higher than 20% PVA.

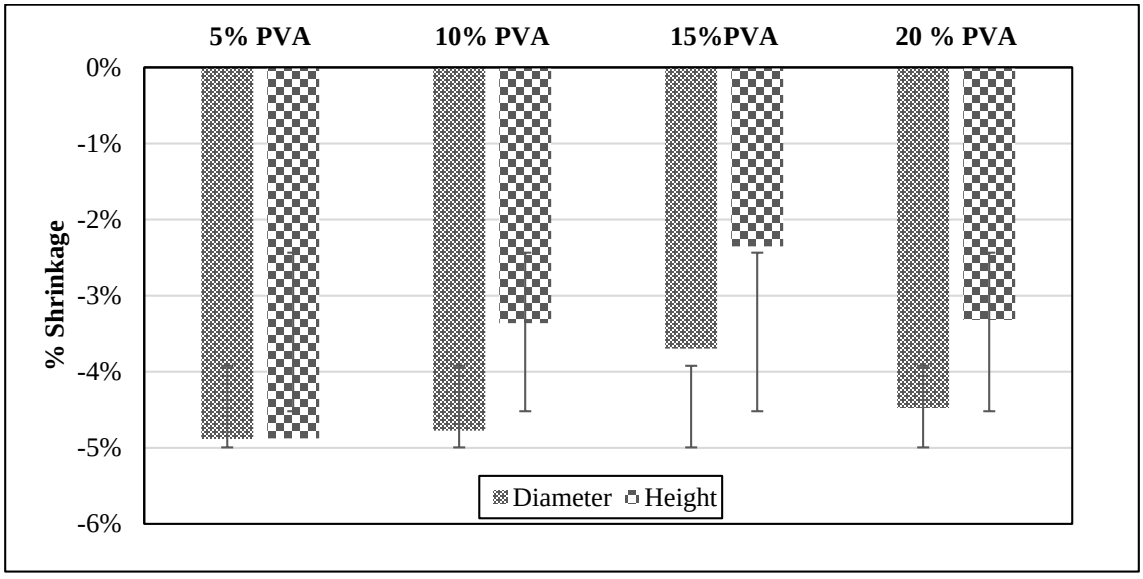

Figure A.11. Effect of PVA concentrations on samples after 6 FTCs.

Figure A.11 shows the effect of PVA concentration on samples after 6 FTCs. The shrinkage in the diameter of the 5%, 10% PVA, and 20% PVA samples are very similar but higher

than that of 15% PVA sample. It is also shown that the height of the sample shrinks more if the sample has 5% or 10% PVA concentration.

Data provided in these figures show that the shrinkage of the PVA-C is affected by both PVA concentration and number of freeze/thaw cycles. These data are good references to choose the proper PVA-C sample for different mechanical tests and in combination with the previous tests allowed correct time of test to be selected. For resonant column test, as explained in Section 3.3.4, the height to diameter ratio of the samples should be 2 to 1, and the device was setup for samples with 50 mm diameter. It was not possible to get reasonable results for 10% PVA, 6 FTC samples because the sample could not meet the requirements for the aspect ratio. As shown in Figure A.11, 10% PVA after 6 FTCs becomes about 3.5 % shorter in height and about 5% in diameter. Therefore, the final height and diameter of the sample does not meet the requirements for the aspect ratio and the device setup for diameter.

Appendix B: Unconfined Compression: Additional Data

B.1 Force-displacement curves

During unconfined compression testing, as explained in Section 3.3.1, the force and displacement data were recorded with the GETDATA software. Figures B.1 and B.2 show force applied to the sample for different displacements during both loading and unloading cycles. Figure B.1 compares force-displacement graphs for samples with different PVA concentrations, and Figure B.2 compares the graphs of samples with different numbers of freeze/thaw cycles.

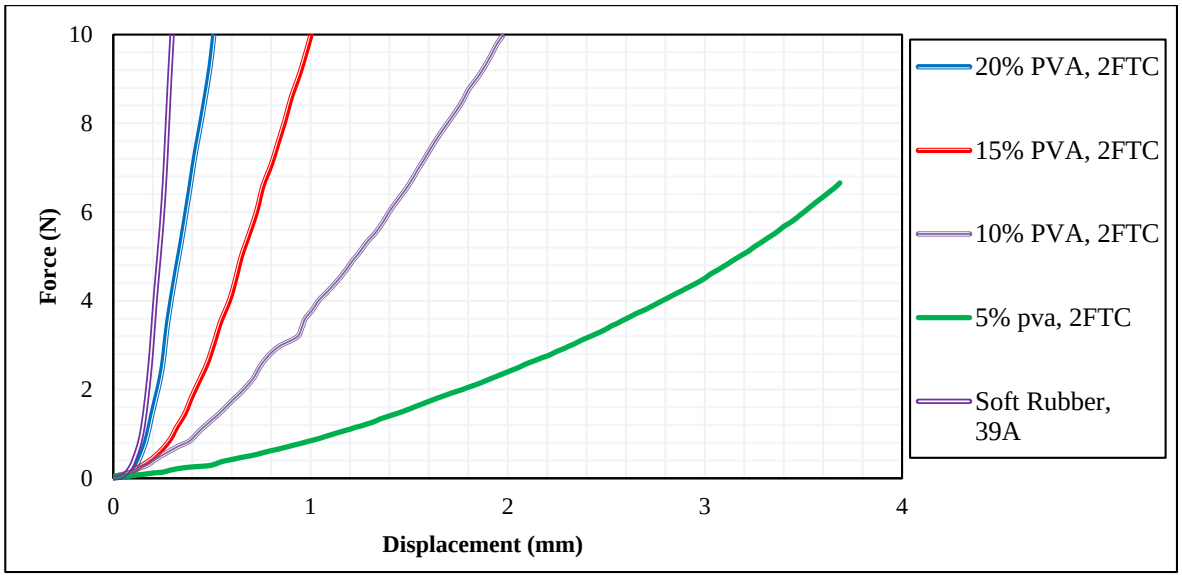

Figure B.1. Loading force versus displacement for samples with different PVA concentrations, along with a rubber sample.

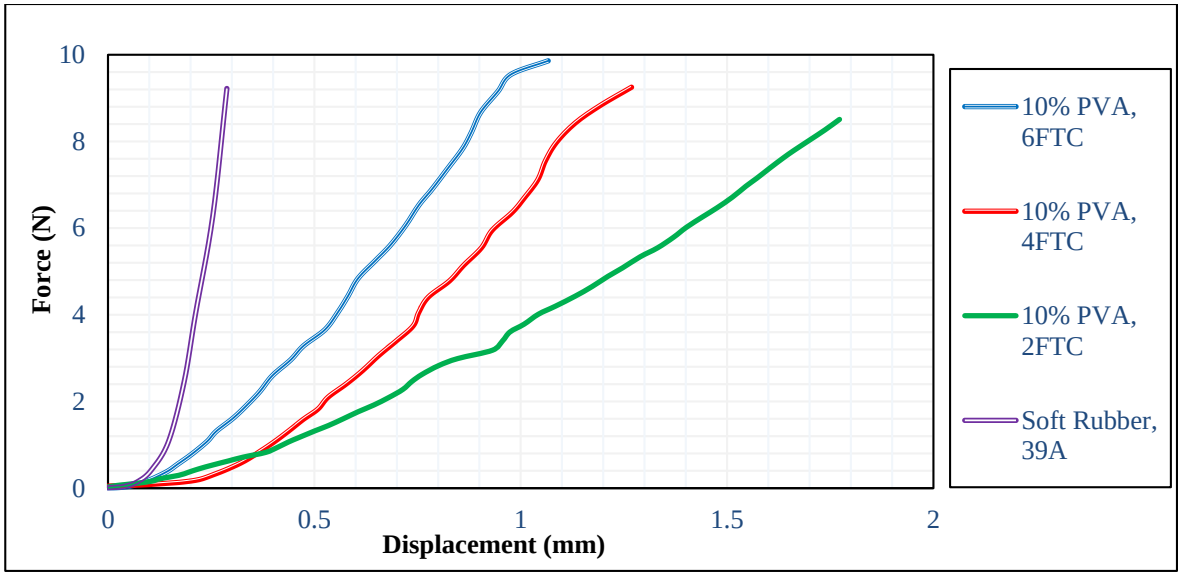

Figure B.2. Loading force versus displacement for samples with FTCs, along with a rubber sample.

As shown in the previous figures, force has a direct relationship with axial displacement. The axial force on the sample increases as samples is more deformed. It is seen in Figure B.1 that the curves of samples with higher PVA concentrations have higher slopes. The same trend is observed in Figure B.2, in which force-displacement curves of samples with higher number of FTCs have higher slopes.

B.2 Curve Fitting Parameters

B.2.1 Effect of PVA Concentration

As explained in Section 4.2.1.1, the stress-strain curves were fitted to equation 3.6. Curve fitting parameters and the correlation coefficients for all of the samples were also provided in Table 4.1. Changes in the two curve fitting parameters between different samples with 2 FTCs was previously plotted in that section. The additional relationships between the curve fitting parameters, α and β, and PVA concentration for samples with 4 and 6 FTCs are shown in Figures B.3 and B.4, respectively.

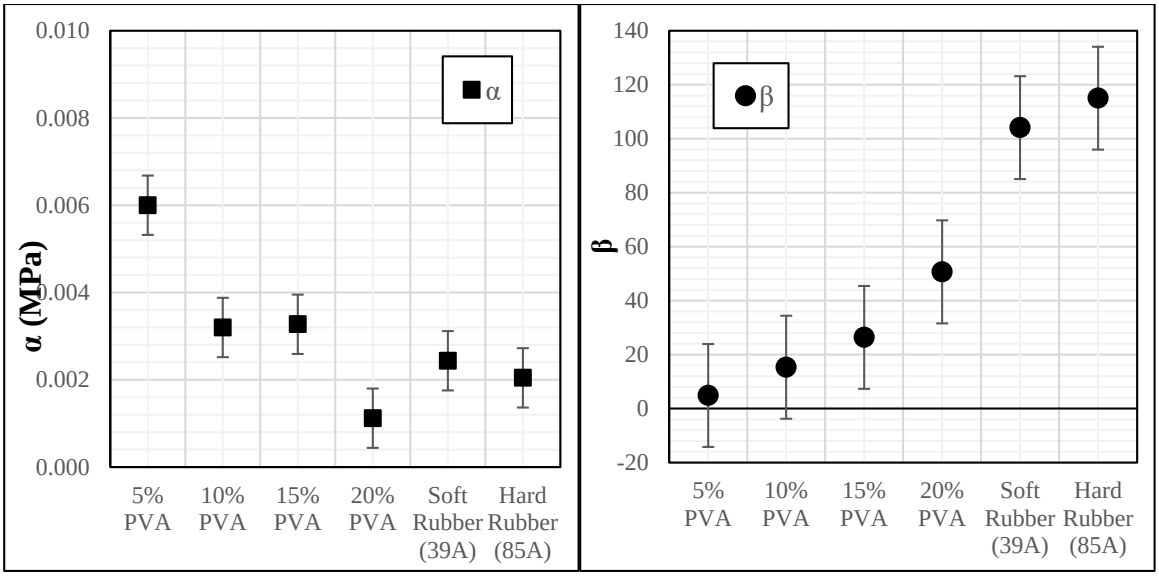

Figure B.3. Stress-strain curve fitting parameters α (left) and β (right) for samples with different PVA concentrations after 4 FTCs.

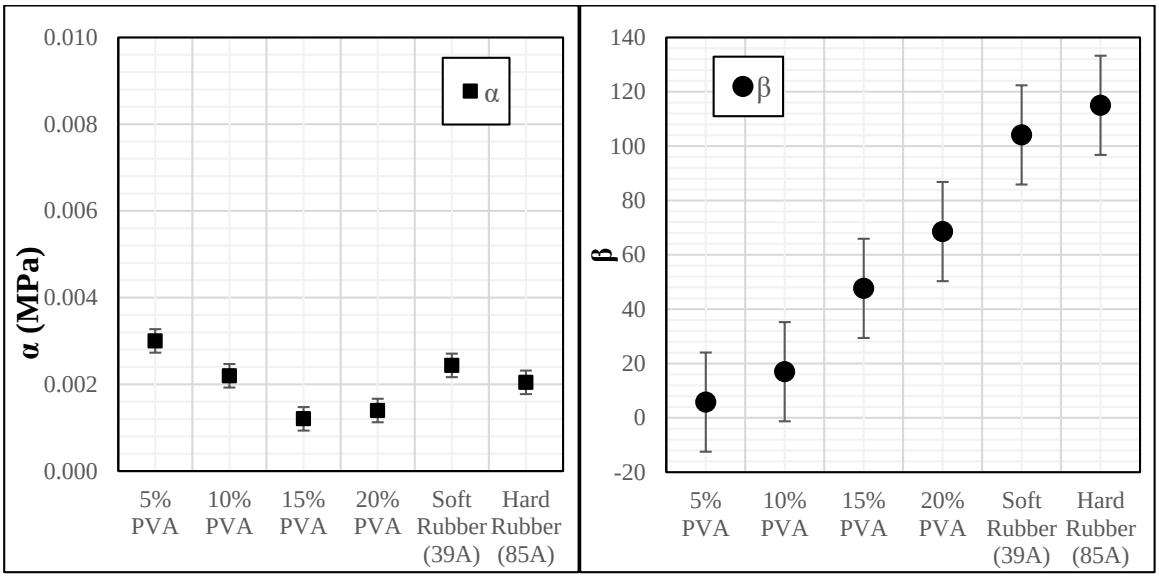

Figure B.4. Stress-strain curve fitting parameters α (left) and β (right) for samples with different PVA concentrations after 6 FTCs.

B.2.2 Effect of Freeze/thaw Cycles

Figures B.5 and B.6 show the additional relationships between the curve fitting parameters and the number of freeze/thaw cycles for samples with 5% and 20% PVA concentration, respectively.

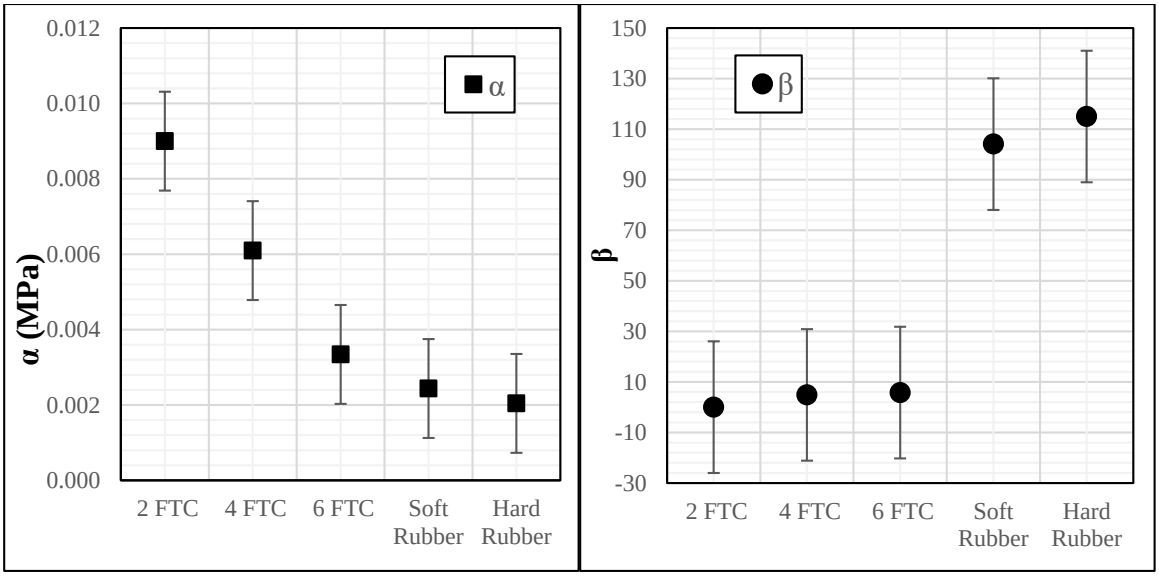

Figure B.5. Stress-strain curve fitting parameters α (left) and β (right) for 5% PVA samples with different numbers of freeze/thaw cycles.

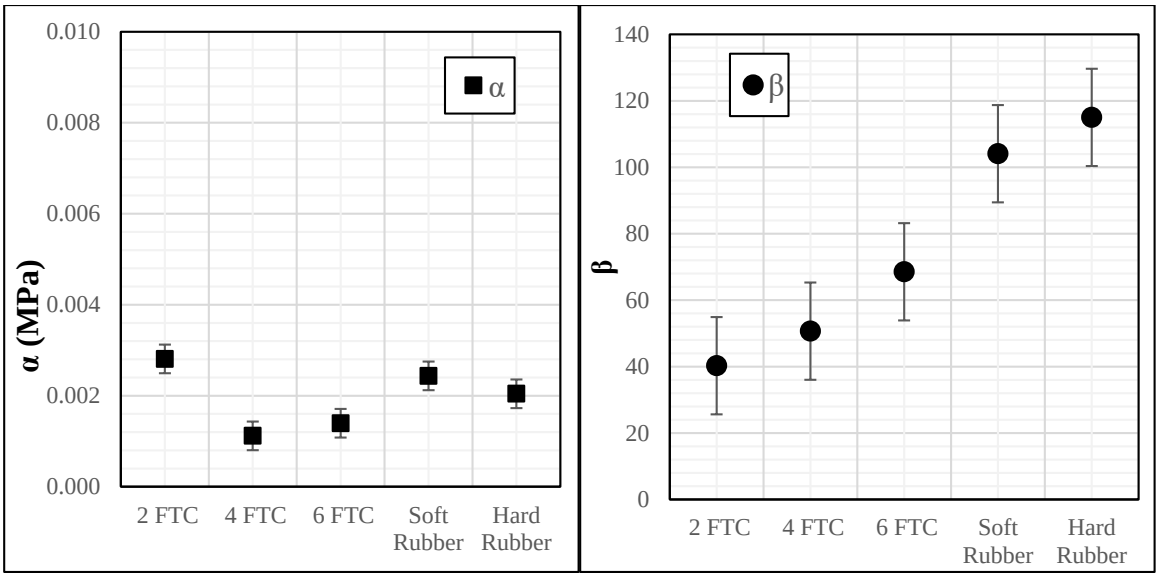

Figure B.6. Stress-strain curve fitting parameters α (left) and β (right) for 20% PVA samples with different numbers of freeze/thaw cycles.

The values of the curve fitting parameter α has an inverse relationship with the number of freeze/thaw cycles. However, the curve fitting parameter β increases for higher numbers of freeze/thaw cycle (for further discussion see Section 4.2.4.2).

B.3 Young's Moduli

Young's moduli of the mini-puck samples at 3% strain were calculated from unconfined compression test data using equation 3.7. These values are shown in Table B.1.

Table B.1. Young's moduli of all of the mini-puck samples at 3% strain obtained from unconfined compression test

	5% PVA	10% PVA	15% PVA	20% PVA
2 FTCs	0.01 ± 0.001	0.028 ± 0.003	0.077 ± 0.030	0.202 ± 0.027
4 FTCs	0.01 ± 0.002	0.044 ± 0.013	0.169 ± 0.025	0.294 ± 0.019
6 FTCs	0.017 ± 0.002	0.053 ± 0.005	0.235 ± 0.094	0.236 ± 0.037

As shown in the table, Young's modulus increases in samples with higher PVA concentrations and more number of freeze/thaw cycles. See Section 4.2.2 for detailed explanation.

Appendix C: Rigid Indentation: Additional Data

C.1 Force-displacement Curves

Force and displacement data from the rigid indentation test is recorded by GETDATA software. Figures C.1 and C.2 show force applied to the sample versus indentation depth during loading.

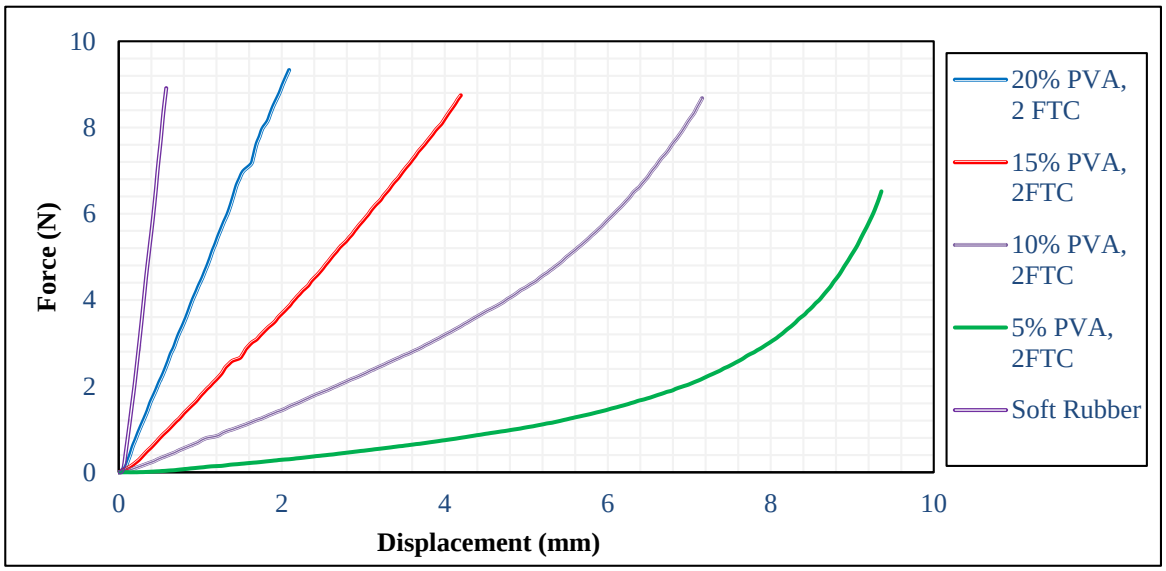

Figure C.1. Loading force versus displacement for samples with different PVA concentrations, along with a rubber sample.

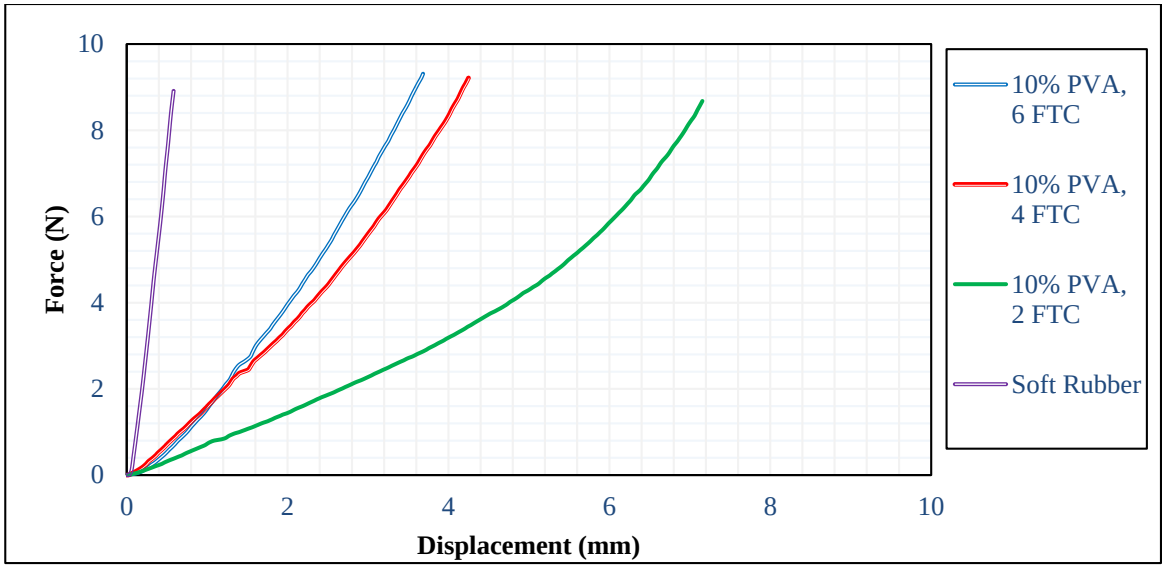

Figure C.2. Loading force versus displacement for samples with different freeze/thaw cycles, along with a rubber sample.

As shown in both figures, force-displacement curves show higher slopes in stiffer samples. Figure C.1, shows that in different samples after 2 FTCs, the force-displacement curves become steeper as the PVA concentration increase. It can be seen in Figure C.2 that the slope of the force-displacement curves increases in samples with higher numbers of freeze/thaw cycles.

C.3 Young's Moduli

C.3.1 Young's Moduli of Thick Samples

Large cylindrical samples were indented and their Young's moduli were calculated using equation 3.10. The values of Young's moduli of these samples at 3% strain were compared in Figure 4.15. Table C.1 provides those values regarding to this table.

Table C.1. Young's moduli for all of the thick samples at 3% strain, obtained from rigid indentation test.

	5% PVA	10% PVA	15% PVA	20% PVA
2 FTCs	0.003±0.002	0.011±0.001	0.035±0.001	0.069±0.001
4 FTCs				0.091±0.002
6 FTCs				0.122±0.003

See section 4.3.1.1 for more description of these values.

C.3.2 Young's Moduli of Thin Samples

Young's moduli of the thin samples (mini-pucks) were calculated using equation 3.14. Figures 4.17 and 4.18 compares the Young's moduli of all of the mini-puck samples at two different strains of 3% and 10%. Tables C.2 and C.3 provide the values of Yong's moduli shown in Figures 4.17 and 4.18, respectively.

Table C.2. Young's moduli of all of the mini-pucks at 3% strained, obtained from rigid indentation test.

	5% PVA	10% PVA	15% PVA	20% PVA	Soft Rubber
2 FTCs	0.007±0.001	0.031±0.002	0.065±0.006	0.206±0.019	
4 FTCs	0.010±0.004	0.044±0.001	0.153±0.005	0.295±0.006	
6 FTCs	0.011±0.003	0.066±0.005	0.189±0.006	0.262±0.021	
Soft Rubber					0.681±0.001

Table C.3. Young's moduli of all of the mini-pucks at 10% strain, obtained from rigid indentation test.

	5% PVA	10% PVA	15% PVA	20% PVA
2 FTCs	0.008±0.001	0.036±0.001	0.088±0.002	0.222±0.012
4 FTCs	0.021±0.002	0.080±0.003	0.179±0.002	0.344±0.002
6 FTCs	0.024±0.000	0.083±0.002	0.245±0.003	0.345±0.007

See section 4.3.2.1 for detailed description.

Appendix D: Load Relaxation: Additional Data

Load relaxation curves for each samples were fitted to Equation 3.15, for the first thirty seconds of relaxation. Figures D.1 to D.5 show the force over the normalized time, t^*, for samples with different PVA concentrations with 6 FTCs, along with the soft rubber (39A) sample.

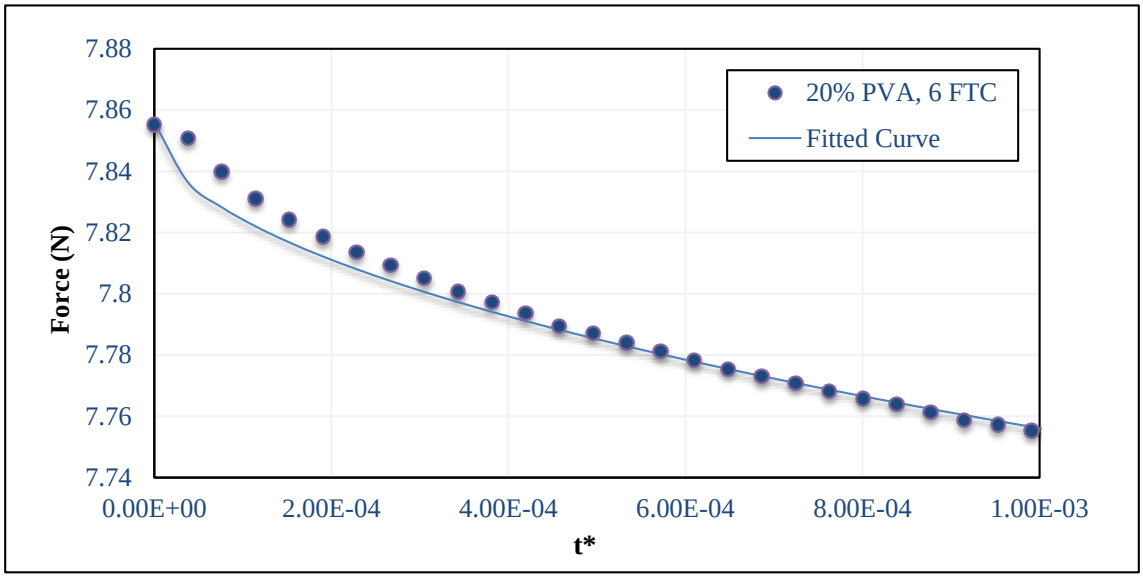

Figure D.1. Force versus the normalized time for 20% PVA, 6FTC

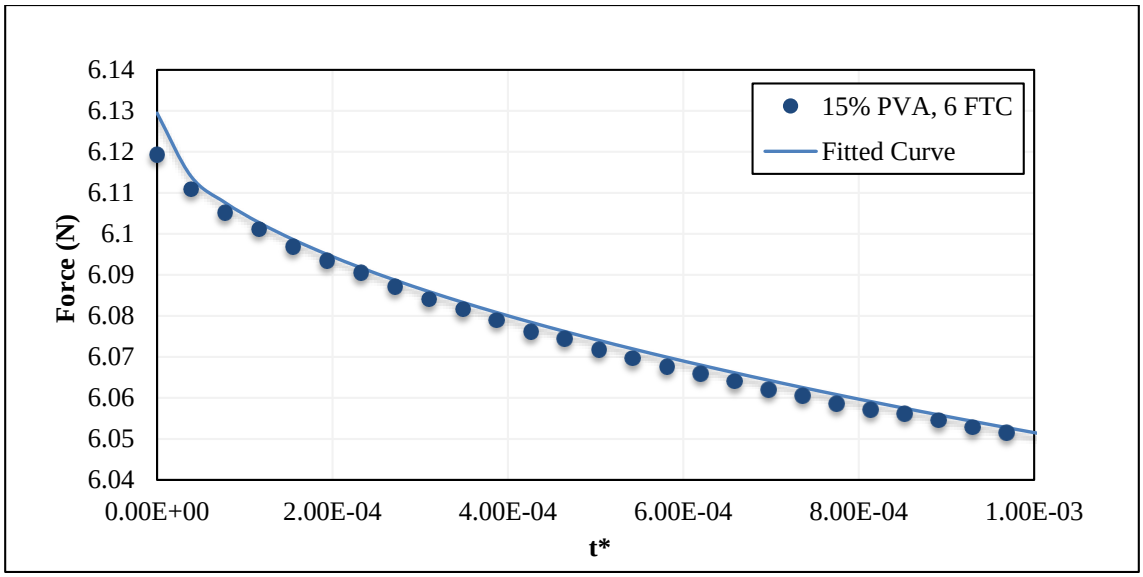

Figure D.2. Force versus the normalized time for 15% PVA, 6FTC

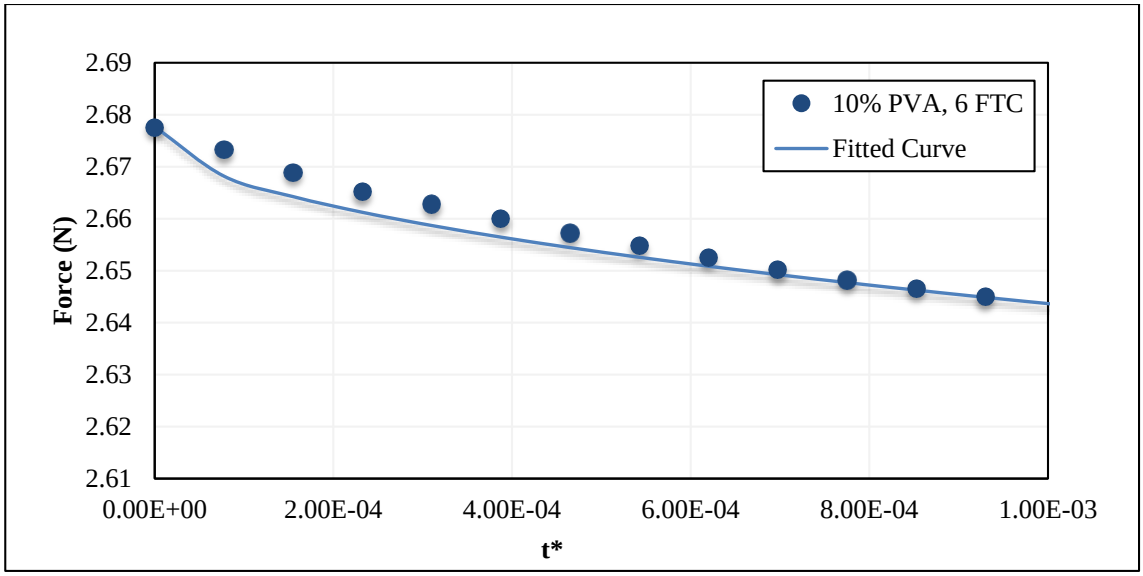

Figure D.3. Force versus the normalized time for 10% PVA, 6FTC.

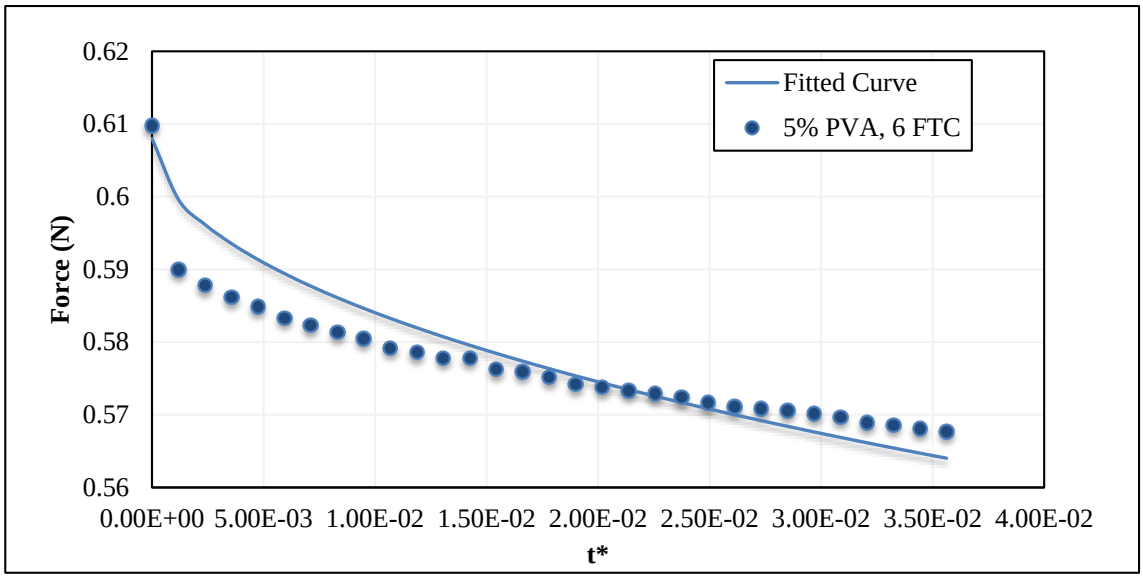

Figure D.4. Force versus the normalized time for 5% PVA, 6FTC.

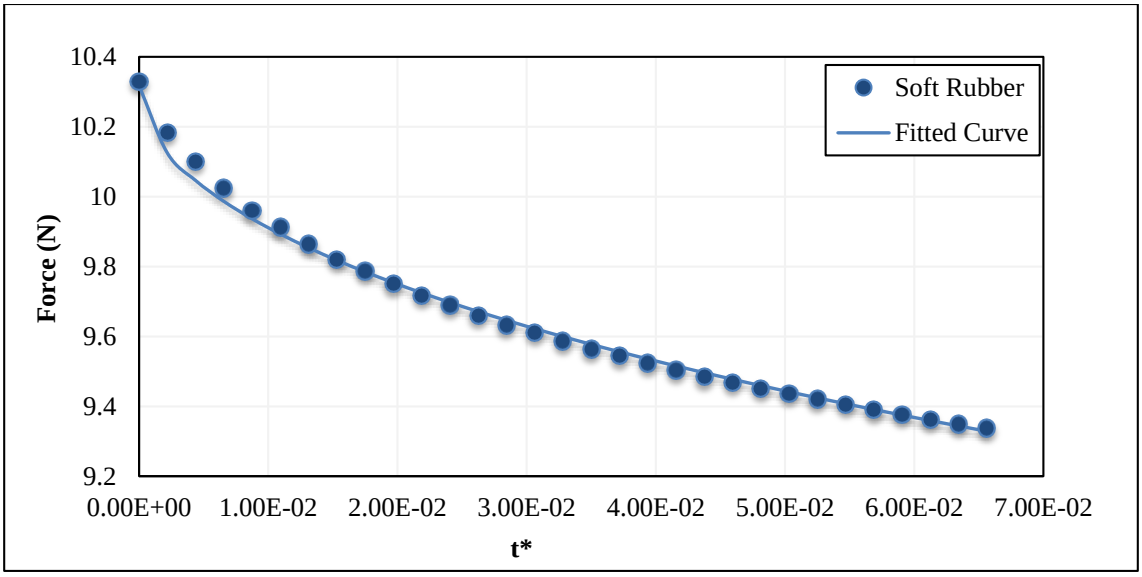

Figure D.5. Force versus the normalized time for the soft rubber (39A) sample.

For further discussion on these results see Section 3.4.2.3.

Appendix E: Damping Test: Additional Data

A single damping ratio test was performed on a 20% PVA sample with 6 FTC. The results of the damping ratio are shown in Figure 4.35 and were used to calculate loss and storage moduli of the samples based on the equation provided in Section 4.5.3. Figures E.1 and E.2 show these results for loss modulus and storage modulus, respectively.

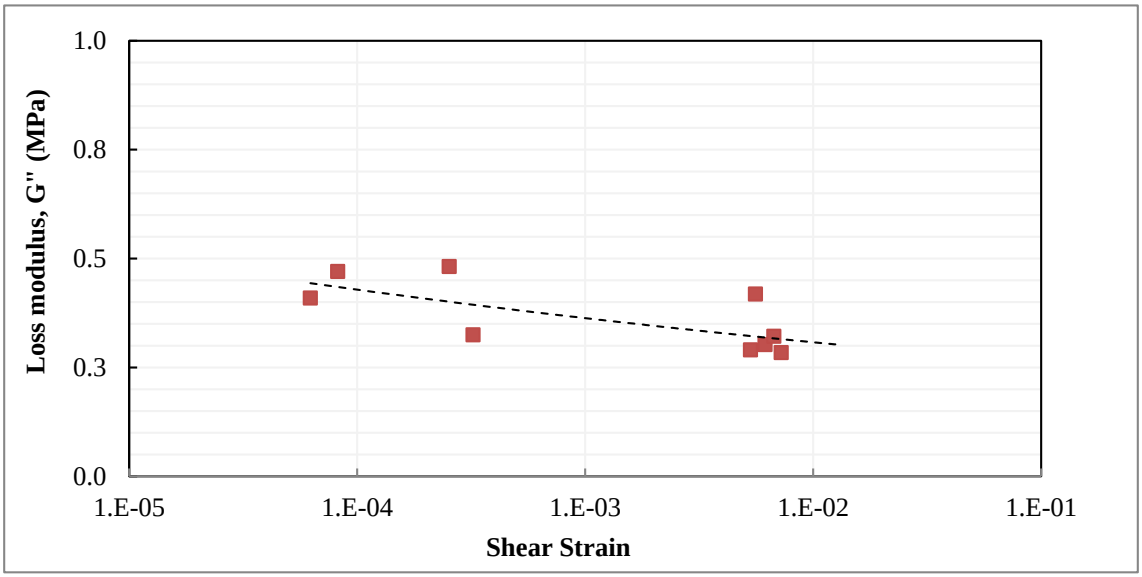

Figure E.1. Loss modulus over shear strain for 20% PVA, 6 FTC sample.

As shown in Figure E.1, by increasing shear strain from 0.0001 to 0.01, loss modulus decreases from approximately 0.46 to 0.34 MPa.

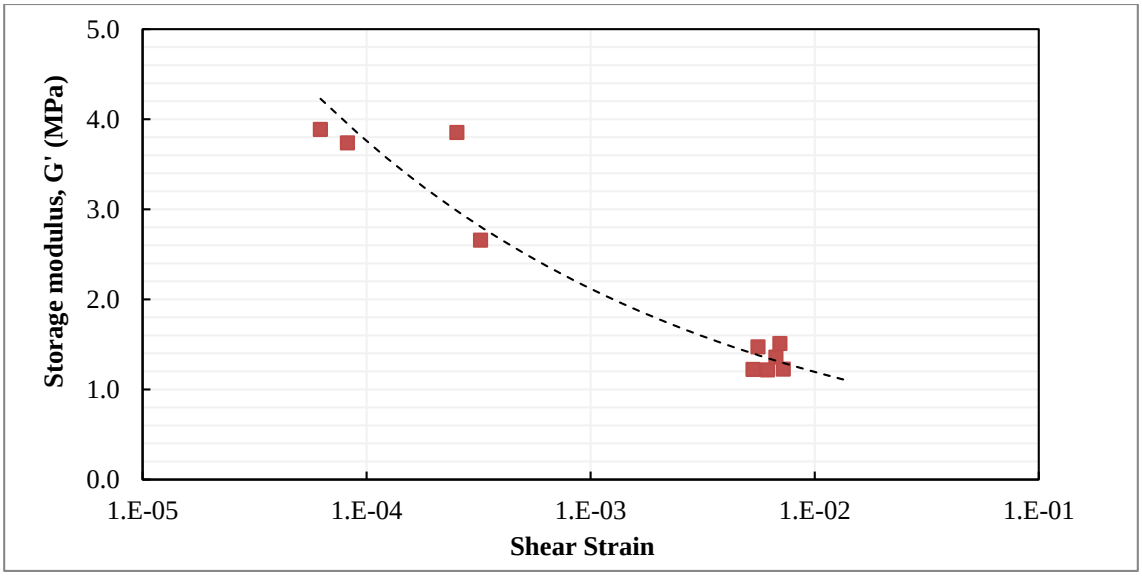

Figure E.2. Storage modulus over shear strain for 20% PVA, 6 FTC sample.

Figure E.2 shows that the storage modulus of the sample decreases from about 4.2 to 1 MPa while the shear strain increases from 0.0001 to 0.01. See Section 4.5.3 for further discussion.

Curriculum Vitae

Name:	Mojdeh Zakeri
Post-secondary Education and Degrees:	Amirkabir University of Technology, Tehran, Iran Bachelor of Science, Biomedical Engineering 2008-2012
Honours and Awards:	Western Graduate Research Scholarship 2014-2016
Related Work Experience	Teaching Assistant The University of Western Ontario 2014-2016